# Case Studies in Forcing Small Motor Neural Circuits

by

## Marcello Codianni

BS, University of New Mexico, 2014

Submitted to the Graduate Faculty of

the Dietrich School of Arts and Sciences in partial fulfillment

of the requirements for the degree of

## Doctor of Philosophy

University of Pittsburgh

2021

UNIVERSITY OF PITTSBURGH

DIETRICH SCHOOL OF ARTS AND SCIENCES

This dissertation was presented

by

Marcello Codianni

It was defended on

November 16, 2021

and approved by

Jon E. Rubin, Departmet of Mathematics

Bard Ermentrout, Department of Mathematics

David Swigon, Department of Mathematics

Robert S. Turner, Department of Neurobiology

**Case Studies in Forcing Small Motor Neural Circuits**

Marcello Codianni, PhD

University of Pittsburgh, 2021

The goal of this work is to explore a variety of forcing scenarios in small motor control neural circuits. Numerous motor circuits interact to produce coordinated movement, and forcing represents a convenient way to abstract the activity of other circuits so that the analysis remains tractable. First, we analyze a pacemaking circuit responsible for joint coordination. This circuit receives periodic bottom-up forcing from ground contact signalling. We then modulate the circuit's pacemaking properties through top-down input, and examine the range in which this circuits output remains entrained to the forcing, allowing the animal to keep its limbs coordinated during changing pace. Next, we turn our attention to a pathological case of motor tics, where an unknown forcing signal produces stereotyped outputs. We build a detailed neural model which expresses a great variety of observed behavior, and carefully analyze how different current channels in the model can account for these different behaviors. We then link it to another neuron model in a small, indirectly coupled circuit and and study the response to different forcing profiles, and explain the model responses to this forcing, offering mechanisms by which the motor tic may be explained. Finally, we observe that during sustained, but modulated, forcing, the detailed model exhibits chaotic behavior. We simplify the model to the key components in generating the chaotic firing, and perform mathematical analysis utilizing tools from dynamical systems to examine the route to chaos through examining its bifurcation structure and Lyapunov exponent approximations.

# List of Tables

# List of Figures

# Preface

On December 31, 1999 my parents told me and my brother they had a special, new millennium New Year's treat for us: An R-rated movie. They pulled out a collector's edition, foil cover, VHS cassette of The Matrix. Being 10, all of the philosophical and political nuance of the film went over my head, and all I thought was that it's the coolest thing I'd ever heard of, and we should totally make that a reality. 20 years later, it is still the coolest thing I've ever heard of, and we should totally make that a reality. Of course, it would make more sense if the machines used human brains to perform menial computations, a notion which has brought me here today. Hopefully not to enslave humanity as a collection of pocket calculators, but rather to help us integrate with our technology and realise our full potential, and, on a deeper level, understand who we are and why we do the things that we do.

Joking aside, I have thoroughly enjoyed my time at Pitt. It has been an incredible experience to be immersed in the culture made by these titans of the field. I especially thank my advisor, Dr. Jon Rubin, who has kept me on the right track despite my best efforts to derail myself, I could not have done this without you. I would also like to thank my committee: Dr. Bard Ermentrout, who taught me about half of everything I know, Dr. Robert Turner, who gave me my first taste of real neural data, and Dr. David Swigon, who helped me overcome my early milestones.

I would like to thank my family. My mother Kathleen, who never let me forget the value of an education and endlessly supported my desire to learn, my father Paul, who introduced me to the idea of scientific principles and told me I would never be a doctor sleeping until noon every day, and my brother Simon, who not only kept me alive, but connected to and interested in the world around me.

I would also like to thank my friends: Dan Ehrmann, who is endlessly reliable, Ben Letson, whose scornful cynicysm made excellent comedy, Michael McLaughlin, whose level-headed outlook keeps things in perspective, and Nathan Fulton, who is probably the smartest person I've ever spoken to. I want to especially thank Abby Pekoske, who is so on my wavelength that we are practically psychically linked, and Michael Lindsey, whose carefree

attitude is something to aspire to. Abby's "Can-do, and don't you dare tell me otherwise," and Michael's unnerving and unerring attention to detail make them some of the best mathematicians I know. I couldn't ask for better friends, and they have kept me going all these years.

Now then, on with the show.

# 1.0   Introduction

## 1.1   Background

Neural systems are found in nearly all animals, with very few notable exceptions, such as Porifera (sponges). The prevalence of neural systems in the animal kingdom can be succinctly explained by the fact that these neural circuits provide a robust mechanism for animals to make sense of and move through the word; humans are, of course, no exception, and thus, if we wish to understand our own senses, thoughts, and actions, we must first understand the behavior of neurons and neural circuits. Neurons communicate with one-another through spiking, all-or-none action potentials, or through graded potentials, and often arrange themselves into small-world networks; networks which concurrently minimize the number of connections made and the number of intermediate neurons on the path from any one cell to another. This small-world characteristic then allows us to examine the structure and behavior of smaller neural circuits in isolation, where the spontaneous activity of individual neurons informs the spontaneous activity of the circuit. Of course, these small circuits do not actually exist in isolation, and whether it be from different neural circuits or senses such as vision, hearing, or physical contact, some of the neurons in our circuit will inevitably receive some external input. We can then model this external input to our small, isolated circuits mathematically through forcing one or more neurons. Considerable work has been done on modeling these small circuits, and a thorough, detailed overview of different modeling approaches can be found in Mathematical Foundations of Neuroscience [48]. However, considerable work still remains, especially when it comes to specific responses to signaling. In this thesis, I will present work in two such problems: joint control in stick insect during certain walking patterns as a response to periodic forcing, and the response to a simple striatal circuit during forcing of an unknown type.

## 1.2 Modeling Approaches

When studying neural circuits, it is often useful to consider the dynamics of simplified models. One such class of these models are the so-called circle maps, in which, rather than details of voltage or currents, an oscillating neuron's phase is modeled through $\frac{d}{dt}\theta = \omega_i + g(t)$, where $\omega_i$ is the "intrinsic" frequency of the oscillator, and $g(t)$ is some time dependent forcing. [57] For circuits of coupled oscillators, we can model the phase of each neuron $\frac{d}{dt}\theta_i = \omega_i + h_{ij}(\theta_{j\neq i})$, where $h_{ij}$ is some function determining the coupling properties from cell $j$ to cell $i$. When $h_{ij}$ is of the form $\frac{K}{N}\sum_{j=1}^{N}\sin(\theta_j - \theta_i)$, where $N$ is the number of neurons and $K$ is a coupling strength parameter, we have the Kuramoto model [92]. Originally developed to model chemical oscillators, this model has found widespread applicability, including neural oscillators [26]. It is often of interest to study, rather than the particular phase of individual neurons, their phase difference meets certain conditions, we can generate the phase models, especially when studying synchronization and pattern formation. These take the form of the difference of phases $\Psi_{ij} = \theta_j - \theta_i$. When cells have similar intrinsic frequencies and $h_{ij}$ meets certain simplifying criteria, we have $\frac{d}{dt}\Psi_{ij} = \varepsilon + h_{ij}(\Psi_{ij})$. Fixed points of this system then represent phase locking.

Another class of neuron models, which are slightly more biorealistic, are the relaxation oscillators. The cannonical relaxation oscillator is the Van der Pol oscillator, given by $\frac{d^2}{dt^2}x - \mu(1 - x^2)\frac{d}{dt}x + x = 0$. $\mu$ here represents a damping force, a dissipation of energy [63]. A modified version of the Van der Pol oscillator is the FitzHugh-Nagumo model, given by $\frac{d}{dt}v = v - \frac{v^3}{3} - w + I_{ext}; \tau\frac{d}{dt}w = v + a - bw$. [67] This system recovers the Van der Pol model when $a = b = 0$ and a coordinate transformation, and can also be considered simplified two dimensional Hodgkin-Huxley system. Of particular importance in these models is the cubic nullcline, which directs the flow through a limit cycle. These models have an important relationship with driving signals, becoming entrained.

In this work, then, we would like to continue examining these forcing signals and the patterns of responses that occur in even more biorealistic settings, particularly using the Hodgkin-Huxley framework, in order to examine more detailed circuit responses. Broadly speaking, this framework takes the form $C\frac{d}{dt}v = -I_{memb} + I_{ext}; \tau_{x^*}\frac{d}{dt}x^* = x_\infty(v) - x$. [56]

Here, $I_{memb}$ is a sum of currents from various ion channels, $I_{ext}$ is an external current, and each $x^*$ is a gating variable for each channel, representing the proportion of channels open at any given time.

## 1.3 Central Pattern Generators and Entrainment to a Periodic Signal

Central pattern generators (CPGs) are simple neural circuits which can produced stereotyped output even in the absence of drive, and are found throughout the animal kingdom in relation to rhythmic action. [133] A notable CPG in humans is the pre-Bötzinger complex, involved in respiration [104]. A critical feature of CPGs is their capacity to modulate their activity in response to external signaling, e.g. changing gait as a response to changing movement speed. They typically function through feedback mechanisms, particularly post-inhibitory rebound. The simplest subunit of CPGs is the half-center oscillator (HCO), consisting of two mutually inhibitory neurons. [134] Each neuron has a fixed behavior which does not vary except through this inhibitory coupling. HCO pattern formation is governed by one of two types of action, escape and release. In escape paradigms, the inhibited neuron will naturally return to its uninhibited behavior, and in release paradigms, the active neuron will stop inhibiting the other neuron. See Figure 1.

In Chapter 2 we will focus on a motor control circuit in the stick insect. Insect locomotion is an active area of interest, with particular applications to cybernetic control mechanisms, and the stick insect is particularly valuable to study due to its large size and the fact that these motor neurons are non-spiking [111], so rather than stable activity patterns, we simply have stable fixed points. Each cell is excitable, so that once some stimulus reaches a threshold, the cell will make a large excursion through phase space before returning to its initial state. The CPG in this stick insect joint is not a true HCO, since in the absence of input each cell remains at its fixed point, but nevertheless has very similar dynamical properties. When driven periodically, the CPG oscillates, may entrain to the period of the forcing, and does so in a manner akin to escape and release mechanisms, dependent on some parameters. While there is a rich dynamical structure to be explored in higher period

pseudoentrainment, we constrain our focus to the regime where the cells are simply entrained to the forcing signal, that is: the duty cycle of the circuit's oscillations approximately matches that of the periodic forcing.

## 1.4  Striatal Response to an Unknown Signal

We then turn our attention to a more detailed neural model within the striatum. The striatum is part of the Cortico-Basal Ganglia-Thalamo-Cortical (CBGTC) loop [101], the major pathway for action selection and reinforcement learning. See Figure 2. The striatum is an important part of this loop as the first node between the cortex and the rest of the basal ganglia. Dysfunction in the striatum has been implicated in a number of movement and behavioral disorders, including, but not limited to: Parkinson's disease, Tourette's Syndrome, Huntington's Disease, autism, depression and addiction. [90] [95] [135] [93] [103]

In this work, we will be focusing on the role the striatum plays in generating motor tics, a prevalent symptom of Tourette's Syndrome. Major work has been done modeling striatal action, both in the larger BG circuit of the direct-indirect-hyperdirect action selection pathway, and in the striatum itself, particularly in the context of Parkinson's Disease. In Parkinson's, patients often present elevated beta rhythms (neural oscillations between 12 and 30 Hz) due to synchronization of the primary output neurons of the striatum, the spiny projection neurons (SPNs) [142]. Some of this work has led to a growing appreciation of the tonically active cholinergic interneurons (TANs), a major source of acetylcholine in the striatum, which are believed to play a role in striatal output, as well as reinforcement learning through interactions with dopamine [22]. Despite this growing interest, the complex variety of behavior observed in TANs has caused modeling to lag behind, a gap that we hope to fill.

Thus, we build a biorealistic spiking model of a TAN using the Hodgkin-Huxley framework. To do this, we found experimental literature suggesting the presence of a variety of functional channels, dynamic ion concentrations, and included a mechanism to include transient changes to neuromodulator activity, for a total of a 16-dimensional system for this cell model, and incorporated it into a simple striatal circuit in order to compare this circuit to
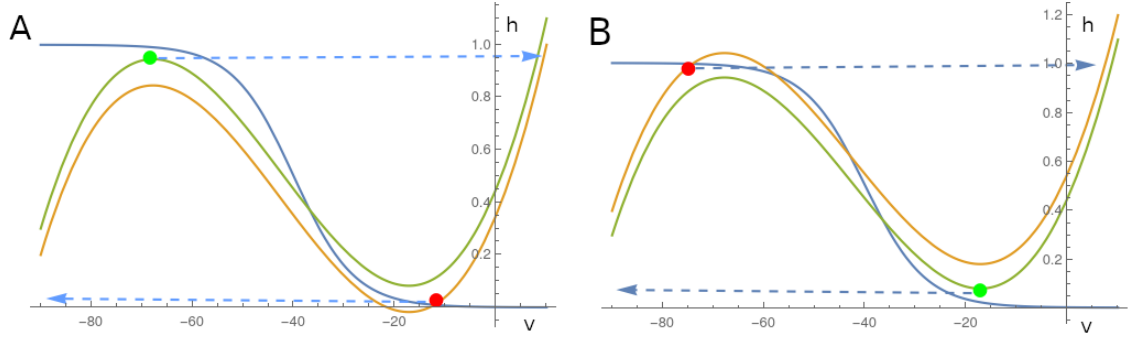
Figure 1: **Escape and Release Mechanisms. A:** Escape Oscillations. The active cell moves along the right branch of the orange (uninhibited) nullcline until it reaches its fixed point (red dot). The inhibited cell moves along the green (inhibited) nullcline until it reaches the knee (green dot). The cell then escapes inhibition, becomes active and inhibits the other cell, which now follows the left branch of the green nullcline. **B:** Release Oscillations. The quiescent cell follows the left branch of the orange (inhibited) nullcline until it reaches its fixed point (red dot). The active cell follows the right branch of the green (uninhibited) nullcline until it reaches the knee (green dot). The cell then moves to its quiescent phase, releasing the quiescent cell, which becomes active, and follows the right branch of the green nullcline.
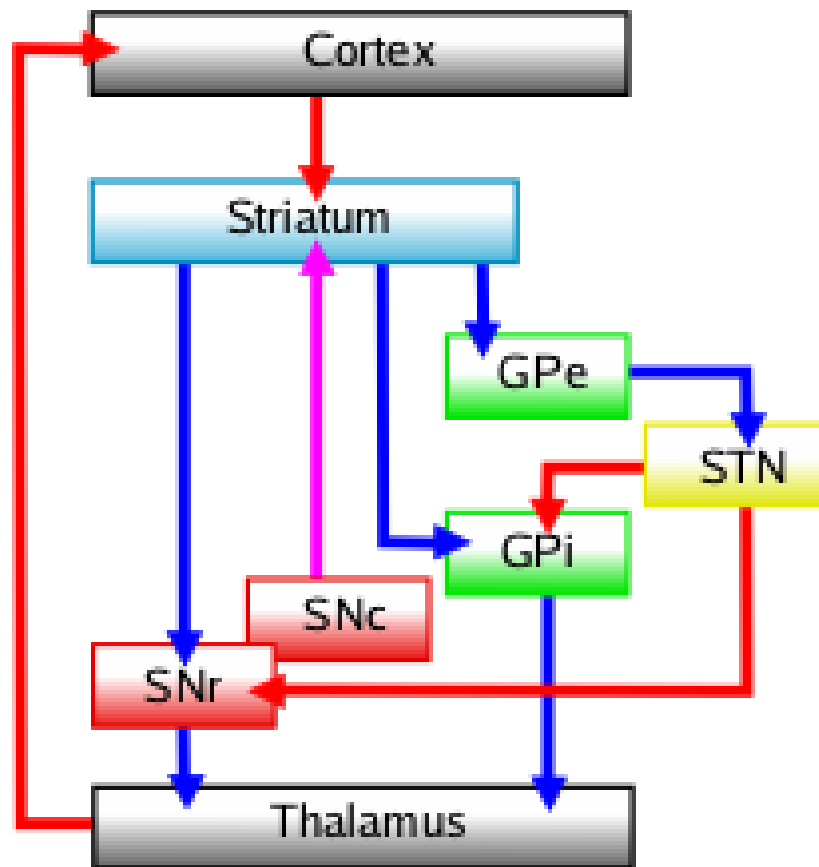
Figure 2: **Cortico-Basal Ganglia-Thalamo-Cortical Loop**. The flow of activity from the cortex, through the basal ganglia into the thalamus, and back to the cortex. Notice that the striatum is the primary node between the cortex and the rest of the basal ganglia. Created by Andrew Gillies, CC BY-SA 3.0 via Wikimedia Commons

experimental data from the striatum during motor tic events. Although the striatum has a rich fauna of neurons directly impacting SPNs, and the SPNs themselves have a rich network structure, virtually all signalling is done through GABA, which is blocked by bicuculline, so our experimental circuit may be reduced to only TAN and SPN [141]. Rather than a typical neural circuit, coupling between cells is through the presence of neuromodulators rather than synaptic transmission. These neuromodulators impact the firing properties of cells by altering their intrinsic mechanisms as opposed to directly impacting the voltage equation. [54]

Furthermore, we no longer know the details of the forcing signal: there is a sudden shift in the dynamics of the system, suggesting forcing, but the details of this process are unknown. Solving this kind of inverse problem is often involved and complex, but we are in luck: signals of this type are often seen in one of a handful of profiles. We may use these profiles as an ansatz, and constrain these candidate profiles based on the circuit response. An interesting feature of this circuit is the action of the neuromodulator on the forcing signal itself. Receptors are known to be present, but the specific action on the signal is unclear, so we additionally investigate what impact this feedback may have.

## 1.5   Sustained Forcing and Chaos

In the TAN model we developed, we find that when forcing is both sustained and subject to neuromodulator feedback, the model enters a state of deterministic chaotic firing. To put it simply, this means the spiking pattern of model is somewhat random, and this randomness is *not* the result of noise in the system. [29] More concretely, our system is sensitive to initial conditions, which means that very small differences in an initial state can accumulate and result in very dramatic differences at some later time. A classical example of a system exhibiting chaos is the logistic map, given by $x_{n+1} = \mu x_n(1 - x_n)$ [131]. The logistic map is often used to model simple population dynamics, capturing reproduction and death as a proportion of the current population. [94] To understand the evolution of of the system, it is often helpful to analyse fixed points, here given by $x^* = \mu x^*(1 - x^*)$, where some simple

algebra gives us that $x^* = \frac{\mu-1}{\mu}$. When $\mu < 1$, these fixed points are negative, so we may discard them as unrealistic, but when $\mu > 1$ we can examine the stability of this fixed point through a cobweb diagram, see Figure 3A-C, and see that an interesting pattern of behavior emerges: when $\mu < 3$, the fixed point is stable, when $3 < \mu <\sim 3.4$, the system bounces between two values, and if $\mu >\sim 3.4$, the system bounces between four values. If we track these values for each value of $\mu$, we obtain the bifurcation diagram in Figure 3D, and see that this period doubling trend continues until we reach a point where our values are apparently random, as the oscillation reaches infinite period. We can find these period doubling events in a more systematic way, by computing the eigenvalues of the fixed points of the $2^{nth}$ iterates of the map. (i.e. fixed points of $x_{n+1}, x_{n+2}, x_{n+4}$ etc.)

This period doubling cascade is a common route chaos [19], so returning to our model, we might expect to find a similar process occurring as we increase the strength of the forcing signal. In the interest of computational tractability we reduce our model to only its key features, and although our model is a flow, not a map, we may use the theory of Poincaré maps to convert our model appropriately.
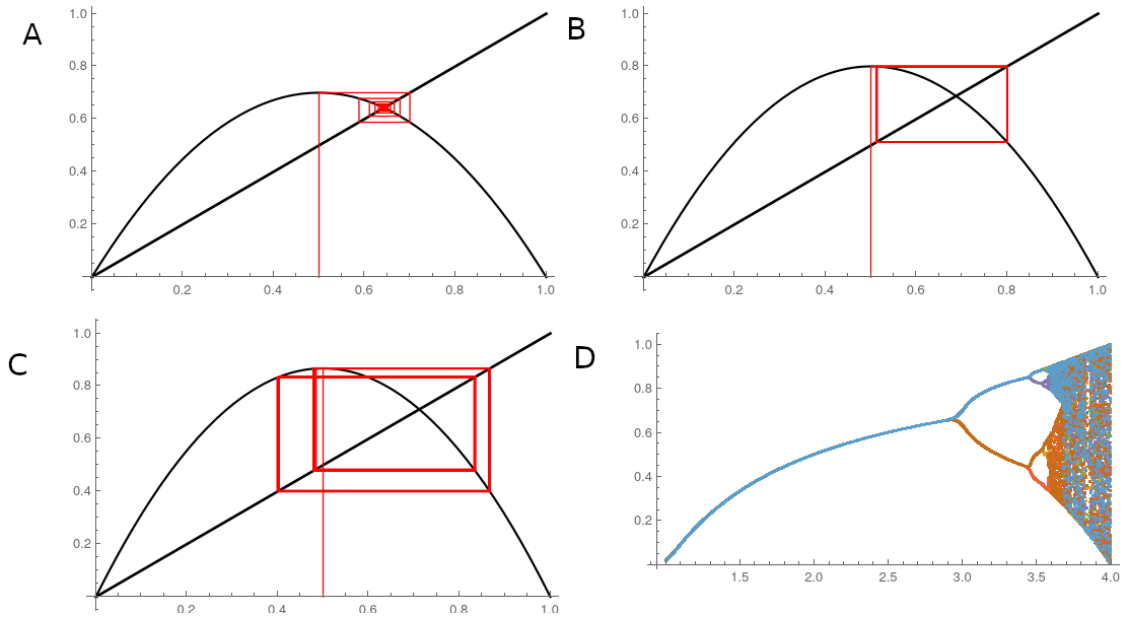
Figure 3: **Period Doubling Bifurcations in the Logistic Map. A-C:** The red trace shows the cobweb diagram as the parameter increases through period doubling bifurcations. **D:** The bifurcation diagram. Each point in the diagram shows the points the map oscillates between for a fixed parameter value on the x axis. The coloring is included to illustrate different branches.

## 2.0   Stick Insect Motor Control Circuit


### 2.1   Introduction


The rhythms underlying locomotion are believed to be generated by neural central pattern generator (CPG) circuits ([137, 37, 117, 87]; for overview, see also [124, 102]). Following this hypothesis, CPG behavior is influenced by top-down neural commands and sensory feedback from muscles and limbs (for review see e.g. [6, 27]). CPG outputs are then processed by other interneurons and eventually drive motoneurons responsible for muscle activation. Coordinating all of these components to yield rhythmic movements of limb segments at particular joints is complex; however, segments within limbs must also be coordinated, as must multiple limbs, for limbed locomotion to emerge. Depending on the given behavioral task or the speed of locomotion, insects generate different interlimb coordination patterns during walking ([116, 58, 121, 118, 51, 15, 60]) ranging from "wave or metachronal gait" at very low speeds ([15, 35, 53]) to tetrapod and tripod coordination patterns at low-to-intermediate and higher speeds ([118, 15, 53]). Information on the underlying neural mechanisms and the contribution of central and peripheral signaling in CPG entrainment and its contribution to this highly flexible interlimb coordination still remains elusive.

In this work, we try to address this problem by considering a small component of this rhythm generation and coordination process in the stick insect *Carausius morosus*, using a minimal computational model and dynamical systems analysis. Stick insect legs feature three segments, each with a corresponding joint and antagonistic muscle pair (Figure 4, [18]). The sensory signals to each segment within a leg are determined in part by the mechanical loading of the leg and ground contact forces, where direct mechanical coupling between joints is negligible during the swing movement of the leg [11], and movement-related signals from muscles and other segments of that leg also contribute. Extensive experimental investigations have produced a hypothesized chart of influences between stick insect leg segments [5] which have successfully been implemented into a mathematical model controlling some basic aspects of the movement of a stick insect leg [126, 129, 127, 122, 125]. These results imply that in the

10

transition from swing to stance phase, depressor muscle activity and coxa-trochanter joint signals impact the thorax-coxa (ThC, hip-like) joint control system, promoting retractor muscle activation.

Our focus here is a model of the ThC joint control system featuring a half-center oscillator CPG and a pair of interneurons (INs) that impact the CPG, along with drive signals. These drives consist of a time-periodic signal to one of the INs, representing ascending depressor input (i.e. loading of the leg and ground contact) during stepping, and independent constant currents to the CPG units, representing top-down drive from higher neural command centers, which could theoretically be used to initiate movement or to tune its properties (e.g., initiate faster walking or turning). Outputs from this system control the contraction of the protractor and retractor muscles. Stick insects engage in a variety of different walking patterns consisting of a continuum of stable patterns ranging from metachronal to tripod and tetrapod coordination patterns [34] and including curve walking and backward stepping of single legs. These occur at different frequencies, and depressor muscles are active during different fractions of each period in these different coordination patterns. To start with here we focus on the two most commonly observed coordination patterns from among this continuum in insects: tetrapod and tripod. To account for the differences pointed out above we will consider forms of depressor input representing these two coordination patterns. Furthermore, the impact of sensory versus central influences in the coordination of leg movements is different for tetrapod and tripod walking. During tetrapod walking the stick insect walks slowly and relies heavily on sensory feedback signals to coordinate its movements. If walking speed increases the animal transitions to tripod walking, which is commonly assumed to rely less on sensory information due to the increased influence of the central drive [6, 12, 7, 109]. In this study we are interested in the mechanisms underlying the entrainment of rhythmic activity in the CPG dependent on the interaction of these ascending and top-down drive signals.

The remainder of the paper is organized as follows. In Section 2.2, we present the model on which we focus, both schematically and mathematically. We also go on, in subsection 2.2.3, to describe the methodology of how we consider entrainment in the ThC joint control system, first at the level of the interneurons and next at the level of the core CPG. Section

2.3 presents our analysis of entrainment, again starting from the interneurons and progressing to the CPG. In the latter case, in subsection 2.3.2, we consider a variety of ways that entrainment to the tetrapodal rhythm can be lost under parameter variations and additional signal modifications that can lead to recovery of entrainment. In subsection 2.3.3, we show how similar ideas can apply to additional scenarios including the loss of some signaling pathways, changes in the baseline CPG configuration, and switch to tripodal walking patterns. The paper concludes with a discussion in Section 2.4.

## 2.2    Methods

In this section, we present the mathematical details of the model that we consider. We also define *entrainment* of model units, which is the behavior of interest in our analysis, and present the methods used to assess the success, breakdown, and recovery of entrainment under variation of various model parameters.

### 2.2.1   ThC Network

We consider the network shown in Figure 5, which is based on experimental data of and reasonable neurophysiological assumptions made for the stick insect walking system as well as on numerical simulations [126, 129, 128]. The core of this network is the CPG, which controls the activity of the protractor and retractor MNs and muscles (for experimental details on the neural networks mediating coordination of multisegmental organs see [5]). Its function is affected by the input from the peripheral sense organs via the interneurons (INs) IN3 and IN4. The effect of the sensory input is of dual nature: it excites the "retractor" CPG neuron (C1) directly via IN4 but inhibits the "protractor" CPG neuron (C2) via an additional inhibitory interneuron, IN3. This part of the network was constructed on the basis of experiments [3] and accompanying simulations [8] made for the neural network controlling the antagonistic levator-depressor muscle pair of the stick insect leg. We assume that essentially the same system can be applied to control any other antagonistic muscle

12
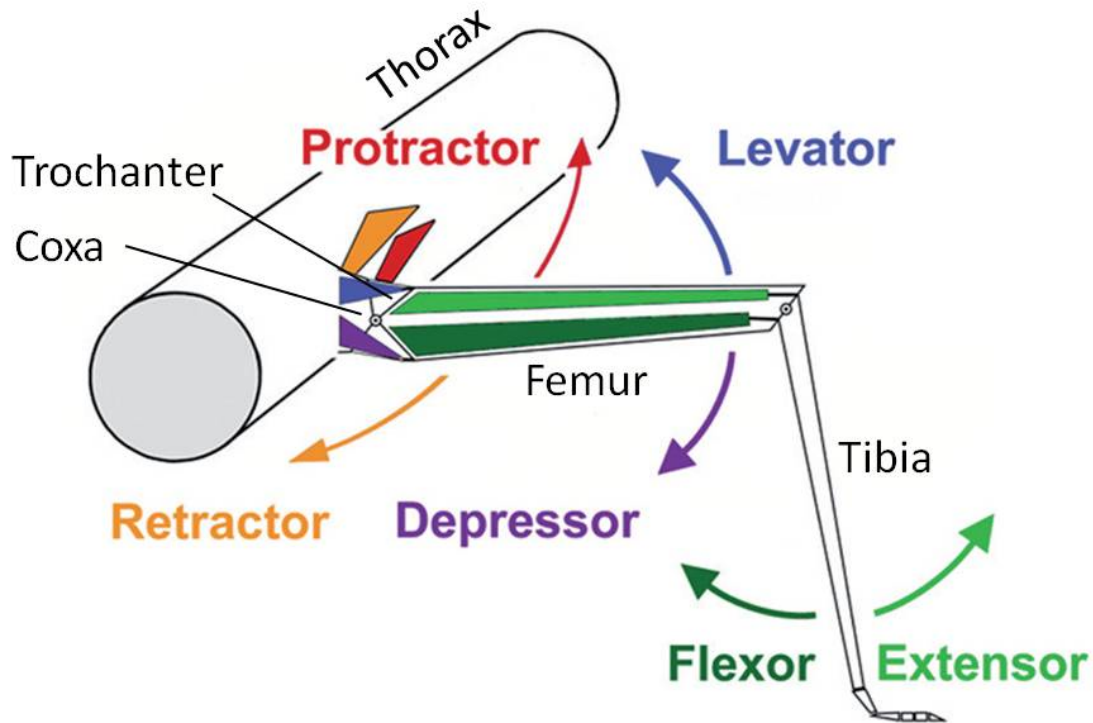
Figure 4: **Scheme of a stick insect leg.** Three antagonistic muscle pairs drive the movement of the leg: at the thorax-coxa joint, protractor and retractor muscles (red and orange) are responsible for moving the leg fowards and backwards; at the coxa-trochanter joint, levator and depressor muscles (blue and purple) control the upward and downward movements; and at the femur-tibia joint, the flexor-extensor muscle pair (dark and light green) moves the leg inward and outward.

pair of the stick insect leg. It therefore constitutes a network that, in its basic properties, is likely to be close to that present in the stick insect.

An excitatory periodic signal $\beta(t)$ with period $\tau$ is used to represent the depressor input and also to implicitly represent inter-leg coupling signals. Specifically, while $\beta(t)$ mainly represents the loading and unloading of the same leg, which controls the activity of the ThC joint under study (intra-leg coupling), $\beta(t)$ also implicitly includes inter-leg coupling signals: in the large-scale network model of Toth and Daun [125], inter-leg coupling is given through the coupling of the CPGs that control the Coxa-trochanter joint of the ipsilateral neighboring legs, which in turn impact $\beta(t)$. The signal $\beta(t)$ provides constant drive to interneuron IN4 for a fraction $\alpha$ of each period and no drive for the remaining part of the period. Different values of $\alpha$ correspond to different leg coordination patterns. The choice $\alpha = 3/4$ is consistent with a step cycle during tetrapod walking, while $\alpha = 1/2$ corresponds to tripod walking.

IN4 itself may be in an active or an inactive phase. While IN4 is in its active phase, it provides excitatory drive to interneuron IN3 and to CPG neuron C1. The dynamics of IN3 is nearly identical to that of IN4, but with drive provided by IN4 during its active phase rather than by $\beta$. In the absence of drive, both IN3 and IN4 are excitable, with a stable fixed point at a relatively hyperpolarized voltage corresponding to the silent phase. We assume a choice of drive levels such that IN3 and IN4 remain excitable when driven; nonetheless, drive does lower the activation threshold for these neurons. When the drive from IN4 activates IN3, the latter also exhibits active and inactive phases and sends inhibitory drive to CPG neuron C2 while active. Each cell in the CPG system receives three inputs: reciprocal inhibition from the other CPG neuron, bottom-up input from either IN4 or IN3 resulting from their responses to the depressor signal, and top-down excitatory input. The excitatory inputs to the CPG units C1 and C2 would be modulated in part by inter-leg coupling. Central influences between the ThC systems of the legs of the stick insect which are modulated by sensory feedback of the individual legs are known to exist ([2, 1], modelled in [119]). In particular, a single stepping leg is able to induce tonic or even rhythmic activity in the protractor and retractor motoneurons of the neighboring legs. The CPG system is initially tuned to match experimental data, such that in the absence of input, C1 has a fixed point at

a hyperpolarized voltage, corresponding to its own silent phase, and C2 has a fixed point at a depolarized voltage, corresponding to tonic activation. In a successful tetrapodal rhythm at the level of the CPG, C1 and C2 exhibit periodic behavior, with C1 active for $\sim$3/4 of each cycle (corresponding to the retraction phase) and C2 active for the other $\sim$1/4 of each cycle (corresponding to the protraction phase), matching the $\beta$ cycle.

### 2.2.2 Model Equations

Each CPG component (C1, C2) and each IN (IN3, IN4) is modeled with a pair of ODEs for voltage ($v$) and the inactivation of an inward current ($h$). The voltage equations, while posed in the Hodgkin-Huxley framework, are relatively simple because the relevant neurons are non-spiking [4]; the equations feature only a leak current, a slowly inactivating inward current that we represent as a persistent sodium current, and input terms. Some of these inputs correspond to synaptic connections between neurons. We model each synaptic activation level as a steep sigmoidal function of presynaptic voltage, with an activation threshold. Additional input terms correspond to the time-periodic drive to IN4 from the depressor unit and the top-down signals to C1 and C2, taken as excitatory synaptic inputs with constant conductances. The voltage nullcline for each neuron is either cubic or monotone, depending on the combined inputs that the neuron receives, and the nullcline of each $h$ equation is sigmoidal.

The equations for the voltages $v_1, v_2$ of C1, C2 and $v_3, v_4$ of IN3, IN4 take the form

$$C_{m_j} v'_j = -I_{ion_j} - I_{input_j}. \tag{1}$$

In equation (1),

$$I_{ion_j} = g_{Na} m(v_j) h_j (v_j - e_{Na}) + g_{L_j} (v_j - e_L)$$

for

$$m(v_j) = (1 + \exp[(v_j - \theta_{Na})/\sigma_{Na}])^{-1}.$$
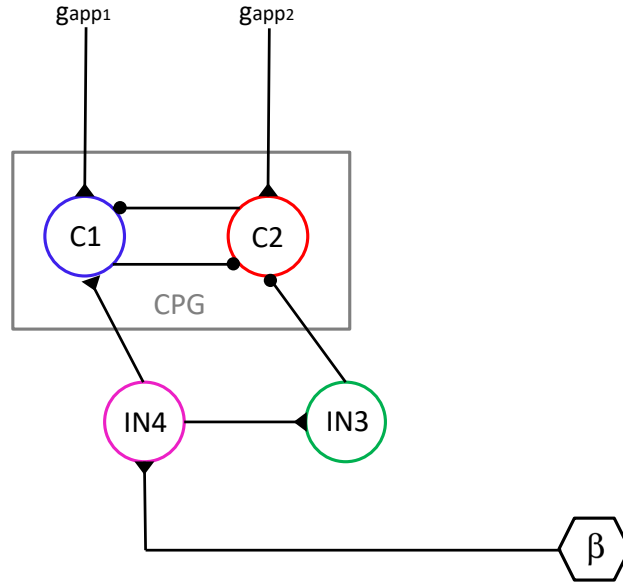
Figure 5: **Thorax-coxa (ThC) joint control system.** Rhythmic activity of the ThC joint is controlled by a CPG that receives depressor input $\beta$ representing sensory feedback signals about loading of the leg and ground contact, transmitted via a pair of interneurons (IN), as well as descending signals $g_{app1,2}$. Connections denoted by triangles are excitatory, while those indicated by circles are inhibitory. For further details see [129].

Moreover,

$$
\begin{aligned}
I_{input_1} &= g_{app_1}(v_1 - e_{syn_e}) + g_{cpg}s_{cpg}(v_2)(v_1 - e_{syn_i}) \\
&+ g_{syn_{41}}s_{41}(v_4)(v_1 - e_{syn_e}) \\
I_{input_2} &= g_{app_2}(v_2 - e_{syn_e}) + g_{cpg}s_{cpg}(v_1)(v_2 - e_{syn_i}) \\
&+ g_{syn_{32}}s_{32}(v_3)(v_2 - e_{syn_i}) \\
I_{input_3} &= g_{syn_{43}}s_{43}(v_4)(v_3 - e_{syn_e}) \\
I_{input_4} &= g_{app_4}\beta(t)(v_4 - e_{syn_e})
\end{aligned}
$$

where $g_{app_i}$ denote top-down input strengths, $g_{cpg}$ is the strength of coupling between the CPG units, $g_{syn}$ parameters quantify the strengths of other synaptic inputs in the system, $\beta(t) = H[\sin(2\pi t/\tau - \Gamma) - \gamma]$ for $H[x]$ the Heaviside step function, and

$$
s_{ij}(v_i) = (1 + \exp[(v_i - \theta_s)/\sigma_{s_j}])^{-1}
$$

for each $s_{ij}$ function in the system; note that the $\sigma_{s_j}$ depends on the target cell $j$, whereas $v_i$ corresponds to the source cell $i$. These expressions are accompanied by the inactivation equations

$$
h'_j = \varepsilon_j(h_{\infty_j}(v_j) - h_j)\cosh[(v_j - \theta_\tau)/\sigma_\tau] \tag{2}
$$

with

$$
h_{\infty_j}(v_j) = (1 + \exp[(v_j - \theta_{h_j})/\sigma_{h_j}])^{-1}.
$$

The baseline parameter values used throughout this paper are listed in Table 1. Relevant units are provided there; to avoid clutter, we omit these in figure labels. Rather than four distinct $\epsilon_j$ values, we set $\epsilon_1 = \epsilon_2 =: \epsilon$ and $\epsilon_3 = \epsilon_4 =: \epsilon_{IN}$. Moreover, we note that $0 < \varepsilon_j \ll 1$ for all $j$, such that the $v_j$ dynamics is much faster than the $h_j$ dynamics. Thus, system (1)-(2) can be viewed as a fast-slow system. Although it is a system with 4 fast and 4 slow variables, we can visualize its dynamics by considering projections to each $(v_j, h_j)$ plane. In this view, system trajectories will spend most of their time drifting in a small neighborhood of attracting parts of the $v_j$-nullclines on the slow ($\mathcal{O}(\varepsilon_j)$) timescale of equation (2), interrupted by fast jumps, on the $\mathcal{O}(1)$ timescale of equation (1), between these attractors.

### 2.2.3 Entrainment

We define entrainment separately for the interneurons and the CPG. For each interneuron, we say it is entrained if for each cycle of the $\tau$-periodic signal $\beta(t)$, the interneuron has one active and one quiescent phase, and the interneuron itself exhibits $\tau$-periodic behavior. We say the interneuron is quasi-entrained if for each cycle of $\beta$, the interneuron has one active and one quiescent phase, and its behavior is $2\tau$-periodic but not $\tau$-periodic. It may be possible to have higher-order quasi-entrainment, featuring periods that are larger integer multiples of $\tau$, but the associated regions of parameter space are too narrow to robustly identify, so we do not pursue this possibility. We say the interneuron is not entrained if it does not have one active and one inactive phase per $\beta$ cycle. In the CPG system, the units drive motoneurons that induce muscle contraction, and functional rhythms should feature minimal protractor and retractor co-contraction. Thus, we say that the CPG is entrained if each of C1, C2 has one active and one inactive phase per $\beta$ cycle, the activity pattern is $\tau$-periodic, and the duration of simultaneous C1, C2 activity is below a small time threshold. We consider simultaneous inactivity as allowable for entrainment since time periods lacking both protraction and retraction are functionally acceptable. For an example of a fully entrained state, see Figure 6.

#### 2.2.3.1 *Entrainment of IN4*

To compute entrainment regions in parameter space, we separate IN4, IN3 and the CPG system C1 and C2. We consider both tetrapodal and tripodal walking patterns, distinguished by their duty cycles, 3/4-1/4 and 1/2-1/2, respectively, although we mostly focus on the tetrapodal case because the ideas involved in the tripodal analysis are similar. For IN4, we use a time-$\tau$ map that starts from the cycle phase corresponding to the onset of $\beta$ drive and ends at time $\tau$ later, just before $\beta$ turns on again, corresponding to one full $\beta$ cycle. To compute the entrained solution, we wish to find an initial condition $(v_4(0), h_4(0))$ for equations (1),(2), specifically for $j = 4$, on the active branch of the driven $v_4$-nullcline such that $(v_4(\tau), h_4(\tau)) = (v_4(0), h_4(0))$. In practice, we search for such initial conditions numerically. To do so, it suffices to take any initial condition $(v_4, h_4)$ near the active branch
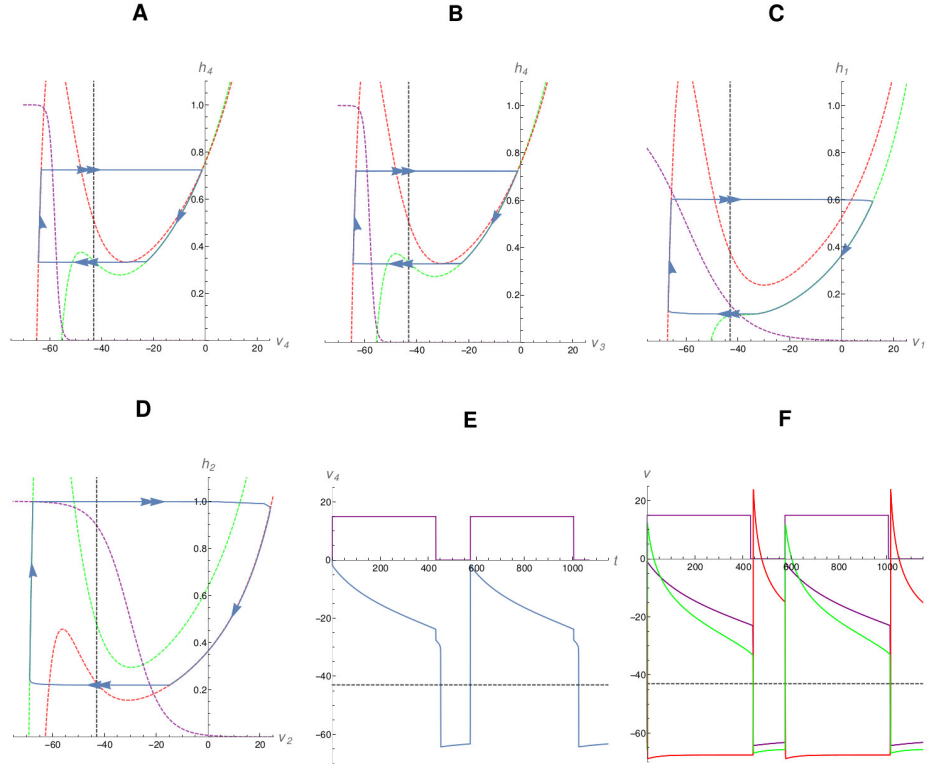
Figure 6: **The baseline entrained state for the full system in the tetrapod rhythm.** **A-D:** $(V, h)$-phase planes for IN4 (A), IN3 (B), C1 (C), C2 (D). Each green (red) dashed curve is a $V$-nullcline with the $\beta$ signal turned on (off). The purple dashed curves indicate the $h$-nullclines for the cells, and the vertical dashed black lines mark the synaptic threshold. The blue curves are projections of the model trajectory onto the four phase planes. The $\beta$ signal lowers the voltage nullcline for all cells except C2 (D). **E:** Voltage time course of IN4 (blue) along with the pattern of drive from $\beta$ (purple), enlarged for clarity. Note that IN4 inactivates slightly after the signal from $\beta$ ends. **F:** Voltage time courses of IN3 (gold), C1 (red), and C2 (green), along with $\beta$ (purple). The inactivation of IN3 and C1 and the activation of C2 occur simultaneously, shortly after the end of the $\beta$ signal, due to propagation of the delayed inactivation of IN4. In this example, C1 and C2 activations are complementary. In (E-F), the horizontal dashed black line indicates synaptic threshold.

of the driven $v_4$-nullcline, in the basin of attraction of the active branch under equation (1) with $h_4$ fixed, since the resulting trajectory will approach a small neighborhood of the $v_4$-nullcline on the fast timescale. Moreover, we find it most effective to break the process up into pieces, first using a boundary value solver to find a solution with $h_4(\tau) = h_4(0)$, without worrying about $v_4(\tau)$. Once we find such a solution, two additional conditions are necessary and sufficient for the trajectory we have identified to represent a stable entrained solution: knee clearance and stability. For relevant strengths of input, the $v_4$-nullcline is cubic-shaped and can be viewed as the concatenation of three branches on each of which $v_4 = v_4(h_4)$, the most negative and middle of which meet in a left knee $(v_{lk,4}(\beta), h_{lk,4}(\beta))$ and the most positive and middle of which meet in a right knee $(v_{rk,4}(\beta), h_{rk,4}(\beta))$, where we have indicated explicitly that these knee coordinates depend on $\beta$. The knee condition is that $h_4(0) > h_{lk,4}(1)$, since $\beta(t) = 1$ when drive is on. This condition ensures that when $\beta$ turns on again to start the next $\tau$-cycle, the IN4 neuron will be able to activate in response (Figure 7). The stability condition is simply that there exists a neighborhood $U$ of $(v_4(0), h_4(0))$ such that all trajectories $(v(t), h(t))$ with initial conditions in $U$ have $|h(\tau) - h_4(\tau)| < |h(0) - h_4(0)|$; we focus on the $h$ coordinates, since we can choose $U$ such that all trajectories under consideration lie arbitrarily close to the $v_4$-nullcline at time $\tau$.

Once we identify a stable solution, we are interested in its basin of attraction. Certain solutions that start far from the entrained orbit may fail to become entrained and instead repeatedly become caught on the left branch of the driven $v_4$-nullcline (e.g., Figure 7B). To compute the upper bound $h_{4,upper}$ on the basin of attraction, we find an initial height $h_4^*(0)$ and corresponding solution $(v_4^*(t), h_4^*(t))$ such that $h_4^*(\tau) = h_{lk,4}(1)$, and set $h_{4,upper} = h_4^*(0)$. Next, for $h_{4,lower}$, we find $h_4^\dagger(0)$ such that $h_4^\dagger(\tau) = h_{4,upper}$, and we set $h_{4,lower} = h_4^\dagger(0)$. Since the map from $h_4(0)$ to $h_4(\tau)$ is monotone decreasing, this map has a unique fixed point in $(h_{4,lower}, h_{4,upper})$, and since we already checked stability, we know that this fixed point is stable. Thus, the interval $(h_{4,lower}, h_{4,upper})$ gives us an approximation to the basin of attraction for the fixed point; although this could be an overestimate, our numerics suggest that the dynamics contracts in $h_4$ within this interval, and hence the interval truly represents the basin.

If the periodic solution does not satisfy the stability condition, then there may be a stable
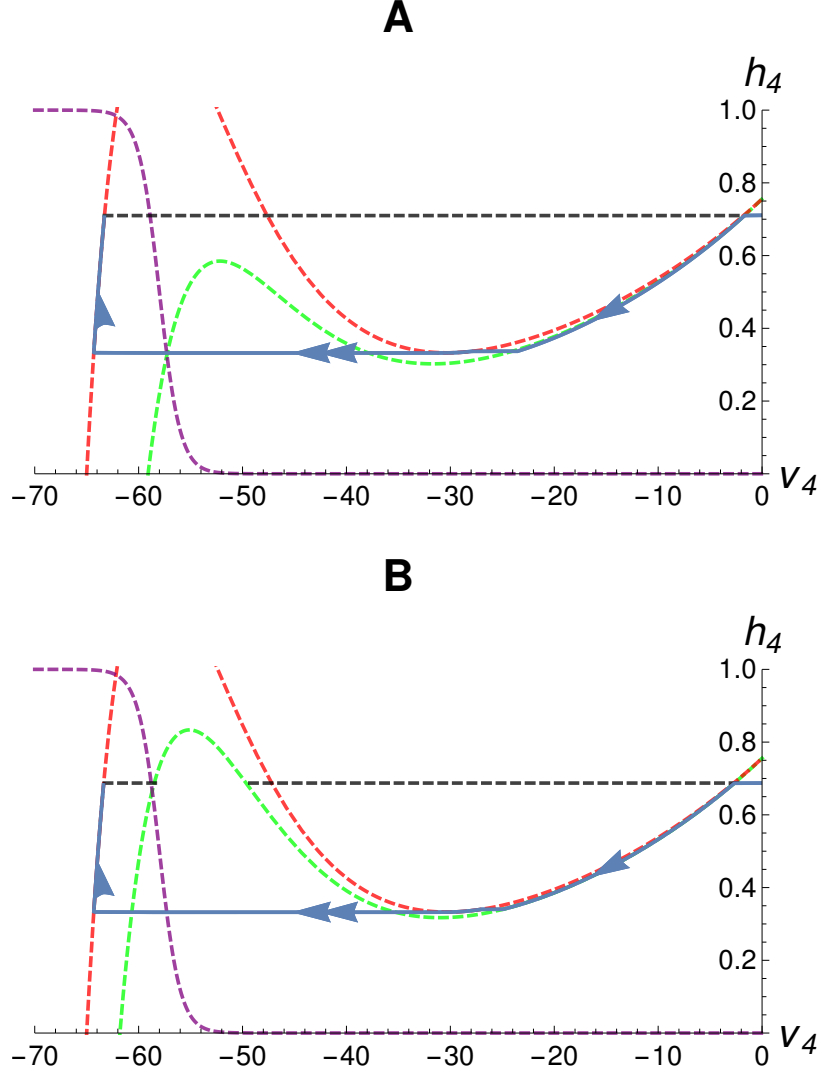
Figure 7: **An illustration of knee clearance. A:** When the trajectory with $h_4(\tau) = h_4(0)$ satisfies $h_4(\tau) > h_{lk,4}(1)$ (as indicated by the horizontal dashed black line), the left knee of the driven nullcline (green) is successfully cleared when $\beta$ activates, and entrainment is thus possible. **B:** Similarly, when $h_4(\tau) = h_4(0) < h_{lk,4}(1)$, the knee is not cleared (horizontal black dashed line) when $\beta$ turns on (i.e., when $\beta(t) = 1$), causing the cell to remain quiescent and preventing entrainment. Color coding of nullclines follows Figure 6. Arrows denote the direction and relative speed of the flow (one arrow: slow, corresponding to $h_4$ dynamics; two arrows: fast, corresponding to $v_4$ dynamics).

solution that is either quasi-entrained or unentrained. How can the stable quasi-entrained solution occur? Let $(v_p(t), h_p(t))$ denote the unstable periodic solution. Suppose that on each cycle, $\beta(t)$ is activated for $t \in [0, \eta\tau) \mod \tau$, where $0 < \eta < 1$. Also, assume that $h_p(t) > h_{rk,4}(0)$, such that the periodic solution is active, for $t \in [0, \eta_p\tau) \mod \tau$ with $\eta_p \in (\eta, 1)$, and that $h_p(\eta_p\tau) = h_{rk,4}(0)$; that is, the solution is caught on the right branch of the $v_4$-nullcline corresponding to $\beta = 0$ ($\beta$ off) for time $t \in (\eta\tau, \eta_p\tau) \mod \tau$. Now, consider a perturbation to the unstable periodic solution; specifically, for the perturbed solution $(\hat{v}(t), \hat{h}(t))$, take an initial condition $(\hat{v}(0), \hat{h}(0)) = (v_p(0), h_p(0) + \delta h)$ for $0 < \delta \ll 1$, which lies at a larger $h_4$ value than that of the periodic solution at time 0. We have $\hat{h}(\eta\tau) > h_p(\eta\tau)$, and hence $\hat{h}(\eta_p\tau) > h_p(\eta_p\tau) = h_{rk,4}(0)$. Thus, the perturbed solution jumps down at time $\hat{\eta}\tau > \eta_p\tau$, and we have $h'_p(t) > 0, \hat{h}'(t) < 0$ for $t \in (\eta_p\tau, \hat{\eta}\tau)$ such that $\hat{h}(\hat{\eta}\tau) = h_{rk,4}(0) < h_p(\hat{\eta}\tau)$. The perturbed and periodic trajectories cannot cross on the 1-dimensional left branch of the $v_4$-nullcline in the silent phase, and hence $\hat{h}(\tau) < h_p(\tau)$, when $\beta$ turns on and the cycle ends. In other words, a perturbed solution that starts above the unstable periodic orbit ends up below the unstable periodic orbit after one $\beta$ cycle.

Similar reasoning gives us $\hat{h}(\tau) > h_p(\tau)$ at the end of the next cycle. That is, the perturbed trajectory alternates cycles where it lags the unstable periodic solution with cycles where it leads. This mechanism can give rise to a $2\tau$-periodic quasi-entrained solution (for example, see Figure 8). Moreover, a similar line of argument shows that such a $2\tau$-periodic orbit must involve a time interval spent on the right branch of the undriven $v_4$-nullcline, an interval spent on the left branch of the driven $v_4$-nullcline, or both. Finally, in the absence of $2\tau$-periodic quasi-entrained behavior, we can observe more complicated patterns featuring higher-order entrainment or apparent lack of entrainment, but we do not pursue these non-robust cases in this work.

In the tripodal case, it happens that IN4 may meet the entrainment criteria, but the duty cycle drifts quite far from that of $\beta$, so we additionally require that the duty cycle remains within 10% of that of $\beta$ for a solution to be considered entrained.

22

**A**



**B**
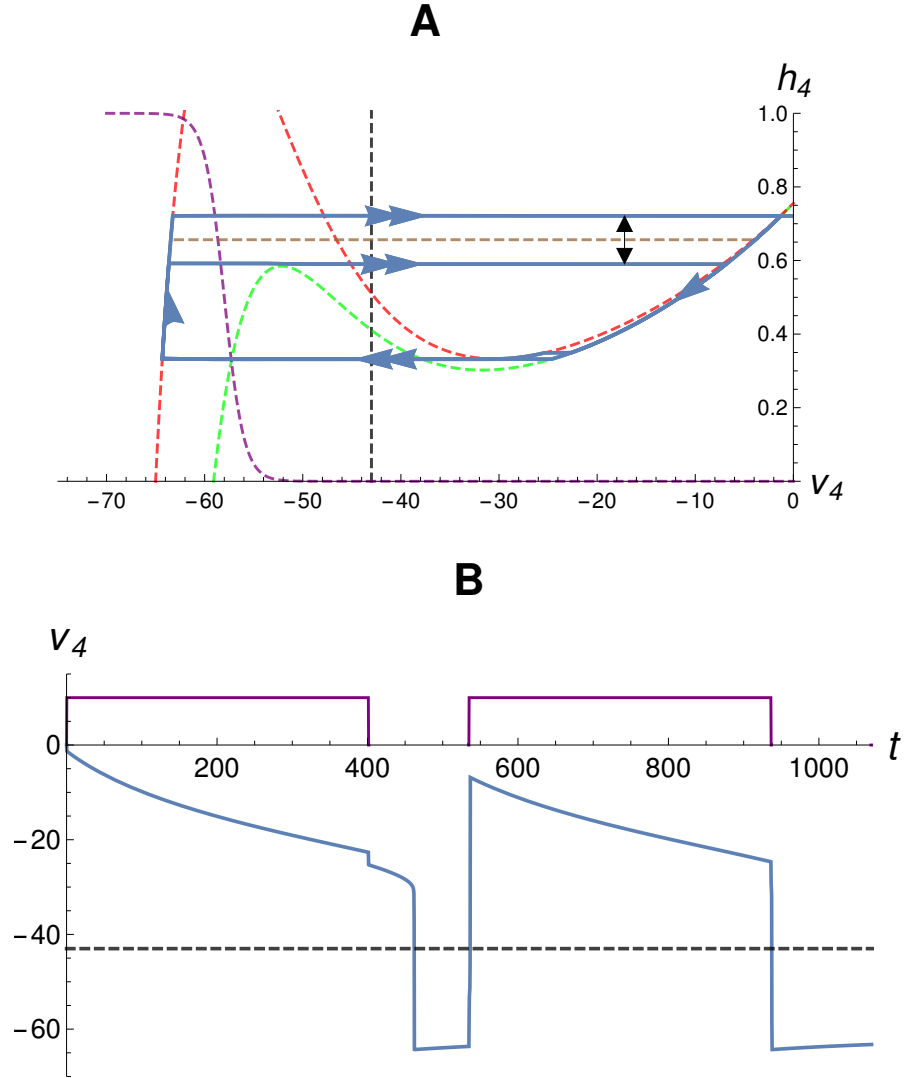


Figure 8:  **Quasi-entrainment of IN4.**  **A:** When the periodic solution (dashed brown) is unstable, we may have quasi-entrainment.  If drive is low enough, this instability can cause a failure of entrainment as the $h_{lk,4}(1)$ (green) moves up.  Nullclines are as before, with the dashed black line indicating the synaptic threshold.  Note that the quasi-entrained trajectory (blue) spends some time on the right branch of the undriven $v_4$-nullcline (red) on every second cycle.  B: Voltage trace of the quasi-entrained state.  The purple curve is the activity of $\beta$, enlarged for visibility.  The dashed black line indicates synaptic threshold.  When the trajectory spends time on the right branch of the undriven $v_4$-nullcline, the active phase of IN4 lasts beyond the time when $\beta$ shuts off.

23

**2.2.3.2** *Entrainment of IN3*

With the description of entrainment of IN4 complete, we briefly turn our attention to IN3. The equations for IN3 are identical to those for IN4 except that $I_{input_3}$ depends on $s_{43}(v_4)$, the input from IN4, rather than on $\beta(t)$. Thus, entrainment, or lack of entrainment, in IN3 will be dictated by that of IN4 together with the strength of drive from IN4 to IN3. We consider three cases as the regimes where functionally relevant activation patterns may occur. First, if IN4 is entrained and provides strong drive to IN3, then IN3 will be entrained, and any lag in the time when IN4 shuts off relative to the offset of $\beta$ yields continued drive to IN3, so shutoff of IN4 and IN3 will be simultaneous. Second, if IN4 is entrained and provides weak drive to IN3, then IN3 will enter a quasi-entrained state. Third, if IN4 is quasi-entrained and provides strong drive to IN3, then IN3 will follow its drive and become quasi-entrained as well.

**2.2.3.3** *Analysis of the CPG*

To compute entrainment profiles for the CPG, we vary parameters over a two-dimensional projection of interest in parameter space and consider trajectories starting from initial conditions for C1, C2 taken in small neighborhoods of the respective stable fixed points of each cell (see *ThC Network*). In addition to entrainment, we investigate duty cycles. To analyze whether and how top-down drive can cause the escape from its $\beta$ cycle, and hence alter the resulting walking pattern, we also consider two parameter tunings of the CPG: a pacemaker (PM) tuning in which the CPG oscillates in the absence of interneuron input when given sufficient top-down drive and a nonpacemaker (NPM) tuning in which C1 is always quiescent and C2 is always tonically active in the absence of input from the interneurons. The PM tuning is obtained from the NPM by adjusting $\theta_{h_1}$ to introduce a small rightward shift in the $h_1$-nullcline. Entrainment effects with these two tunings share many qualitative similarities, albeit with some quantitative differences, and we will assume the NPM tuning except where otherwise indicated.

To characterize entrainment, we consider nullcline configurations as well as the frequency of the particular walking pattern as top-down $(g_{app_1}, g_{app_2})$ and bottom-up $(g_{syn_{41}}, g_{syn_{32}})$

input strengths are varied. We shall see that the entrainment profile of the CPG will be quantitatively perturbed in the case that either IN4 or IN3 is quasi-entrained rather than entrained; however, the main mechanisms of entrainment breakdown and recovery in the CPG are qualitatively similar across these two cases. Finally, we will consider a measure of robustness of system performance by investigating the possibility of continued entrainment of the CPG in the case that the connection to the CPG from either interneuron has been damaged or destroyed. We find that the CPG is capable of maintaining some form of entrainment for low $\tau$, and while there may be some CPG-specific failure at very low $\tau$, the interneuron subsystem will fail before the CPG, and so these failures are irrelevant to the entrainment of the circuit. Additionally, we find that with sufficient bottom-up signalling to both CPG units, top-down modulation is unnecessary, and hence the CPG system can maintain entrainment without top-down drive.

#### 2.2.3.4  *Numerical Methods*

For IN3 and IN4, we utilized the built-in boundary value solver in Mathematica 11.0, with the initial condition $v_i(0) = 20$ and boundary condition $h_i(0) = h_i(\tau)$, where $t = 0$ corresponds to the beginning of the $\beta$-on part of a cycle; note that any choice of $v_i(0)$ above the right branch of the $v_i$-nullcline would give similar results based on the fast-slow structure of equations (1),(2), and hence the choice of 20 was fairly arbitrary. Those solutions with $h_i(\tau) < h_{lk,i}(1)$ were discarded, as they indicated knee clearance failure and hence were incompatible with entrainment, as discussed above. The remainder were numerically tested for stability, and those that were stable were considered to be entrained.

In the absence of stable entrainment, we considered solutions with initial conditions $(v_i(0), h_i(0)) = (20, h_i^*)$ for various choices of $h_i^*$, over a $2\tau$ time interval. We used a bisection method to seek solutions with $h_i(0) = h_i^* = h_i(2\tau)$ and $h_i(\tau) > h_{lk,i}(1)$, and we called such solutions quasi-entrained; when such solutions were not found, the system was declared to be unentrained (which includes any higher-order quasi-entrainment). We computed the attraction basin of each entrained or quasi-entrained solution as described previously (see *Entrainment of IN4*) by implementing the bisection method numerically.

If IN4 and IN3 are entrained by $\beta$, then for our analysis of the CPG, rather than simulating the full 4-neuron system, we replaced the IN4 and IN3 dynamics with a Heaviside function using a precomputed duty cycle to account for the interneuron inactivation latency. That is, for a given parameter pair $(g_{app_4}, \tau)$, when IN4 is entrained the duty cycle will be slightly different from 3/4-1/4, so we computed the specific duty cycle with this parameter pair and fed this into the Heaviside function, giving the CPG units synaptic input 1 (corresponding to excitation of C1 and inhibition of C2) when IN4 was active and 0 otherwise. We then computed the flow of the CPG equations for each parameter pair with a fixed initial condition, discarded a transient spanning ten time-$\tau$ cycles, and then checked the CPG entrainment conditions – $\tau$-periodicity of the orbit, one active and one inactive phase per period for each CPG unit, and absence of simultaneous C1 and C2 activity – after starting the orbit from its position at the end of the transient.

## 2.3   Results

In this section, we start from baseline parameters that yield entrainment, and we identify major mechanisms of entrainment breakdown and recovery as parameters are varied in the interneuron subsystem and in the CPG subsystem. For the CPG, we focus on the non-pacemaking (NPM) tuning in which the CPG requires rhythmic IN input to oscillate, but most of the mechanisms discussed applied to the pacemaking (PM) tuning as well; see the subsection 2.3.3.2 for a discussion of some exceptions and details. The entrainment breakdowns arise from effects on the nullcline configuration of the system under study that lead either to a change in fixed point properties or to a collision of a trajectory with a nullcline when input level changes. After a breakdown, a rhythm can in some cases be recovered by other parameter variations that also affect nullcline configurations.

Table 1: **Stick Insect Model Parameters** $C_*$ parameters denote capacitances, which differ between interneurons and CPG units, $g_*$ parameters are conductances, and $e_*$ are reversal potentials, with $e_{syn_e}$ and $e_{syn_i}$ the reversals for excitatory and inhibitory synapses, respectively. $\theta_*$ and $\sigma_*$ are half-activation and slope parameters, respectively, for the associated sigmoid functions. $\Gamma$ denotes a phase-shift in the $\beta$ signal, while $\gamma$ represents the activation threshold, controlling the start time and duty-cycle of the ascending drive, respectively. $\varepsilon_*$ give the time constants of the slow variables, which differ for the CPG and IN subsystems. In cases where two values are given, the first corresponds to the NPM tuning and the second to the PM tuning (see text for details). Finally, note that $g_{app_i}$ and $g_{syn_{ji}}$ values (where $j$ denotes the source cell and $i$ corresponds to the cell indicated at the top of the table) are sometimes varied, as indicated in the text.

| | C1 | C2 | IN3 | IN4 | | C1 | C2 | IN3 | IN4 |
|---|---|---|---|---|---|---|---|---|---|
| $g_{cpg}$ (mS/cm$^2$) | 1 | 1 | - | - | $g_{app_i}$ (mS/cm$^2$) | 0.1 | 0.1 | - | 1 |
| $g_{syn_{ji}}$ (mS/cm$^2$) | 0.7 | 0.7 | 1 | - | $C_m$ ($\mu$F/cm$^2$) | 1.1493 | 1.1493 | - | - |
| $C_{m_{in}}$ ($\mu$F/cm$^2$) | - | - | 0.21 | 0.21 | $g_{na}$ (mS/cm$^2$) | 10 | 10 | 10 | 10 |
| $\theta_{Na}$ | -37 | -37 | -37 | -37 | $\sigma_{Na}$ | -6 | -6 | -6 | -6 |
| $g_l$ (mS/cm$^2$) | 2.8 | 2.8 | - | - | $g_{l_{in}}$ (mS/cm$^2$) | - | - | 5.8 | 5.8 |
| $e_l$ (mV) | -65 | -65 | -65 | -65 | $e_{na}$ (mV) | 50 | 50 | 50 | 50 |
| $e_{syn_i}$ (mV) | -80 | -80 | - | - | $e_{syn_e}$ (mV) | 0 | 0 | 0 | 0 |
| $\Gamma$ | - | - | - | $7\pi/4$ | $\gamma$ | - | - | - | $-\sqrt{2}/2$ |
| $\theta_s$ | -43 | -43 | -43 | -43 | $\sigma_{s_i}$ | -0.1 | -0.1 | -0.1 | -2.381 |
| $\theta_\tau$ | -30 | -30 | -30 | -30 | $\sigma_\tau$ | 12 | 12 | 12 | 12 |
| $\theta_{h_i}$(NPM) | -60 | -30 | -58 | -58 | $\theta_{h_i}$(PM) | -55 | -30 | -58 | -58 |
| $\sigma_{h_i}$ | 10 | 6 | 1 | 1 | $\varepsilon$ | 0.0019 | 0.0019 | - | - |
| $\varepsilon_{IN}$(Tetra) | - | - | 0.0008 | 0.0008 | $\varepsilon_{IN}$(Tri) | - | - | 0.0018 | 0.0018 |

### 2.3.1   Interneuron Subsystem

As IN4 is the only cell to receive input directly from the $\beta$ signal, its entrainment depends only on the strength of the $\beta$ signal and the length of the period $\tau$. Our specific results depend on the fact that in the parameter tuning that we use for IN4, which is based on [5, 4, 97], as drive strength increases, the fixed point remains on the left branch of the $v_4$-nullcline, where it is stable, until the nullcline switches from cubic to monotone increasing. Once that occurs, additional increases in drive simply move the stable fixed point to gradually more depolarized voltages, but these remain below the synaptic threshold for the drive levels we consider.

As discussed in section 2.2, in an entrained parameter regime,

$$h_4(\tau) = h_4(0) > h_{lk,4}(1), \tag{3}$$

where $h_{lk,4}(1)$ is defined from the driven $v_4$-nullcline. If drive is weakened via a reduction in $g_{app_4}$, $h_{lk,4}(1)$ increases. If the period $\tau$ of $\beta(t)$ is reduced, the trajectory from a given initial point $(v_4(0), h_4(0))$ ends up with a smaller $h_4(\tau)$. Both of these changes work against condition (3). Correspondingly, we observe that each of these changes can cause a loss of entrainment, with $h_4(\tau) < h_{lk,4}(1)$, such that the solution collides with the left branch of the driven nullcline and IN4 fails to activate when $\beta$ turns on. This failure can result regardless of the stability of the solution $h_4(\tau) = h_4(0)$ for the time$-\tau$ flow map: if the solution is stable, it still lies below the knee, and if the solution is unstable, then any potential $2\tau$-periodic solution will have either $h_4(\tau) < h_{lk,4}(1)$ or $h_4(2\tau) < h_{lk,4}(1)$; see Figure 9 for a display of the highest value of $h_4$ obtained for each of a collection of $(\tau, g_{app_4})$ pairs as well as the respective basins of attraction for the entrained and quasi-entrained solutions.

It is important to note that the duty cycle of IN4 is rarely exactly that of $\beta$. In fact, in most cases, when $\beta$ turns off, the IN4 trajectory collides with the right branch of the undriven $v_4$-nullcline, such that IN4 briefly remains active until $h_4(t) = h_{rk,4}(0)$, causing a slight extension of its active phase relative to the on duration of $\beta$ (e.g., Figure 6E).

As noted previously (see subsection 2.2.3.2), IN3 is functionally identical to IN4. Thus, if IN4 is entrained, either with or without an extended active period relative to $\beta$, then IN3
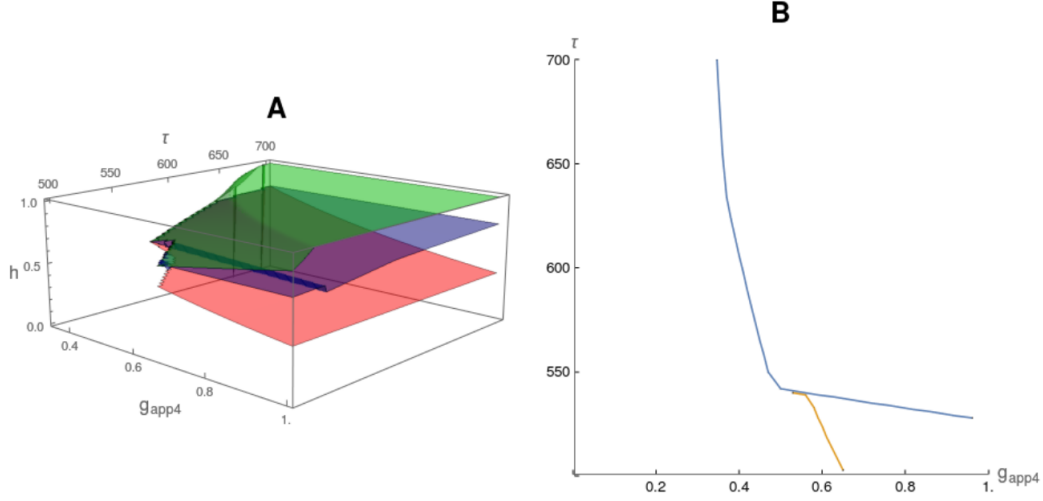
Figure 9: **The entrainment region in $(\tau, g_{app_4})$-space for IN4. A:** The blue surface denotes the highest $h_4$ value of the stable entrained or quasi-entrained orbit over a region of $(\tau, g_{app_4})$ values. The green and red surfaces denote the upper and lower boundary of the orbit's basin of attraction, respectively. **B:** The boundaries of entrainment and quasi-entrainment in $(g_{app_4}, \tau)$ parameter space. The entrained region lies above and to the right of the blue curve and corresponds to the color-coded region in A. The quasi-entrained region lies below the blue curve and to the right of the orange curve.

can undergo the same, left-knee-based failure mechanism as IN4 as the input strength $g_{syn_{43}}$ or $\tau$ is reduced. If IN4 is not entrained, then IN3 does not receive drive during part or all of the time when $\beta$ is active, and hence IN3 will not be entrained either.

### 2.3.2 CPG Subsystem

We recall that in the absence of coupling between C1 and C2 and input from IN3 and IN4, C1 has a critical point on the left branch of the $v_1$-nullcline, at a hyperpolarized voltage corresponding to an inactive state, and C2 has a critical point on the right branch of the $v_2$-nullcline, at a depolarized voltage corresponding to an active state. For an oscillation of the CPG to occur, C1 must activate and then return to inactivity, while C2 must become inactive and then resume its activity. The activation of C1 is induced by the drive from IN4. Once that drive is off, the switch back to C1 inactive and C2 active will be initiated by one of two events: either $v_1$ will fall below the synaptic threshold, *releasing* C2 from inhibition and allowing it to activate, or $v_2$ will *escape*, rising above the synaptic threshold such that C2 inhibits C1 [83, 45, 40]. We analyze these two cases separately and then discuss some additional considerations.

#### 2.3.2.1 *Entrainment involving release by C1: failure and recovery*

First, suppose that in the entrained CPG solution, after IN4 turns off, C1 releases C2 to return the system to its baseline state. Unlike the interneurons, the CPG system can undergo various changes to its fixed point structure as parameters vary. One such change is that an Andronov-Hopf bifurcation may occur in the driven regime for C1, as the drive level coming from either top-down $g_{app_1}$ or bottom-up $g_{syn_{41}}$ is increased. Here, the fixed point where the $v_1$- and $h_1$-nullclines intersect moves from the right driven branch of its cubic $v_1$-nullcline to the middle branch (Figure 10A). In this case, $h_1(t) = h_{rk,1}(1)$ may occur for some $t < \eta\tau$, while $\beta$ is still on (point 2 in Figure 10A), where we recall that we defined $\eta\tau$ as the duration of $\beta(t)$ activation within each cycle. The trajectory for C1 will then jump down to the left branch of the driven $v_1$-nullcline and may cross the synaptic threshold $v_1 = \theta_s$, releasing C2. If this release happens too soon or the inhibition from C1 to C2 is

too weak, however, then C2 will not be able to activate. Now, if the drive to C1 is not too large, the time before $h_1$ reaches $h_{lk,1}(1)$ is longer than the remaining time over which C1 receives bottom-up input. Hence, when that input turns off, C1 returns to the left branch of the $v_1$-nullcline and C2 eventually activates, maintaining entrainment. For even larger drive, C1 will reach the left knee of the driven $v_1$-nullcline, where $h_1 = h_{lk,1}(1)$ (point 3 in Figure 10A), and will re-activate, resulting in two C1 activations during a single $\beta$ cycle of period $\tau$ (Figure 10B), which does not qualify as entrainment.

Given this failure, there are several parameter manipulations that can restore entrainment. First, an increase in the pace of walking, implemented by lowering $\tau$, can recover entrainment, When $\tau$ is lowered, assuming that IN4 remains entrained, the duty cycle of IN4 remains approximately 3/4-1/4, and so when C1 moves to the left branch of the driven $v_1$-nullcline, the remainder of the drive period is short enough that $h_1(\eta\tau) < h_{lk,1}(1)$ when the drive period ends at $t = \eta\tau$, preventing C1 from activating for a second time. C1 still fails to release C2 when it first jumps down from $h_{rk,1}(1)$ (point 2 in Figure 11A), but since there is no simultaneous activity of C1 and C2, the solution still represents entrainment. Although in this case the duty cycle of the CPG can be quite different from that of $\beta$, and we have simultaneous quiescence, each cell undergoes exactly one tonically active and one quiescent phase during each $\tau$ period (Figure 11).

Although this failure can be induced by increasing the drive to C1, it can also be remedied with an additional increase in this drive (either $g_{app_1}$ or $g_{syn_{41}}$). If the drive to C1 is increased enough, the driven $v_1$-nullcline loses its cubic structure and becomes monotone increasing. This approach removes the release mechanism altogether, forcing the CPG oscillation to be entirely dependent on the oscillation of the bottom up signalling, and hence on $\beta$. While sufficient, applying enough drive to ensure monotonicity is not always necessary, as increases in drive also lower the right knee of the driven $v_1$-nullcline, increasing the time before C1 jumps down to its quiescent driven branch (Figure 12).

A third mechanism by which this failure can be remedied is by top-down stimulation of C2. Higher top-down drive onto C2 promotes the activation of C2 when released by C1. Specifically, when C1 leaves the active branch of the driven $v_1$-nullcline, C2 loses a source of inhibition. When the inhibition on C2 from IN3, $g_{syn_{32}}$, is strong relative to its top-down
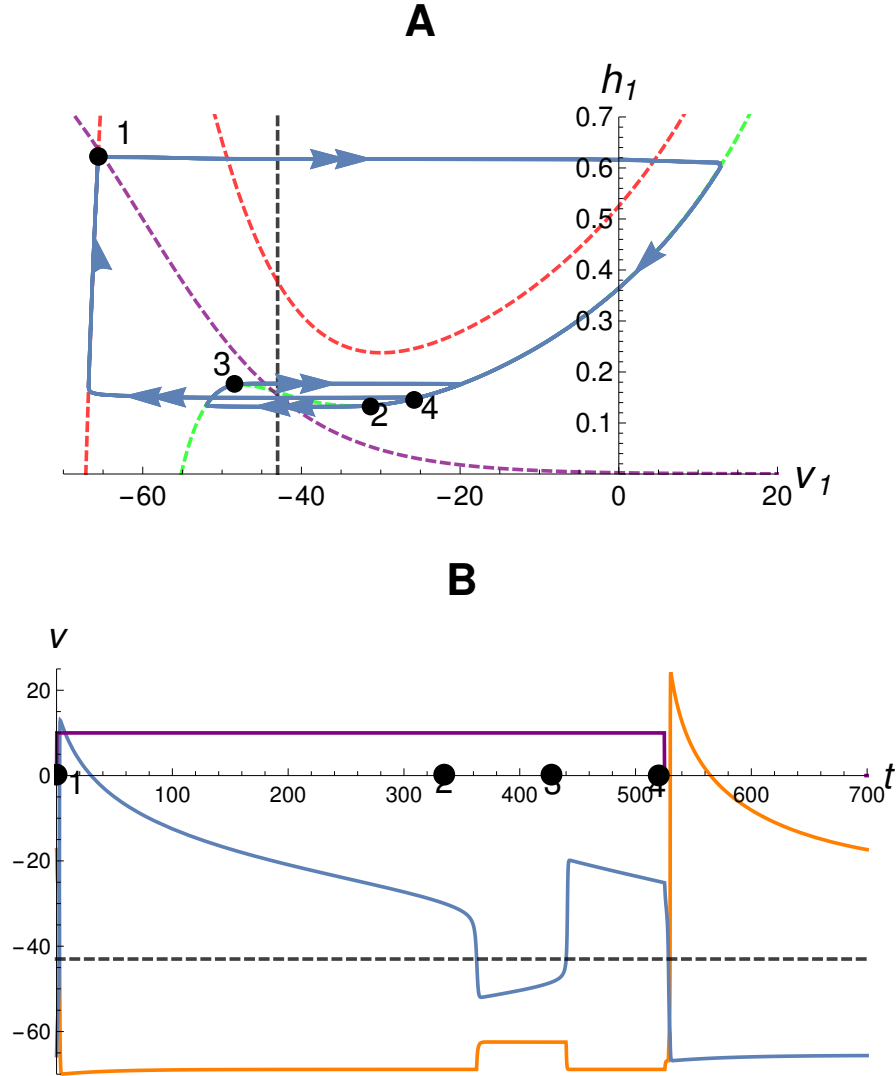
Figure 10: **Entrainment failure after an AH bifurcation in the phase plane of C1, relating to a premature jump-down.** **A:** C1 phase plane. Note that the driven $v_1$-nullcline (green) and $h_1$-nullcline (purple) intersect on the middle branch of the former. At point 1, drive turns on and C1 becomes active. At point 2, $h_1 = h_{rk,1}(1)$ and C1 jumps down. In this simulation, this does not release C2 (not shown), and C1 reactivates at point 3, where $h_1 = h_{lk,1}(1)$. At point 4, drive turns off and C1 returns to the inactive, undriven $v_1$-nullcline (red). The vertical black dashed line indicates the synaptic threshold. B: Time course of $v_1$ and $v_2$ during the failed release ($v_1$ blue, $v_2$ orange). The purple curve indicates the drive from IN4 due to $\beta$, enlarged for visibility, and the dashed black line indicates the synaptic threshold.

32
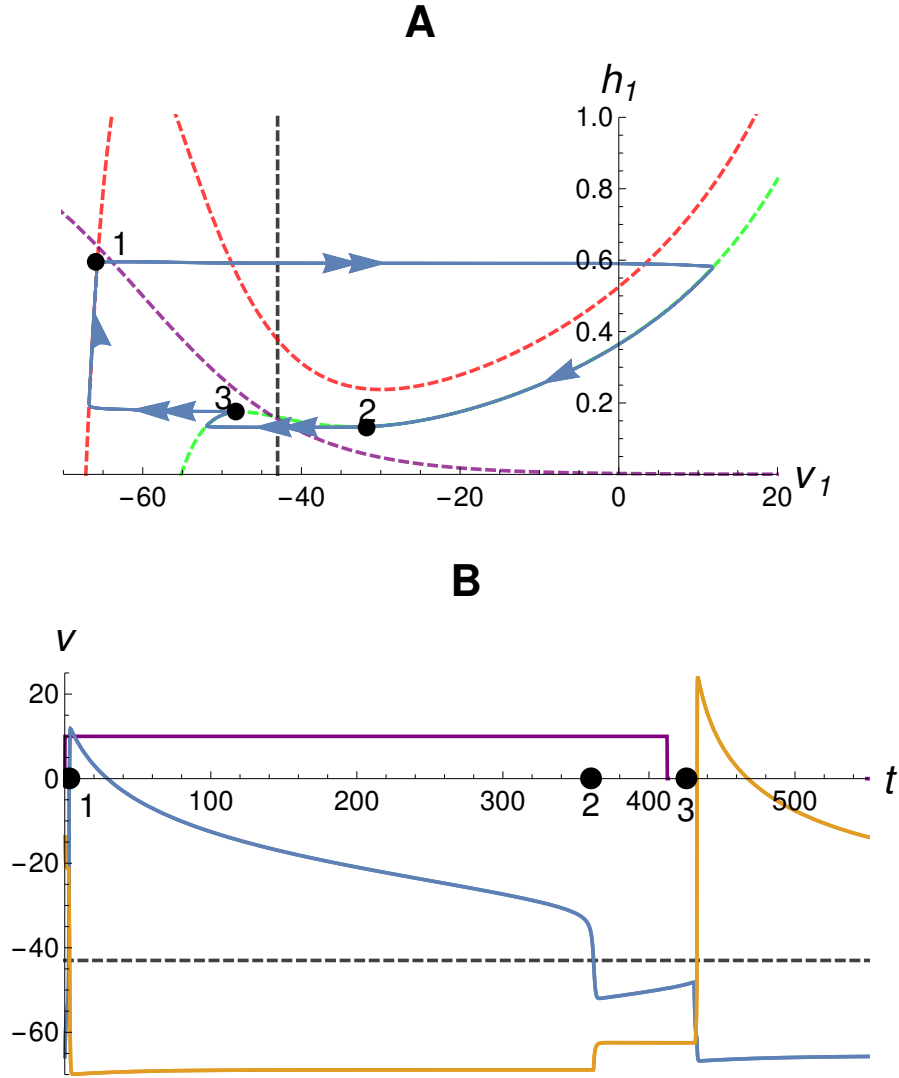
Figure 11: **Recovery of CPG entrainment by decreasing the bottom-up drive period $\tau$. A:** At point 1, drive begins and C1 activates. At point 2, C1 jumps down but C2 fails to activate (not shown). Because of the relatively small value of $\tau$, the drive ends while C1 is at point 3, before it can reactivate, causing C1 to jump down, allowing C2 to jump up, and restoring the entrained rhythm. Note that the nullclines have not changed from Figure 10. **B:** Time course of $v_1$ (blue) and $v_2$ (orange) with reduced $\tau$. Note that while the voltage $v_1$ begins to climb slightly after an initial drop-off around time 350, it remains below synaptic threshold (dashed black).

**A**

**B**
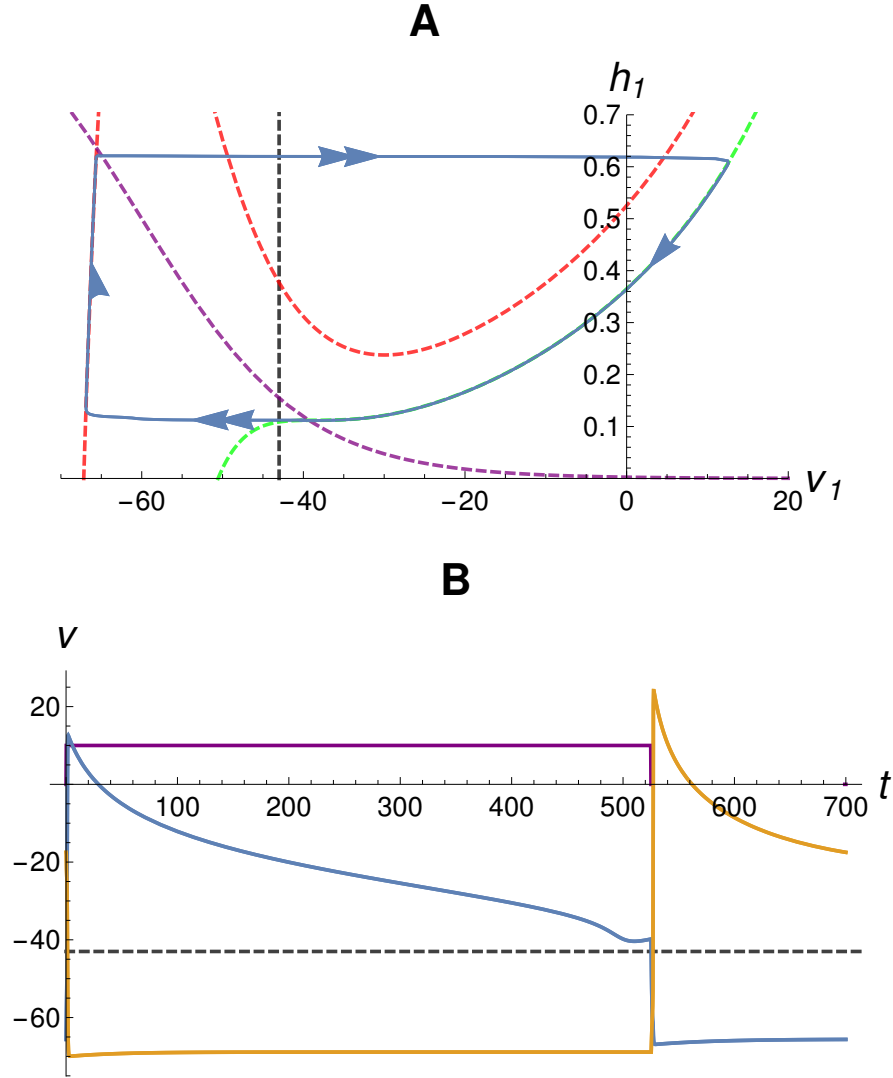
Figure 12: **Recovery of CPG entrainment by increase in drive to C1. A:** Increasing the drive to C1 can restore entrainment by removing the release mechanism. With increased drive, the $v_1$-nullcline becomes monotonic or nearly monotonic; C1 does not jump down below synaptic threshold while $\beta$ is active and hence does not release C2. **B:** Time course of $v_1$ and $v_2$ ($v_1$ blue, $v_2$ orange) for the recovered entrained solution. Note that C1 falls below synaptic threshold only when the drive $\beta$ turns off.

34

drive, $g_{app_2}$, the removal of inhibition from C1 does not change the fixed point structure for C2: it retains a stable quiescent fixed point and fails to activate. With increased $g_{app_2}$, the loss of inhibition from C1 that arises when C1 jumps down to the left branch of the $v_1$-nullcline pushes the C2 system through a fold bifurcation and annihilates the stable quiescent fixed point. With this fixed point destroyed, C2 can jump up to the active state. Once active, C2 inhibits C1, which then moves to an intermediate $v_1$-nullcline of partial drive and partial inhibition. In this case, the middle branch fixed point is destroyed, and C1 now has a stable quiescent fixed point. As before, the duty cycle has changed, but the CPG still meets the requirement of one active and one inactive phase of each unit per $\tau$ period (see Figure 13).

In summary, in this regime, when entrainment is lost, it can be recovered by decreasing $\tau$, increasing drive to C1, or increasing $g_{app_2}$, the top-down drive to C2. Interestingly, these recovery mechanisms lead to different CPG output patterns and duty cycles.

**2.3.2.2** *Entrainment involving escape by C2: failure and recovery*

We now change gears and turn our attention to entrained solutions for which, after IN4 and IN3 turn off, C2 becomes active by escape, without a termination of the inhibition from C1. This escape regime requires a sufficiently strong $g_{app_2}$; how strong is sufficient in turn depends on the inhibition strengths $g_{syn_{12}}, g_{syn_{32}}$. That is, as the top-down drive $g_{app_2}$ to C2 is increased in the presence of full inhibition by C1 and IN3, the C2 subsystem will undergo a fold bifurcation (cf. Figure 13), although the stronger $g_{syn_{12}}, g_{syn_{32}}$ are, the larger $g_{app_2}$ must be to make this happen. In this case, with a large enough period $\tau$, C2 can return to its tonically active phase via an escape mechanism, where $h_2(t) = h_{lk,2}(1)$ for some $t < \eta\tau$. When this occurs, C2 inhibits C1 and the trajectory jumps to an intermediate $v_1$-nullcline in the $(v_1, h_1)$ plane that reflects the presence of this inhibition before the end of the $\beta$ drive signal. Entrainment success or failure then depends on drive to C1. If C1 has evolved to satsify $h_1(t) < h_{rk,1}^{inh}(1)$, where the superscript *inh* represents the fact that C1 receives inhibitory input from C2, then its trajectory jumps to the silent phase and an entrained solution results. If, however, $g_{app_2}$ is too strong, then C2 escapes too soon, with $h_1(t) > h_{rk,1}^{inh}(1)$. In this case, when C2 escapes, the C1 trajectory collides with the active
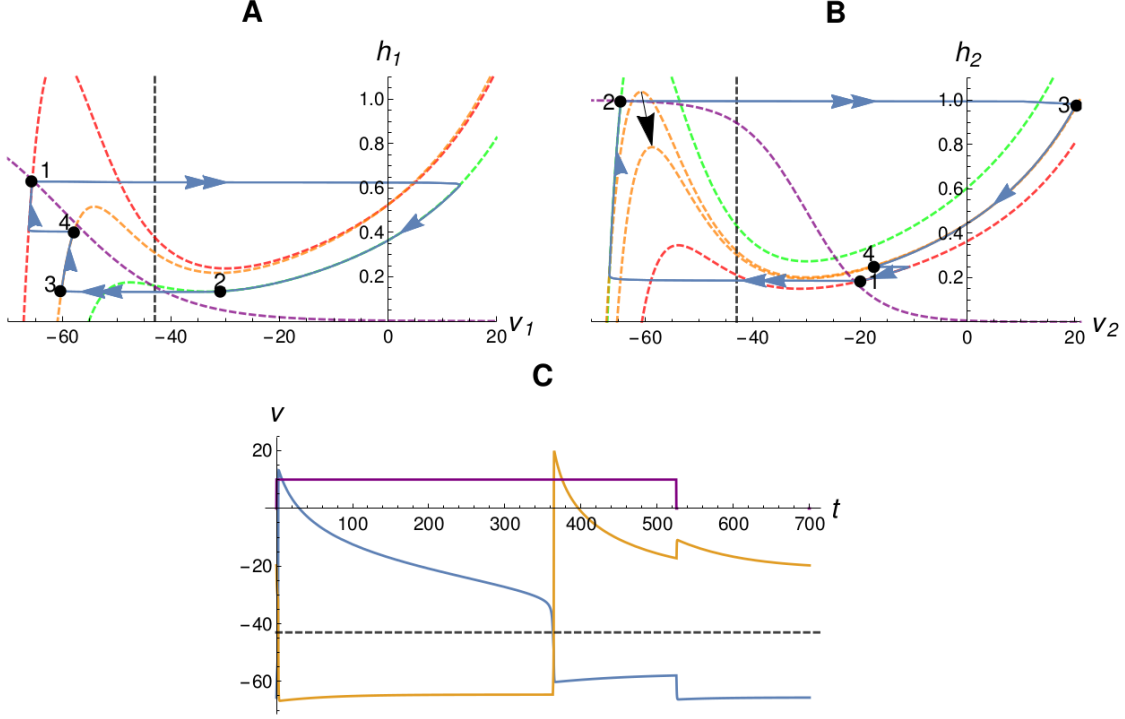
Figure 13: **Recovery of CPG entrainment by increased top-down drive to C2. A-B:** Phase plane view of a stable entrained orbit for C1 (A) and C2 (B). Increasing top-down drive to C2 can restore entrainment via a fold bifurcation in the C2 system. At point 1, drive begins, activating C1 and inactivating C2. At point 2, C1 successfully releases C2 due to a fold bifurcation in the fixed point structure of C2 as the $v_2$-nullcline moves from the green to the lower orange position (instead of the upper orange position that occurred for smaller $g_{app_2}$). From point 3, both cells travel along their intermediate nullclines (with input from IN4 and IN3 still on) until point 4, when the drive from the interneurons ends. The phase plane for C1 has not changed relative to Figure 10. For C2, the green dashed $v_2$-nullcline arises due to inhibition from C1 and IN3, while the red dashed $v_2$-nullcline corresponds to the absence of inhibition. The two dashed orange $v_2$-nullclines occur for a partially inhibited state, after C1 has become quiescent but IN3 is still active, for two different levels of $g_{app_2}$. As top-down drive to C2 is increased, the orange knee moves below the $h_2$-nullcline. **C:** A voltage trace of the successfully entrained solution. The blue curve is $v_1$, the orange $v_2$. Note that although the duty cycle is approximately 1/2-1/2, entrainment conditions are satisfied.

36

branch of the inhibited $v_1$-nullcline and the CPG enters a period of simultaneous activity of C1 and C2. This appears to be the only mechanism by which failure occurs due to simultaneous activity (see Figure 14).

Decreasing $\tau$ allows C2 to remain quiescent for a larger proportion of the active $\beta$ cycle, reducing the time of co-activation of C1 and C2. For $\tau$ low enough, the time required for C2 to achieve $h_2 = h_{lk,2}(1)$ and escape becomes longer than the extent of the active phase of the $\beta$ cycle, which restores entrainment, since there is no longer an escape of C2 with C1 active (see Figure 15).

This failure can also be remedied by weakening $g_{app_1}$ or $g_{syn_{41}}$. As drive to C1 is weakened, the right knee of the intermediate $v_1$-nullcline moves up, until at the moment of C2 escape, C1 lies below the knee and can hence jump directly to the left branch of the $v_1$-nullcline. Now, since C1 is quiescent for the remainder of the $\beta$ cycle, we have no simultaneous activity and have one active and one inactive phase per cycle for each cell, and thus the requirements for entrainment have been restored (see Figure 16). Interestingly, in the solution with entrainment restored by this mechanism, C1 and C2 have almost fully swapped their duty cycles relative to the original entrained solution, with C2 on and C1 off for about 3/4 of each period.

More generally, the effects of this mechanism on the duty cycle can be quite extreme, with only small changes in $g_{app_2}$ leading to large changes in the duty cycle and, as we have just observed, with some cases of the duty cycle being completely reversed. The latter regime could possibly relate to backward stepping, which has been found to feature such a reversal in protractor and retractor motor neuron activation and in the synaptic drive to these neurons [27, 13], an idea which may warrant further investigation in future work. This parameter variation mechanism therefore shows some promise as a means by which top-down signalling can override the maintenance of walking patterns by bottom-up sensory signals and ease transitions to different walking pattern modalities (see Figure 17).

In summary, with relatively large $g_{app_2}$ that gives rise to C2 escape, failure can occur when $g_{app_2}$ becomes too strong relative to the inhibitory signal strength $g_{syn_{32}}$. In some cases, decreasing drive to C1, via $g_{app_1}$ or $g_{syn_{41}}$ can restore entrainment by preventing co-activation of C1 and C2, but at the cost of a major difference in duty cycle between the CPG
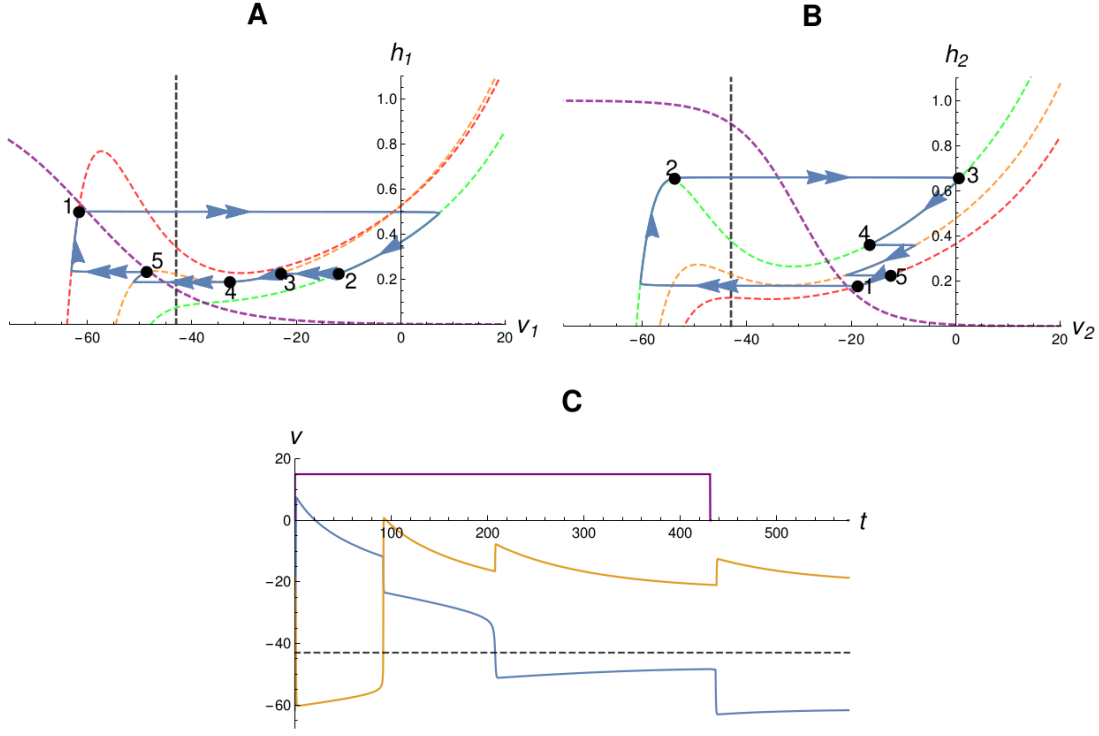
Figure 14: **Entrainment failure when C2 escapes and C1 remains active. A-B:**
Phase plane views for C1 (A) and C2 (B) show projections of a trajectory representing failed
entrainment. At point 1, drive and inhibition due to $\beta$ are applied to C1 and C2 from
IN4 and IN3, respectively. At point 2, C2 escapes, and it returns to the active phase at
point 3; meanwhile, although C1 is inhibited by C2, it becomes caught on the active branch
of the intermediate $v_1$-nullcline (orange). From point 3 to point 4, C1 and C2 are both
active. At point 4, C1 returns to quiescence, causing C2 to move up to the intermediate
$v_2$-nullcline. Finally, at point 5, the signal due to $\beta$ ends and both CPG units jump to
corresponding voltage nullclines, where they evolve back to position 1. **C:** A voltage trace
of the unentrained solution shown in (A-B). Blue shows $v_1$ and orange $v_2$. Note that there
is an extended period of time when both cells are active together.
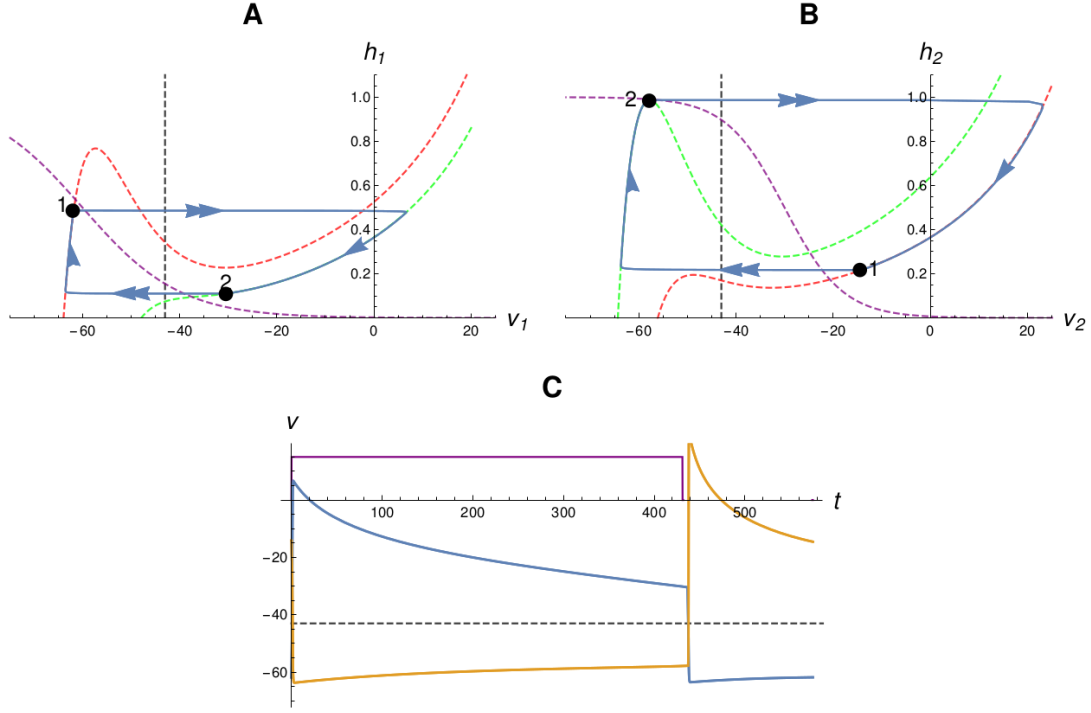
Figure 15: **Recovery of CPG entrainment with C2 escape by decreasing $\tau$. A-B:** Phase planes for C1 (A) and C2 (B). With small enough $g_{app_2}$ and a fast pace (small $\tau$), C2 fails to escape before the end of the active phase of the $\beta$ drive, restoring entrainment. C1 and C2 are at point 1 when $\beta$ activates. With low enough $\tau$ or top-down drive to C2, cells C1 and C2 reach point 2 when $\beta$ turns off, without an escape of C2, and entrainment is restored. **C:** A voltage trace of the resulting entrained solution ($v_1$ blue, $v_2$ orange). Note that although C2 is capable of escape if the period $\tau$ were long enough, this does not occur for this parameter set.
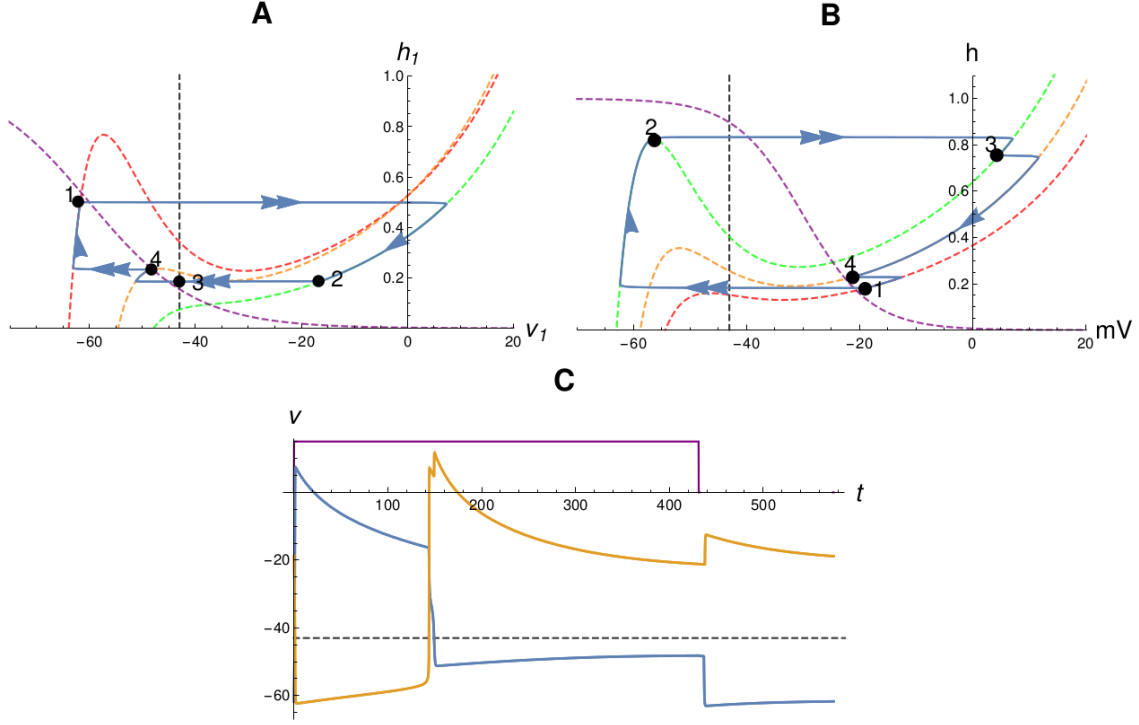
Figure 16: **Recovery of CPG entrainment with C2 escape by decreasing drive to C1.**
**A-B**: Phase planes for C1 (A) and C2 (B) showing the restored entrainment. At point 1, $\beta$ activation begins. Later, at point 2, C2 escapes. When this happens, $h_1$ lies below the right knee of the relevant $v_1$-nullcline and hence C1 returns to quiescence, briefly continuing to provide inhibition to C2 until point 3, when $v_1$ falls below $\theta_{syn}$. At point 4, $\beta$ activation ends, allowing each cell to jump to its corresponding $\beta$-off nullcline. **C:** A voltage trace ($v_1$ blue, $v_2$ orange) of one cycle of the entrained trajectory shown in (A-B). Notice that the duty cycles have been nearly completely reversed compared to the original CPG rhythm.

40

and $\beta$. Decreasing $\tau$, on the other hand, gives a recovery without this change in pattern.

### 2.3.2.3 *Overdriven C1*

C1 may receive enough top-down drive to cause a timing-dependent $2\tau$-periodic failure. In this case, as the $\beta$ cycle ends, say at time $t_{off} = \eta\tau \mod \tau$, drive to C1 ends. At that moment, C1 is neither being driven by IN4 nor inhibited by C2. When $g_{app_1}$ is large, the resulting $v_1$-nullcline is monotonic; we have seen how this monotonicity can be useful for entrainment in subsection 2.3.2.1. But if $g_{app_1}$ is so large that $v_1(t_{off}) > \theta_{syn}$, then C1 remains active when $\beta$ turns off. With C1 active, C2 is prevented from activating and $\tau$-periodic entrainment is lost (see Figure 18).

Interestingly, this behavior is made worse by weakening bottom-up drive, $g_{syn_{41}}$, to C1. As $g_{syn_{41}}$ is decreased, the active phase fixed point for C1 is pushed to larger $h_1$ and smaller $v_1$. When $\beta$ turns off, the trajectory in the $(v_1, h_1)$ phase plane jumps to a nullcline on which $v_1$ increases with $h_1$. Eventually, the $h_1$ coordinate of the fixed point becomes large enough that when $\beta$ turns off and the trajectory jumps, $v_1 > \theta_s$, preventing the release of C2 from inhibition from C1, and thus C1 remains active on every second $\tau$-period. Correspondingly, we obtain the counter-intuitive seeming result that in the face of excessive top-down drive $g_{app_1}$ to C1, increasing $g_{syn_{41}}$ can restore entrainment (see Figure 19). With this added bottom-up drive to C1, the active fixed point is pushed to larger $v_1$ and smaller $h_1$. Furthermore, at larger $v_1$, the $h_\infty$ function takes on more extreme values, causing the trajectory to travel down the $v_1$-nullcline slightly faster, which allows $h_1$ to reach smaller values. As the value of $h_1$ is lowered, the corresponding $v_1$ value on the $\beta$-off $v_1$-nullcline falls below synaptic threshold, ending inhibition from C1 to C2 and allowing the entrained rhythm to proceed.

As in the C1 release case, the loss of entrainment due to excessive $g_{app_1}$ can also be remedied by increasing $g_{app_2}$ (see Figure 13). Again, as C1 becomes and remains active, C2 quickly approaches a stable quiescent fixed point. With increased $g_{app_2}$, this fixed point undergoes the same fold bifurcation that came into play previously, enabling C2 to escape and return to the active phase when inhibition from IN3 to C2 turns off (Figure 20).
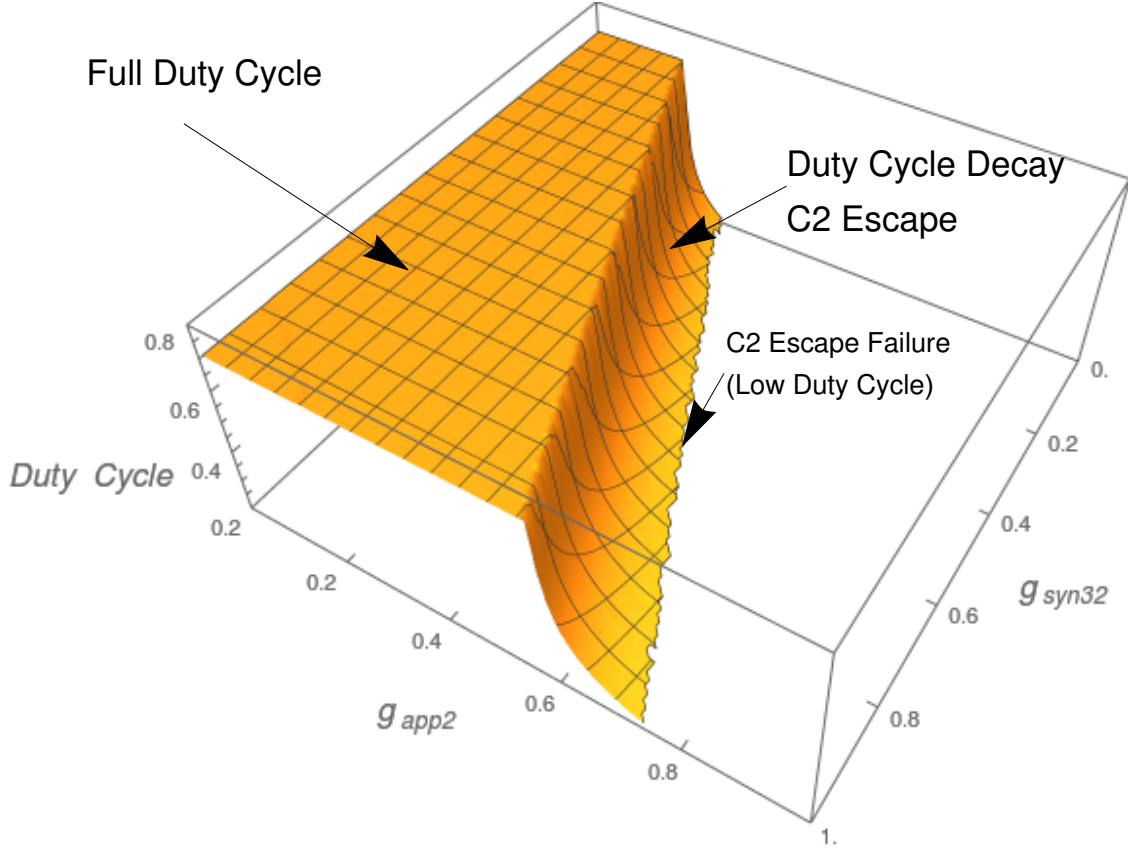
Figure 17: **Entrainment featuring escape by C2 allows for a broad range of duty cycles in the CPG.** The orange surface indicates the duty cycle of the CPG over a range of $(g_{syn_{32}}, g_{app_2})$, with C1 in a baseline tuning. The flat section at a duty cycle of 0.75 represents a regime in which the CPG follows the duty cycle of $\beta$ well; the 0.75 refers to the fraction of each cycle for which C1 is active. From there, sufficient increases in $g_{app_2}$ and decreases in $g_{syn_{32}}$ can lead to the reduction in the fraction of each cycle with C1 active, down to about 0.2 before entrainment is lost.
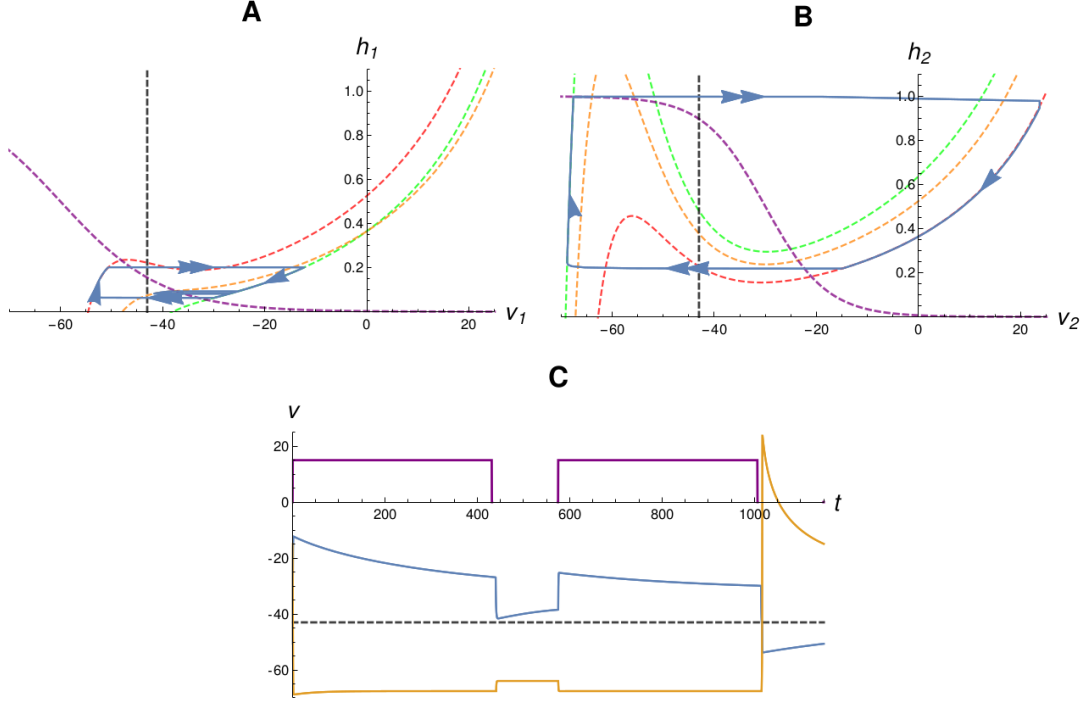
Figure 18: **Bottom-up and top-down signalling to C1 can combine to prevent C1 inactivation on every second cycle. A-B:** Phase planes for C1 (A) and C2 (B). In A, the orange $v_1$-nullcline occurs when C1 is receiving no input, since the $\beta$-dependent drive has ended and $v_2 < \theta_{syn}$. On one of every two cycles, $v_1$ remains above synaptic threshold on the orange $v_1$-nullcline, preventing C2 activation, and entrainment fails. **C:** Time courses of $v_1$ (blue) and $v_2$ (orange) in the case shown in A-B. Note that $v_1$ falls to just above the synaptic threshold (dashed black line) when $\beta$ (purple) turns off.
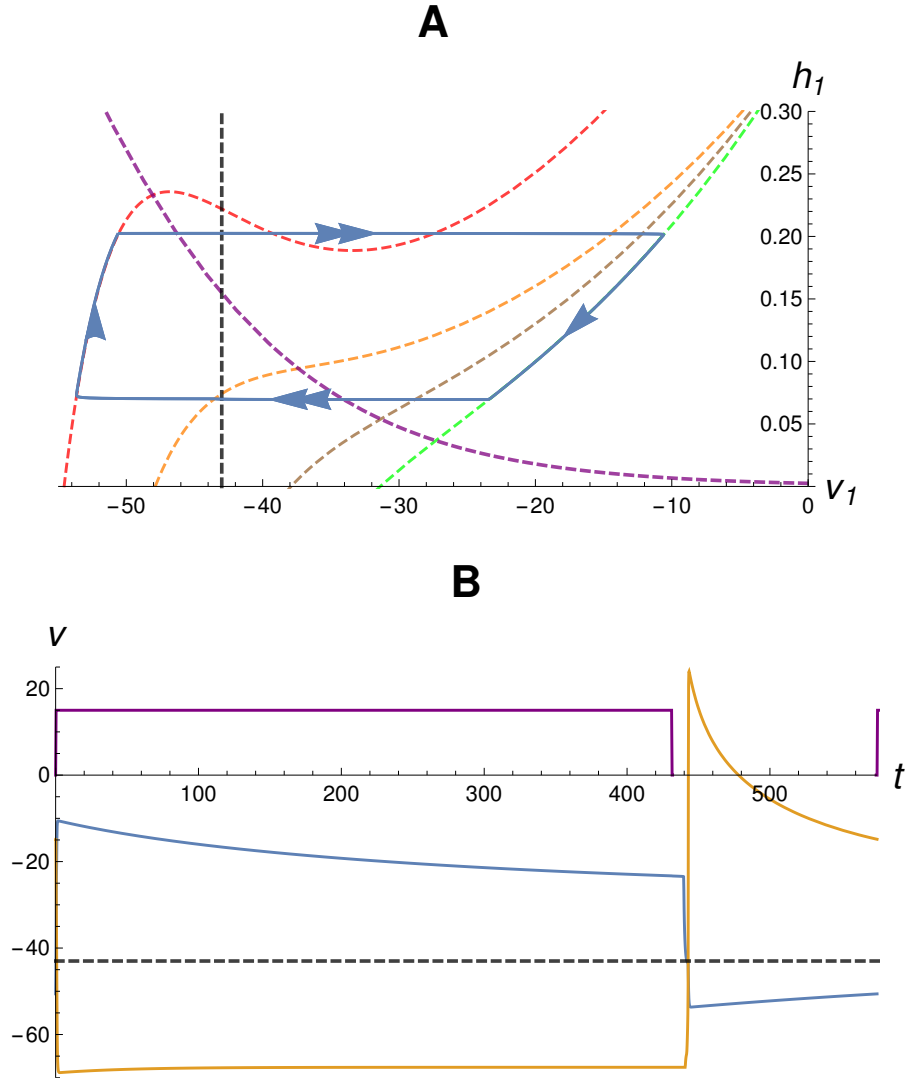
Figure 19: **Paradoxical restoration of entrainment by increase in ascending drive to C1 when $g_{app_1}$ is strong. A:** C1 phase plane. The brown and green dashed curves are the driven $v_1$-nullclines for small and large $g_{syn_{41}}$, respectively. When $g_{syn_{41}}$ is sufficiently large, the trajectory (blue) reaches small enough $h_1$ values by the time that $\beta$ turns off that when it jumps down, it reaches $v_1 < \theta_s$ on the corresponding $v_1$-nullcline (orange), releasing C2. Note here that the scale of $h_1$ has been shortened relative to other phase plane plots to provide a zoomed view of the key region. **B:** Time courses of $v_1$ (blue) and $v_2$ (orange). Again note that C1 now falls below threshold at the end of the $\beta$ activation period.
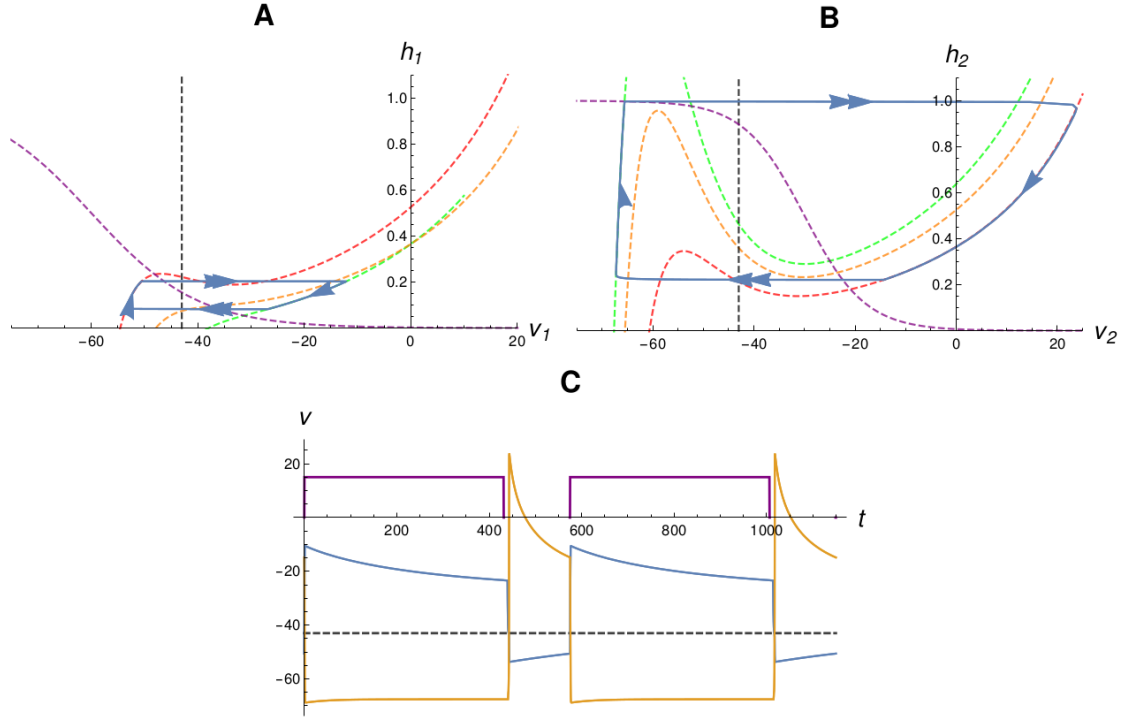
Figure 20: **Recovery of entrainment in the overdriven C1 case by increase in $g_{app_2}$.** Phase planes for C1 **(A)** and C2 **(B)**. As in the C1 release case, increasing drive to C2 can move its intermediate nullcline (orange) through a fold bifurcation. Now, when C1 $\beta$ activation ends, C2 is free to return to its active state, inactivating C1. C: Time courses of $v_1$ (blue) and $v_2$ (orange).

45

**2.3.2.4** *Summary of basic mechanisms*

Let us assume that the $\beta$ period $\tau$ is large enough to yield entrainment of IN4 and IN3, and the drive to C1 is large enough to allow it to be recruited. Surveying the analysis so far, we observe that CPG entrainment involves the recruitment of C1 by $\beta$ followed by a switch from C1 active to C2 active either due to release of C2 by C1, for relatively small $g_{app_2}$, or the escape of C2, for relatively large $g_{app_2}$. In both cases, entrainment to an input signal with a fixed duty cycle can be lost if $\tau$ becomes too large, corresponding to a walking pattern that is too slow for that input, or if $g_{app_1}$ or $g_{app_2}$ is chosen to lie at a problematic level. Interestingly, we see non-monotonicity in the effects of these top-down drive parameters; there are cases when one or both could be increased to restore entrainment, cases when one or both could be decreased to restore entrainment, and intermediate cases where changes in both directions can restore entrainment, although as our figures show, the details of the entrained rhythm do vary across entrained parameter regimes. Thus, the top-down drives in the CPG system offer a powerful control system, and tuning of top-down drives in parallel with modulation of bottom-up input strengths [61, 62] would allow entrainment to occur over the broadest possible range of walking paces.

### 2.3.3 Generalizations

We have considered entrainment to the tetrapodal drive signal when the CPG system is in a non-pacemaking (NPM) mode and hence does not oscillate in the absence of this bottom-up signal. We now go on to consider three scenarios beyond this baseline regime, namely scenarios with certain signaling pathways removed, with the CPG in the pacemaking (PM) mode, or with a tripodal drive signal.

**2.3.3.1** *Loss or removal of signaling pathways from interneurons*

The exact wiring of the network displayed in Figure 5, particularly for the interneuron subsystem that conveys the sensory information to the CPG, is not known. The wiring diagram shown is based on experimental data and reasonable neurophysiological assumptions

made for the stick insect walking system as well as on numerical simulations made with constructed models [126, 129, 128]. However, the suggested network was never analyzed with respect to redundancy in the way that sensory information is transmitted to the CPG.

Interestingly, we found that under some conditions, the CPG can maintain entrainment even when some synaptic connections associated with the interneuron subsystem are removed, suggesting that the system does feature some redundancy. We next consider how this effect can occur.

We require that IN4 is not eliminated entirely, as it is the only cell receiving the $\beta$ signal. If the synapse projecting from IN4 to either C1 or IN3 is eliminated ($g_{syn_{41}} = 0$ or $g_{syn_{43}} = 0$, respectively), however, then the CPG can still maintain entrained oscillations over a certain parameter regime. That is, oscillating drive from IN4 to C1 alone is capable of maintaining entrainment, as is oscillating inhibition from IN3 to C2.

Consider first what happens if $g_{syn_{41}} = 0$. In this case, first suppose that $g_{app_1}$ is small but C1 is still able to activate when C2 becomes inhibited by IN3. The resulting CPG duty cycle fails to exceed 1/2-1/2 because C1 jumps down from the active phase and releases C2 to activate before the end of $\beta$. Figure 21 shows the duty cycle of the CPG in the case of $g_{syn_{41}} = 0$, with a low, fixed $g_{app_1}$. The nonmonotonicity of the boundary at low $g_{app_2}$ is due to the following: Starting on the plateau, with $g_{syn_{32}} \approx 0.6$, the CPG is entrained due to the release mechanism discussed in section 2.3.2.1. As $g_{app_2}$ is lowered, we find a new, timing-dependent entrainment failure mechanism. In this failure mode, C2 is not driven sufficiently to allow for escape; thus, the activation of C2 depends on the loss of inhibition from $\beta$ (via IN3) and the activation of C1 requires the inactivation of C2 due to the onset of inhibition to C2 from $\beta$. In this regime, however, the intermediate $v_2$-nullcline of C2 corresponding to the presence of inhibition from IN3 but not C1 has its right knee above synaptic threshold. With small enough $\tau$, if C2 begins its active phase at $t_0 = 0$, then at $t_1 = \tau/4$, $h_2(t_1) > h_{rk,2}(0)$, the intermediate right knee, and so when $\beta$ turns off, the trajectory collides with the active branch of this intermediate nullcline and C2 remains active, while C1 remains inactive due to the persistence of inhibition from C2 (see Figures 22, 23).

As $g_{app_2}$ is increased, C2 may escape before C1 releases, allowing the escape-dependent mechanism to dominate and providing another window of entrainment, before it is again lost

due to early escape, as in *Entrainment involving escape by C2: failure and recovery.* The boundary between the flat portion of the surface and the curved portion arises where the times associated with the escape and release mechanisms exactly balance, so that the two events occur simultaneously.

Next, consider what happens as $g_{app_1}$ is increased with $g_{syn_{41}} = 0$. With sufficiently large top-down input to C1 and moderate top-down input to C2, the CPG can recover its 3/4-1/4 duty cycle, even though $g_{syn_{41}} = 0$. With enough top-down drive to C1, the active $v_1$-nullcline of C1 becomes monotonic, preventing early release, and the inactive $v_1$-nullcline maintains its quiescent fixed point; thus, in the resulting oscillation, transitions occur through the actions of $\beta$ on C2.

The other reduced signaling scenario to consider is $g_{syn_{43}} = 0$. Under this condition, C2 no longer receives input from IN3 since IN3 no longer activates and hence the inactivation of C2 is entirely reliant on inhibition from C1. First, C1 needs to activate; it can do so when it receives excitation from IN4, but only if $g_{app_1}$ is not too small relative to the strength of the inhibition from C2 to C1. A danger here is that if the inhibition from C1 to C2 is too weak, or $g_{app_2}$ is too strong, then entrainment can fail due to co-activation of C1 and C2. A second pitfall for small $g_{app_1}$, even if C2 does inactivate, is that C1 will be in the release mode and will leave the active phase before the end of $\beta$. Thus, although entrainment occurs, the CPG again fails to maintain the duty cycle of its input. Increasing $g_{app_1}$ can help to increase the duty cycle as it did with $g_{syn_{41}} = 0$. Thus, we see that by top-down control - specifically, tuning up $g_{app_1}$ and tuning down $g_{app_2}$ - the CPG can maintain function despite loss of inhibition from IN3 to C2.

In summary, the wiring diagram shown in Figure 5 appears to include some redundancy, in that the ascending $\beta$ signal is transmitted to the CPG via two pathways, namely IN4-to-C1 and IN4-to-IN3-to-C2, rather than just to one. Our analysis shows that the dual pathway system is not necessary for entrainment of the CPG to the $\beta$ signal. Without both pathways, however, the maintenance of the duty cycle of the tetrapodal walking pattern by the CPG becomes more difficult and requires quite strong top-down input to C1.
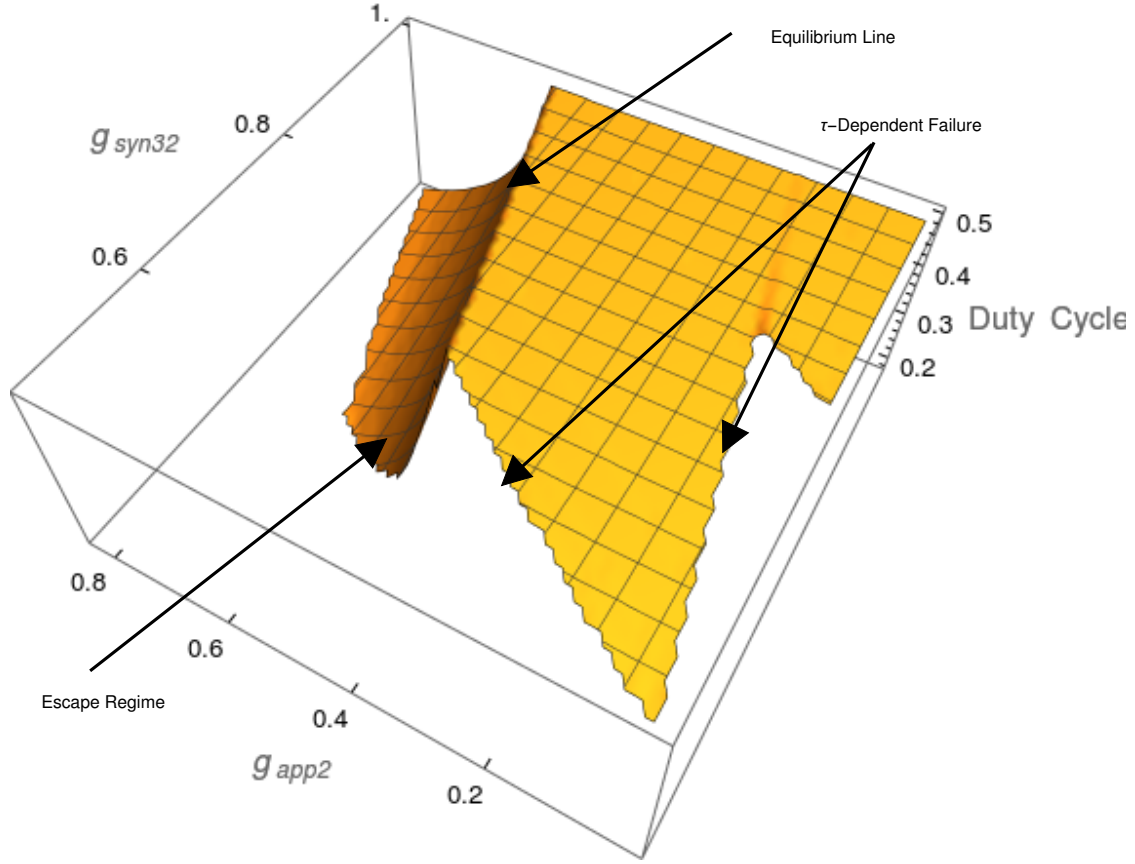
Figure 21: **With loss of part of the ascending signaling pathway and low top-down drive to C1, entrainment is possible but imprecise.** The duty cycle of the CPG with the IN4-C1 connection removed and with fixed, small $g_{app_1}$ stays constant over a range of $g_{app_2}$ and $g_{syn_{32}}$ but decays as these parameters are increased and decreased, respectively. Observe that the fraction of the cycle for which C1 is on (duty cycle) is bounded above by 0.5. Entrainment can also be lost in a region of parameter space (white triangle to the right of the surface).
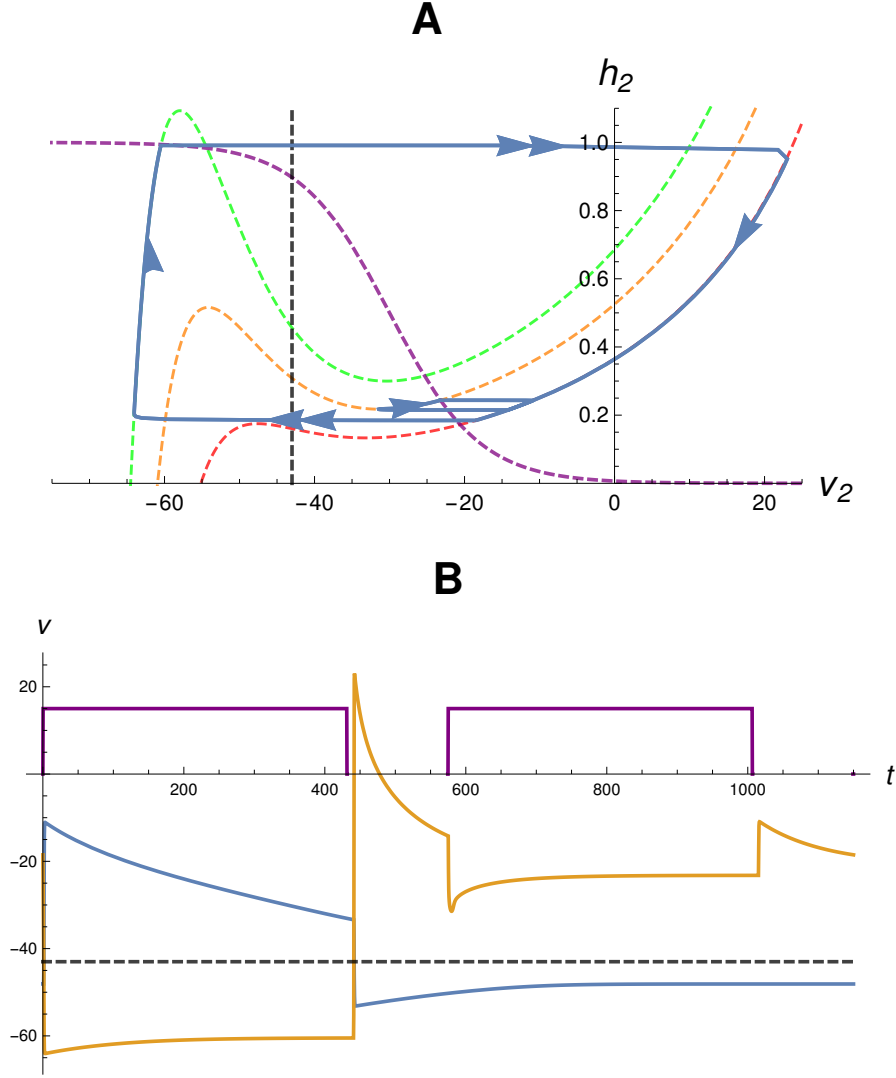
Figure 22: $\tau$-**dependent failures can occur for** $g_{syn_{41}} = 0$. **A:** Phase plane for C2 showing entrainment failure for moderate $g_{app_2}$. When inhibition to C2 begins, C2 may be caught on an intermediate $v_2$-nullcline (orange) without inhibition from C1. Since C1 receives no drive from IN4, it remains inactive, preventing entrainment. On the subsequent cycle, C2 does not become caught and C1 can activate, and these cases alternate repeatedly. **B:** The C1 (blue) and C2 (orange) voltage traces. Note that at the second onset of $\beta$-induced inhibition to C2, $v_2$ decreases but remains above threshold, preventing the activation of C1.
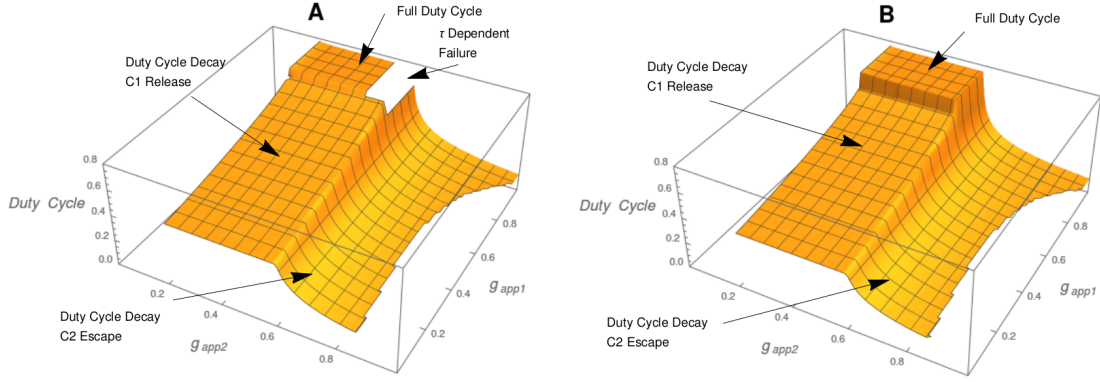
Figure 23: **Top-down drive can restore the tetrapodal duty cycle in the absence of drive from IN4 to C1.** The duty cycle of the entrained orbits with fixed bottom-up inhibition to C2, $g_{syn_{32}}$. **A:** With lower $\tau$, there is a failure to entrain for moderate $g_{app_2}$ and large $g_{app_1}$, similar to the $\tau$-dependent failure mechanism described above. **B:** With higher $\tau$, entrainment in this parameter region is recovered. In both cases, we observe that the duty-cycle can increase up to a plateau at 3/4-1/4 as $g_{app_1}$ increases, for small $g_{app_2}$. The mechanism governing the duty cycle here is the release from C1, discussed in section 2.3.2.1. As we increase $g_{app_2}$, we see a sharp drop in the duty cycle, which is again governed by the escape of C2, discussed in section 2.3.2.2. On the plateau itself, neither cell is escaping nor releasing, and so the duty-cycle is that of $\beta$, governed entirely by bottom-up input to C2.

**2.3.3.2** *Differences between PM and NPM CPGs*

With a small rightward shift in the $v_1$ nullcline and a sufficiently large value of $g_{app_1}$, the CPG subsystem will oscillate even without bottom-up signaling, becoming what we are calling a pacemaker (PM). In this tuning, the range of entrainment expands to include very small values of $g_{syn_{41}}$, allowing robust entrainment even with an almost complete loss of the connection between the interneuron subsystem and C1. If there is a complete loss of signal, however, then the period of the CPG oscillation will not match that of $\beta$, and so entrainment is lost. This is a result of the destabilization of the resting fixed point of C1 in the undriven state. Since it is no longer stable, the $h_1$ value of the trajectory is now free to climb above the slightly driven left knee, and so in turn the voltage is clear to jump to the active branch once even slight $\beta$ drive from IN4 to C1 begins. Indeed, since the slightly driven nullcline is itself in an intrinsically oscillating regime, this return to activation is guaranteed. C2 retains its active stable fixed point, both when C1 is active and quiescent, but the fixed point corresponding to C1 quiescent lies above the right knee corresponding to C1 active. Thus, the activation of C1 causes C2 to jump down to its quiescent state, where it approaches a stable quiescent fixed point until C1 returns to quiescence.

The difficulty with entrainment in the PM regime is that in cases of higher $g_{syn_{41}}$, C1 enters its overdriven state more readily than in the earlier NPM case, since now the driven fixed point for C1 occurs at larger $v_1$ and $h_1$. When $v_1 > \theta_s$ on the intermediate $v_1$-nullcline that becomes relevant when $\beta$ turns off, the release of C2 is prevented. Therefore, in the PM regime, top-down signaling becomes a less effective mechanism for decoupling the limb segment movements from bottom-up sensory signaling than in the NPM regime (see Figure 24).

**2.3.3.3** *Unlike the tetrapodal case, tripodal walking can lose entrainment via drift in duty cycle but does not exhibit quasi-entrainment*

To retune the system to a tripodal walking pattern, we require that the interneuron subsystem entrains to a $\beta$ rhythm with duty cycle 1/2-1/2 instead of 3/4-1/4. To achieve this change, we set both $\Gamma$ and $\gamma$ to 0, which adjusts the phase-shift and the activation
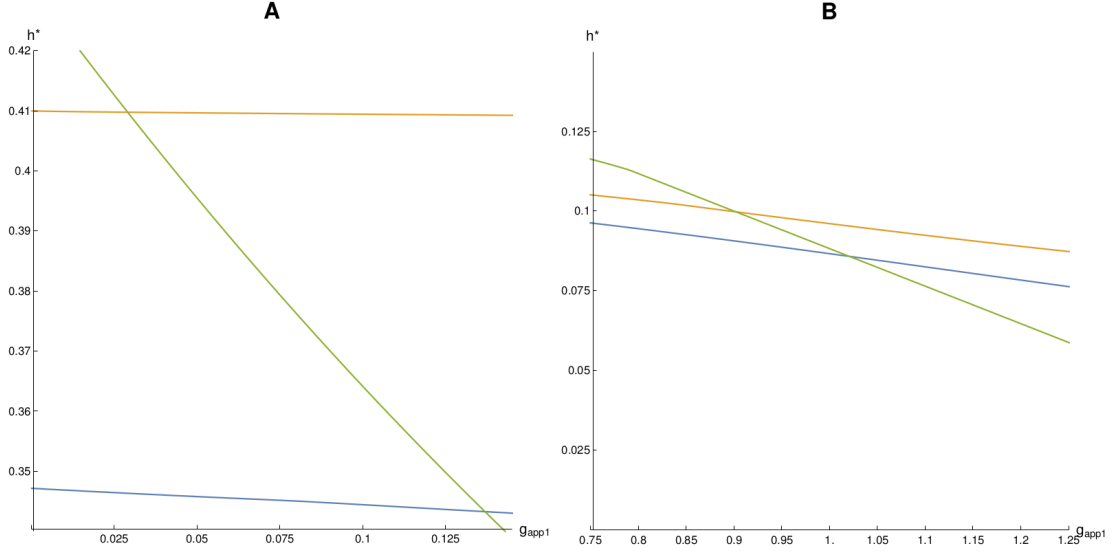
Figure 24: **CPG entrainment in the PM and NPM parameter regimes.** In each panel, we track the position of the value of $h_1$ as $\beta$ turns on **(A)** or off **(B)**. In (A), the trajectory in the PM case (orange) reaches above the left knee (green) at a smaller value of $g_{app_1}$ than is needed for the NPM case (blue), facilitating entrainment. Likewise, in (B), as $g_{app_1}$ is increased, the trajectory in the PM case (orange) when $\beta$ turns off ends up above the right knee (green) at lower $g_{app_1}$ than for the NPM case (blue), such that the overdriven state occurs more easily in the PM case.

threshold of $\beta$, respectively. We also increase the rate constant $\varepsilon_i$ of the interneuron slow variables $h_i (i = 3, 4)$ to 0.0018. We selected this rescaling to produce the qualitative changes in dynamics needed to produce the tripod duty cycle; although it may not be biologically realistic, we obtain similar results from other parameter rescalings that produce qualitatively similar dynamics, as we discuss further in Section 2.4. We also constrain the definition of entrainment to require that the duty cycle of IN4 remains within 10% the duty cycle of $\beta$; note that the choice of 10% is arbitrary, and we obtain similar results if this number is increased. See Figure 25 for a comparison of duty cycles between the tripodal and tetrapodal cases. In the tripodal case, stability is not lost before the failure of this duty cycle constraint, and so quasi-entrainment is not observed. On the other hand, where the tetrapodal case is entrained, it remains within its prescribed duty cycle tolerance. See Figure 26 for a comparison of these regions in parameter space. In the CPG, the mechanisms of entrainment failure and recovery remain consistent with those discussed for the tetrapodal case, although the particular parameter values at which entrainment and failure occur will differ between the two walking patterns.

## 2.4  Discussion

Animal locomotion requires highly coordinated activity of the segmental neuronal networks that control limb movements [137, 124, 118, 15, 18, 10, 66]. Experiments have shown that sensory signals originating from the extremities play a pivotal role in controlling locomotion patterns by acting on central networks [6, 27, 5, 12, 46, 17]. Based on past data [5, 4], we assume that these central networks contain CPGs as driving elements. Using a neural network model created from stick insect data [126, 129, 127, 122], which incorporates a possible set-up of how sensory information is transferred to the CPG, we investigated in this work (1) the conditions under which sensory input entrains the CPG, (2) the mechanisms by which entrainment of the CPG by sensory signals is lost, and (3) the restoration of entrainment by changes in bottom-up or top down input or walking speed.

Slow walking stick insects heavily rely on movement, force, load and ground contact
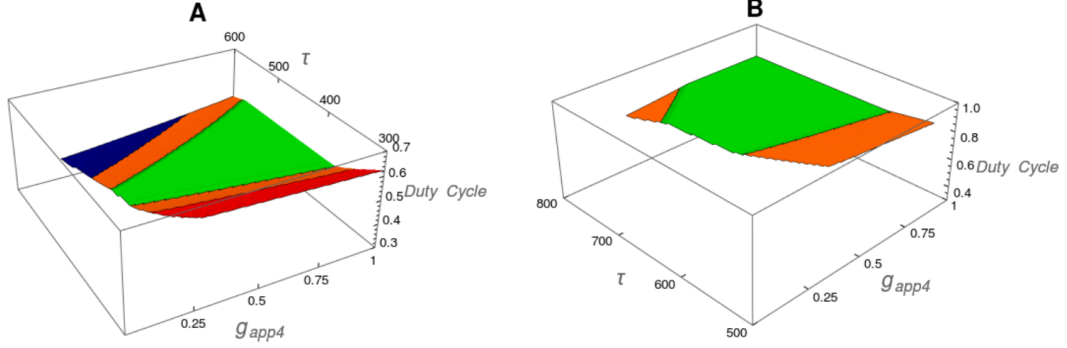
Figure 25: **Comparison of tripodal and tetrapodal entrainment regions in parameter space. A:** The duty cycles of the interneurons in the tripodal case undergo extreme drift. For parameter values in the green region, the duty cycle is nearly exactly that of $\beta$, while in the orange region duty cycles have drifted away from $\beta$, but are still considered entrained. The red and blue regions consist of parameter values yielding duty cycles of more than 10% away from 1/2-1/2 (too long and too short, respectively). **B:** The duty cycles of the interneurons in the tetrapodal case do not drift excessively. Although entrainment can be lost due to loss of stability or knee clearance failure, the duty cycles do not deflect from their prescribed level. Green and orange regions have duty cycles that agree with, and are within $\pm 10\%$ of, that of $\beta$, respectively.
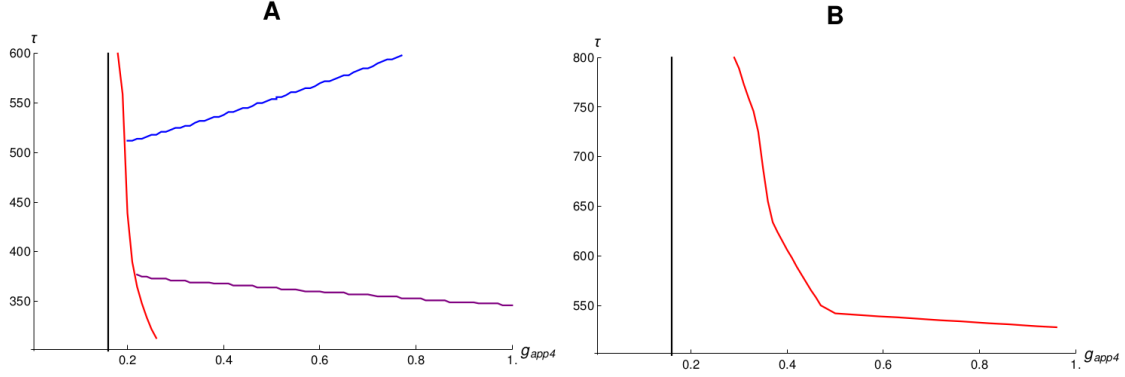
Figure 26: **The boundaries of entrainment regions in parameter space for the two cases. A: Tripodal, B:Tetrapodal** To the left of the red curve, which depends on $\tau$, entrainment fails due to a knee collision, while to the left of the black curve, the driven $v_1$-nullcline retains a quiescent fixed point, making entrainment impossible, regardless of $\tau$. The blue and purple curves denote boundaries where the duty cycle deviates $\pm 10\%$ from 1/2-1/2. Thus, the region above and to the right of the red curve in each diagram features successful, stable knee clearance and the subregion below the blue and above the purple curves is where the duty cycle meets our entrainment constraints in the tripodal case. The tetrapodal regime does not lose entrainment due to duty cycle drift.

signals to establish coordinated walking patterns [27, 5, 97]. In particular, the CPGs that are assumed to control the movements of the individual leg joints may be entrained by these sensory feedback signals during walking. The results of our study fit nicely into this view of a *decentralized control* in stick insect walking as we have emphasized that with sufficient bottom-up signaling to both CPG units, top-down modulation is unnecessary, meaning that the CPG system can maintain entrainment even without top-down drive.

The basic setup of the CPG was chosen such that in the absence of any input C1 has a fixed point at a hyperpolarized voltage, corresponding to its silent phase, while C2 has a fixed point at a depolarized voltage, corresponding to tonic activation of the cell. We have shown that entrainment of the CPG involves the recruitment of C1 by $\beta$ followed by a switch from C1 active to C2 active either due to release of C2 by C1, for relatively small $g_{app_2}$, or to escape of C2, for relatively large $g_{app_2}$. In both cases, entrainment can be lost if $\tau$ becomes too large, corresponding to a slowing of locomotion to an extent that a different walking pattern is needed, or if $g_{app_1}$ or $g_{app_2}$ is chosen to lie at a problematic level; presumably, for slower patterns such as a metachronal pattern, the duty cycle of the $\beta$ signal would need to change, which we do not consider here. Loss of entrainment is seen in experimental results. Grabowska et al. [121] found that amputation of stick insect middle legs leads to loss of entrainment in front and hind legs. In this case, the removal of peripheral and central influences of the middle legs might effectively reduce $g_{app_1}, g_{app_2}$ to problematic levels. Indeed, in the reverse experiment, Borgmann et al. [2] found that a single stepping middle leg induces a generalized increase in activity in the protractor/retractor motoneurons of the neighboring ThC joints, suggesting a strong drive from the middle leg that would be lost with amputation. In our model, failures arise if C1 or C2 becomes too dominant or the two become too independent, such that co-activation can occur; recovery requires restoring an appropriate tuning that allows C1 and C2 to activate in alternation, once each per input cycle. These constraints stress the point that even in the case of decentralized control of slower walking, central inputs may still play a role in providing an appropriate activation level to the CPG, and a balance between the central and sensory inputs to the CPG is still necessary, meaning that top-down control has to be in a suitable regime for successful CPG entrainment by bottom-up signaling to occur.

Fast running cockroaches are believed to depend much less on sensory feedback signals to establish coordinated walking patterns than stick insects do. Locomotion is assumed to be instead controlled more centrally, presumably by a greater top-down input from higher brain regions. This pushes the CPG into its pacemaker mode, in which it requires less sensory information to be entrained ([75, 130, 9]; for a review on the comparison of cockroach and stick insect locomotion, see [7, 109]). In accordance with this distinction we observed that, if we push the CPG into its pacemaker mode, the range of entrainment expands to include very small values of $g_{syn41}$, which allows a robust entrainment of the CPG by bottom-up signaling even with an almost complete loss of the connection between the interneuron subsystem and the CPG.

In addition, we have shown that the top-down drives in the CPG system offer a powerful control system and that tuning these drive levels together with the strengths of the bottom-up inputs would allow for the maintenance of entrainment over the broadest possible range of walking paces. Interestingly, experimental evidence does suggest that top-down pathways may also induce neuromodulation of sensory feedback signals [62]. The results from section 2.3.2.2, in particular, reveal a parameter variation mechanism that can allow the CPG duty cycle to deviate significantly from that of the $\beta$ input and bottom-up signals from IN3 and IN4. Importantly, the resulting regimes should not be interpreted as a representation of alternative walking patterns such as tripodal stepping, because we do not vary the duty cycle of $\beta$, as would arise with an altered time course of ground contact. Rather, these mechanisms could relate to other walking modalities, such as turning or backwards stepping, which are manifested at the level of the ThC joint. Rosenbaum and colleagues [13] have shown in the stick insect that backwards stepping requires a change in muscle activation with protractor and retractor completely switching their roles while no major adjustments in sensory duty cycle are necessary (see also [27]). One possible mechanism for the performance of curve walking or sharp tuning is to change the walking direction of the inner middle leg from forward to backward [122, 100]; see also [28]. In an earlier model of stick insect walking [129], we have made detailed suggestions as to how rhythmic stepping might be generated by the CPGs, how this activity might be transmitted to the corresponding motoneurons (MNs), and how the latter might control the activity of the related muscles. There, we

suggested a mechanism by which MN activity could be modified by a premotor network (cf. Figure 2, IN1 and IN2 in [129], not part of the circuit analyzed here) without changing the activity of the CPG itself. An interesting direction for future work could be to combine the changes in CPG duty cycle with the patterning by the premotor network to achieve additional stepping patterns.

This work points to several forms of robustness within the overall ThC circuit. One aspect of robustness that emerges from our work is that the loss of signals from the interneurons conveying the bottom-up sensory information (IN3 and IN4) does not prevent the entrainment of the CPG. Specifically, we found that oscillating drive from IN4 to C1 alone or oscillating inhibition from IN3 to C2 alone was capable of maintaining entrainment, under certain conditions on parameters. This robustness points to some redundancy in the interneuron subsystem, as has been previously proposed [126, 129]. The neural connectivity of the subsystem that conveys the sensory information is not known; however, it is based on reasonable physiological assumptions on stick insect neurophysiology. Our results show that entrainment of the CPG by sensory signals from the legs can be achieved with a circuit even simpler than the one proposed in the above-mentioned modeling studies. Another form of robustness that we observe is that overall, the CPG duty cycle matches that of the sensory signal over a wide parameter range, especially in the tetrapodal case (Figure 25). This invariance is appropriate because we are not explicitly modeling transitions between walking patterns, with associated changes in sensory information from other legs and properties of $\beta$, but rather the maintenance of patterns across variations in walking pace and signaling strength. Combining our analysis with dynamics of $\beta$ to model fluid changes between stepping patterns, such as might occur as the insect accelerates, remains for future work. In fact, although we do not implement a closed-loop signaling system that allows CPG output to impact the properties of $\beta$, we can obtain a preliminary idea of how a closed-loop version of our model would work in certain cases by referring to Figures 13 and 16. There, we see entrainment patterns that feature CPG phase durations that are out of register with the input duty cycle, $\alpha$. In both cases, there is a switch from C1 to C2 activity during the phase when $\beta$ is still on. If the CPG output in turn shortened $\alpha$, then the earlier termination of $\beta$ would be unlikely to affect the CPG pattern and the new entrained pattern would be

expected to continue. Confirming this type of outcome, and exploring closed-loop effects in other scenarios, would require additional work, however, and remains for a future study.

A final form of robustness that we observe is that, although most of the results that we present focus on the tetrapodal walking pattern, the same analysis that we present in detail for the tetrapodal pattern also demonstrates that the mechanisms of entrainment failure and recovery in the CPG remain the same for the tripodal pattern (see subsection 2.3.3.3). The particular parameter constellations associated with each entrainment or failure regime for the two walking patterns have a partial overlap (e.g., see Figures 25, 26). Interestingly, for intra-network and top-down connection strengths that lie in a shared entrainment regime, our model suggests that a direct transition or downshifting from an entrained tripodal to an entrained tetrapodal pattern would be possible, via an abrupt change in $\tau$ (period) together with $\alpha$ (duty cycle). Similarly, if a stick insect steps into a hole or its leg strikes an obstacle, then it starts to perform searching movements to look for a good foothold. After a foothold is found, the animal resumes walking at a slow pace. This means that if the animals would walk in a tripodal pattern and encounter a large obstacle or hole, then there would be a period in which the legs would perform searching movements and end up re-ordered before walking was continued in the slower tetrapodal pattern. A set of network connection strengths that gives entrainment for both patterns would facilitate such an adjustment.

In addition to a relatively simple, open-loop signaling system with fixed input duty cycle, our model includes a minimal CPG circuit and relatively reduced representations of the dynamics of the neurons in the network. The reductions in our model allow us to analyze thoroughly the mechanisms involved in entrainment, its failure, and its recovery and the roles of specific signals within the system. To do so, we used methods based on projections of model trajectories to phase planes corresponding to individual circuit components, as have been used for a variety of studies in past work (e.g., [40, 39, 38]). These methods are more appropriate here than commonly used approaches based on phase response curves (e.g., [115, 33, 21]), due to the strong coupling between the network components and the fact that these components are not oscillators in the absence of coupling. A cost of this tractability is that our model can only inform us about changes in walking patterns that are distinguishable at the level of a single joint, i.e. walking patterns that can be distinguished

by changes in cycle period and duty cycle of the CPG that we investigate. It cannot provide insights about alternative walking patterns observed in stick insects, such as mirror-image tetrapodal patterns for which the period and duty cycle do not change at the level of the ThC joint. Our model produces changes in duty cycle arising at the CPG level with changes in cycle period, but we do not study gradual changes of input duty cycle and the continuum of patterns that may occur in a gradual transition between tetrapodal and tripodal cases as input duty cycle and cycle period are modulated together. Another cost of using a reduced model is that a single parameter set does not produce entrainment for both tetrapodal and tripodal patterns; rather, we change the time constant $\epsilon_i$ of the gating variable $h$ for the model INs as part of the switch. From an analytical point of view, this switch makes sense because it gives qualitatively appropriate IN and CPG dynamics, but it is not biologically reasonable; we obtain similar dynamics and entrainment results if we change $g_{l_{in}}, e_l$, and $g_{app_4}$ instead, for example, but then a shift in the range of $\tau$ is needed. A more realistic model would allow for a more biologically feasible switching mechanism but with a loss of analytical tractability.

Our findings represent effects that we predict will arise in more complicated circuits, computational or physiological, that operate according the same general principles: rhythm generation via a half-center-like mechanisms that yields alternations of activity of the neurons projecting to antagonistic muscle groups, subject to ascending sensory input and tonic central drive. We did not exhaustively catalogue the possible stable solutions in the system, ignoring, for example, higher-order entrainment with period exceeding twice that of the ascending input. We also do not claim to have identified every possible entrainment failure mechanism that could arise through variation of the multiple control parameters in our model. The analysis of chaotic or other exotic solutions occurring as entrainment is lost or gained (e.g., [21]) is also outside the scope of this study; while mathematically interesting, these solutions seem to be limited to narrow parameter bands and are likely of limited importance to the topics of our study.

# 3.0 Striatal Motor Control Circuit Under Bicuculline

## 3.1 Introduction

Despite comprising only about 2% of striatal neurons, tonically active cholinergic interneurons (TAN) are thought to play a crucial role in mediating striatal activity ([44], [88], [36]). These TANs are the sole identified striatal source of acetylcholine (ACh), and nearly all striatal neurons are thought to possess ACh-sensitive muscarinic receptors of various subtypes, particularly M1 and M2/4 ([43], [20]). These receptors serve a number of roles, with M4 acting to inhibit firing, while M1 effects are more complex, allowing for the promotion of firing ([76], [42], [144]). Recently, there has been a focused interest in the ways that ACh may impact or contribute to various basal ganglia related neurological disorders, such as Parkinson's Disease and Tourette's Syndrome ([50], [79], [42], [123], [105]). Although TANs are prominent at the forefront of striatal research, there are few mathematical models of these neurons. Developing such models represents an important step in advancing this research, to provide a tool for hypothesis testing and generating mechanistic predictions.

Experimental recordings have provided observations of TAN activity patterns, as well as insights into the nature and properties of the individual currents expressed in TANs ([84], [69]). Given the availability of this level of information about TANs, we sought to develop a conductance-based model that includes experimentally observed currents and to find parameter regimes in which various TAN behaviors are captured. Further, there are numerous reports characterizing TAN activity under various experimental conditions ([24]; [74]; [84]; [14]; [136]; [69]), and we tuned parameters to ensure that our model matches these experimental benchmarks at a qualitative and, when possible, quantitative level. Finally, we used the model to simulate the dynamics of TANs, along with spiny projection neurons (SPNs), under conditions associated with tic production in an animal model of Tourette's Syndrome (TS), both as a form of model validation and to provide some insight into the mechanisms of tic expression in the striatum.

TS is a disorder affecting about 1% of people throughout their lifetimes, characterized

by the emergence of motor tics (Conciecao et al., 2017). Animal models of tic production have been successfully developed via the application of bicuculline to striatum and have shown a characteristic surge and pause of activity in SPNs ([65]; [64]; Bronfeld and Bar-Gad, 2013). We hypothesized that ACh plays an important role in the striatal expression of motor tics, and this led us to focus on the behavior of TANs during tic generation and resulting dynamics of striatal ACh. Specifically, using our new TAN model, we considered the associated ACh dynamics and the effects of ACh on TANs and SPNs. While neuromodulator levels have typically been treated as fixed parameters when incorporated into conductance-based models ([30], [140], [99], [89]), we opted to include the dynamics of the maximal conductances associated with neuromodulator-related currents, allowing our model system to emulate the ACh dynamics resulting from brief surges of synaptic input to TANs. We consider two aspects of these responses: cholinergic effects directly on the effective input associated with surge initiation and autoregulation effects of heightened ACh on the TANs themselves. We show that with the combination of these two components, the model can reproduce features of TAN and SPN dynamics observed experimentally in animal models where the striatal application of bicuculline yields tic production ([64], Bronfeld and Bar-Gad, 2013). Thus, we predict both of these impacts of ACh release contribute to the surge and pause response associated with tic production in this setting.

## 3.2    Materials and Methods

### 3.2.1    Overview of Model Components

We develop a conductance-based model of a striatal TAN. In addition to typical sodium, potassium, and leak currents ($I_{Na}$, $I_K$, and $I_L$, respectively), the model includes a variety of other currents identified in TANs: sag and inward rectifier currents ($I_h$ and $I_{IR}$), a persistent sodium current ($I_{NaP}$), a slow calcium current ($I_{Ca}$), a T-type current ($I_T$), medium and slow afterhyperpolarization (AHP) currents ($I_{mAHP}$ and $I_{sAHP}$), and an M-type potassium current $I_M$ (sometimes called persistent K) ([78], [81], [120], [24], [77], [16], [84], [14], [79],

63

Tan and Bullock, 2008, [73], [72], [99], [136], [141], [143], [123], [69]). Finally, we include an applied current representing combined cortical and thalamic inputs to a TAN ($I_{appT}$).

In addition to the gating variables associated with these currents, the model includes dynamics of the concentrations of extacellular potassium ($K_o$) and intracellular sodium ($Na_i$) ions and of local levels of ACh, which is released by TAN spiking, along with the feedback effects of ACh on other model components. $K_o$ and $Na_i$ dynamics are modelled in a standard fashion (Baretto and Cressman, 2011). As for ACh, there appear to have been few quantitative measurements related to its dynamics and its effects as mediated through muscarinic receptors (M1, M2 and M4), although the latter have been characterized qualitatively ([85], [89]). Thus we implement its dynamics as follows: ACh is released into the extracellular space by TANs at a rate that depends on TAN spiking, while after its release, ACh binds and unbinds to different receptors at associated rates and is also degraded at some rate by acetylcholinesterase (AChE). See Fig. 27 All simulations were performed in XPP-AUTO (Ermentrout, 2002)

For the study of surge and pause dynamics, we also simulate a previously published SPN model ([107]). This model includes sodium, potassium, M-type, and leak currents plus inputs. We do not include synaptic inhibition from the model SPN to the model TAN because the relevant experimental model includes the application of bicuculline ([64], Bronfeld and Bar-Gad, 2013), which we assume, for simplicity, induces a complete block of inhibition.

Others ([82]; [98]; [108]; [140]; [99]) have modeled the effects of different fixed levels of neuromodulators in conductance-based models by adjusting maximal conductance levels in the currents impacted by these factors. Building off of this idea, we model the temporally evolving effects of ACh on receptor activation through the dynamics of various conductances. Of particular interest, we have a spike-enhancing M1 current in the SPN ([80]; [91]), a spike-reducing M2/4 current in the TAN, and M2/4-like suppression of cortical and thalamic inputs to both cells ([20], [106]). In some simulations, we seek to separate out the factors contributing to the surge-pause pattern. For those results, either we allow the conductances of the intrinsic M currents of the SPNs and TANs to vary, while the input strength remains independent of the ACh level, or vice versa.
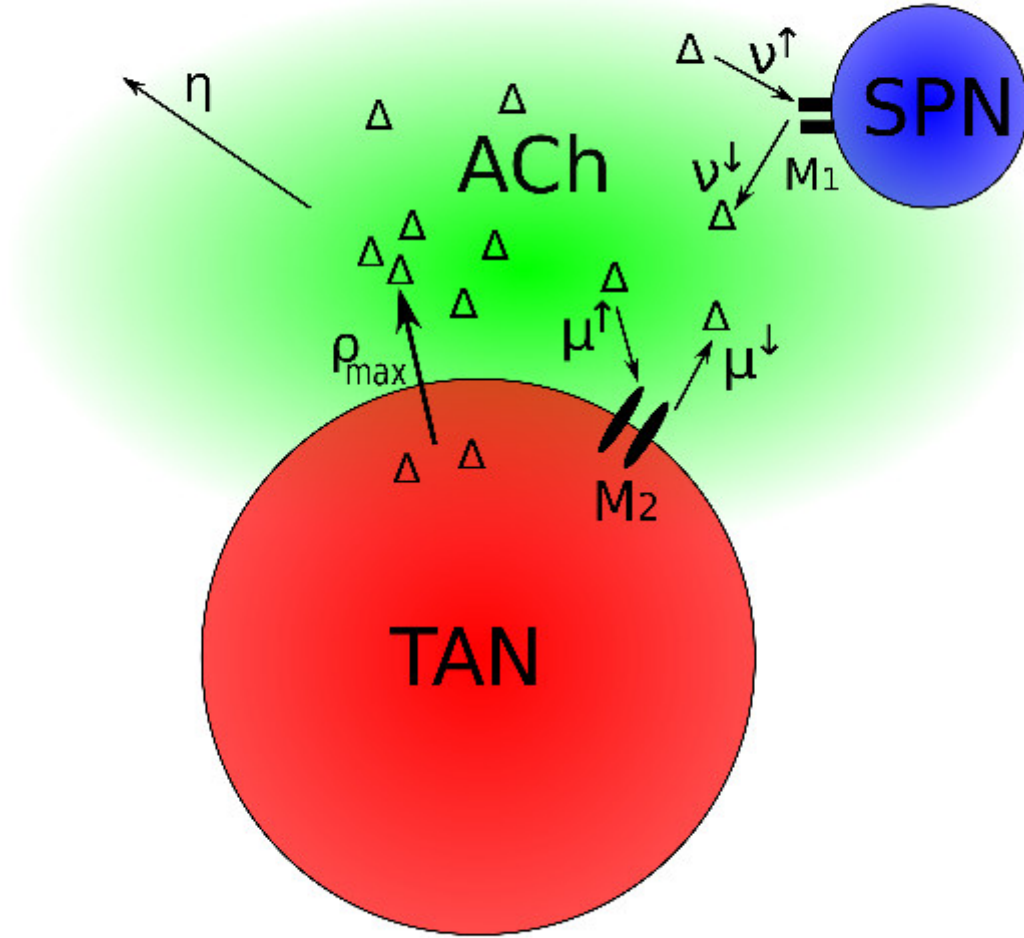
Figure 27: **Diagram of Cell Interactions**. ACh is released from TAN firing at a rate $\rho_{max}$ and degraded by AChE at a rate $\eta$. Extracellular ACh becomes bound and unbound to M receptors at rates $\mu^{\uparrow,\downarrow}$ and $\nu^{\uparrow,\downarrow}$

### 3.2.2    Model Details

The current balance equations for our model neurons take the form

$$
\begin{aligned}
C_T \tfrac{d}{dt} v_T = &\ - \quad I_{Na} - I_K - I_{leak} - I_h - I_{IR} \\
&\ - \quad I_{Ca} - I_{sAHP} - I_{mAHP} \\
&\ - \quad I_t - I_{NaP} - I_{MT} \\
&\ + \quad I_{appT} + \zeta_T W_T(t) \\
C_S \tfrac{d}{dt} v_S = &\ - \quad I_{Na} - I_K - I_{leak} - I_{MS} \\
&\ + \quad I_{appS} + \zeta_S W_S(t)
\end{aligned}
\tag{4}
$$

where the subscripts $T$ and $S$ denote the TAN and SPN, respectively. The currents are given in the Hodgkin-Huxley formulation as

$$
\begin{aligned}
I_{Na} &= g_{Na} m_\infty^3(v) h (v - E_{Na}) \\
I_K &= g_K n^4 (v - E_K) \\
I_{IR} &= g_{IR}(v - E_K) \\
I_h &= g_h p (v - E_h) \\
I_T &= g_T a^3 (v - E_{Ca}) \\
I_{Ca} &= g_{Ca} s^2 (v - E_{Ca}) \\
I_{NaP} &= g_{NaP} r (v - E_{Na}) \\
I_{sAHP} &= g_{sAHP} \xi (v - E_K) \\
I_{mAHP} &= g_{mAHP} ([Ca]/([Ca] + k_m)) (v - E_K) \\
I_L &= g_L (v - E_L)
\end{aligned}
\tag{5}
$$

with $I_{MT}, I_{MS}, I_{appT}, I_{appS}$ all defined later. The terms $W_T(t), W_S(t)$ refer to Wiener processes used to include noise in certain simulations, with a scalable amplitude $\zeta_T$ or $\zeta_S$, respectively. In most cases, we found that the inclusion of noise did not significantly alter the qualitative behavior of the model TAN and so it is excluded from TAN simulations (i.e., $\zeta_T = 0$) unless otherwise noted.

Sodium and potassium activation functions $m, n$ and sodium inactivation function $h$ are adapted from [86]. The fast activation function for $I_{Na}$ is treated as instantaneous, and takes

the form

$$m_\infty(v) = \exp(\frac{45v}{7})(v + 28)/\tau_m(v)$$

where

$$\tau_m(v) := -0.128 + 2.105 \exp(\frac{v}{10}) + \exp(\frac{45v}{7})(v + 28).$$

The other gating variables in the TAN model obey differential equations that are a standard part of the Hodgkin-Huxley framework, of the form

$$\frac{d}{dt}X = (X_\infty(v) - X)/\tau_X. \tag{6}$$

For $h$ and $n$, the function $X_\infty(v)$ is determined by $\alpha_X(v) = X_\infty(v)/\tau_X$, and $\beta_X(v) = (1 - X_\infty(v))/\tau_X$ where

$$\alpha_h(v) = 0.35 \exp((-v + 51)/20)$$

$$\beta_h(v) = 5/(\exp(-(v + 21)/10) + 1)$$

$$\alpha_n(v) = -.05(v + 27/(\exp(-(v + 27)/10) - 1)$$

$$\beta_n(v) = -0.625 \exp(-(v + 37)/80).$$

Otherwise, activation and inactivation variables evolve under equation (6) with $X_\infty(v) = 1/(1 + \exp(\frac{v - \theta_X}{\sigma_X}))$ for parameters $\tau_X, \theta_X$, and $\sigma_X$ specific to each variable (see Table 2). Here $\tau_x$, $\theta_X$, and $\sigma_X$ denote the time constant, half activation (inactivation) and slope of the gating function $X_\infty$, respectively.

Additional model components include the calcium-related equations

$$\frac{d}{dt}[Ca] = \epsilon(-I_{Ca}(v) - k_{Ca}[Ca] - I_T(v)),$$
$$\frac{d}{dt}\xi = a_\xi[Ca]\xi - b_\xi\xi,$$

and ion equations

$$\tau_{K_o}\frac{d}{dt}K_o = \gamma\delta I_K - 2\delta I_{pump} - I_{glia} - I_{diff}$$
$$\tau_{Na_i}\frac{d}{dt}Na_i = -\gamma I_{Na} - 3I_{pump}$$

with

$$I_{pump} = p/(1 + \exp(\tfrac{25 - Na_i}{3}))$$
$$(1/(1 + \exp(5.5 - K_o))),$$
$$I_{glia} = g/(1 + \exp(\tfrac{18 - K_o}{2.5})),$$
$$I_{diff} = \varepsilon_{diff}(K_o - K_{base}).$$

These concentrations affect the potassium and sodium reversal potentials, respectively given by

$$E_K = 26.64 \log(\tfrac{K_o}{K_i}),$$
$$E_{Na} = 26.64 \log(\tfrac{Na_o}{Na_i}),$$

where $K_i = 188 - Na_i$ and $Na_o = 144 - \delta(Na_i - 18)$.

Of particular importance in our simulations are the two $M$-currents,

$$\begin{aligned} I_{MT} &= g_{M2/4}m_T(v_T - E_K), \\ I_{MS} &= g_{M1}m_S(v_S - E_K), \end{aligned} \tag{7}$$

that contribute to the TAN and SPN membrane potential dynamics, respectively. The gating function $m_T$ is as in equation (6) and the gating function $m_S$ comes from [107]. However, the maximal conductance of each current can be modulated by the effects of ACh on associated M-type receptors through a G-protein dependent second messenger type system ([144]).

To separate effects of ACh on these intrinsic currents from effects on extrinsic inputs, we combine a fixed, ACh-insensitive conductance term, $\hat{g}_*$, and a dynamic, ACh-sensitive conductance term, $\tilde{g}_*$, which we average to compute the instantaneous maximal $g_*$

$$g_{M2/4} = \tfrac{\hat{g}_{M2/4} + \tilde{g}_{M2/4}}{2}$$

$$g_{M1} = \tfrac{\hat{g}_{M1} + \tilde{g}_{M1}}{2}$$

where

$$\begin{aligned} \tau_{M2/4}\tfrac{d}{dt}\tilde{g}_{M2/4} &= g_{M2/4max}/(1 + \exp(\tfrac{A_T - \theta_{\tilde{g}T}}{\sigma_{\tilde{g}T}})) \\ &\quad - \tilde{g}_{M2/4} \\ \tau_{M1}\tfrac{d}{dt}\tilde{g}_{M1} &= g_{M1max}/(1 + \exp(\tfrac{A_S - \theta_{\tilde{g}S}}{\sigma_{\tilde{g}S}})) \\ &\quad - \tilde{g}_{M1}. \end{aligned} \tag{8}$$

Rather than voltage, these conductance equations depend on $A_T$ and $A_S$, which represent the level of ACh bound to M-type receptors on TANs and SPNs, respectively.

The currents $I_{appT}, I_{appS}$ corresponding to synaptic inputs are also affected by ACh, so we implement a similar approach, with an ACh-insensitive part $\hat{I}_{app}$ and a dynamic ACh-sensitive part $\tilde{I}_{app}$, again with

$$I_{appT} = \frac{\hat{I}_{appT} + \tilde{I}_{appT}}{2}$$

$$I_{appS} = \frac{\hat{I}_{appS} + \tilde{I}_{appS}}{2}$$

and

$$\tau_{appT} \frac{d}{dt} \tilde{I}_{appT} = I_T / (1 + \exp(\frac{A_{exc} - \theta_{appT}}{\sigma_{appT}})) - \tilde{I}_{appT}$$
$$\tau_{appS} \frac{d}{dt} \tilde{I}_{appS} = I_S / (1 + \exp(\frac{A_{exc} - \theta_{appS}}{\sigma_{appS}})) - \tilde{I}_{appS}. \tag{9}$$

Importantly, $\hat{I}_{appT}, \hat{I}_{appS}, I_T, I_S$ are all prescribed functions of time, each given by what we call a railcar or a ramp. A railcar input jumps to 0.5 at time $t_0$, and back to 0 at time $t_f = t_0 + 250$ms. A ramp input jumps to 0.5 at time $t_0$ms, and decays linearly to 0 at time $t_f = t_0 + 2000$ms. For ACh sensitive currents, these values define an envelope for the effective input, which is modulated by $A_{exc}$ (See Fig. 28)

Each dynamic equation in (8), (9) has an associated term for its level of bound of ACh, given by $A_T$ for TAN M-receptors, $A_S$ for SPN M-receptors, and $A_{exc}$ for both applied currents. We model the dynamics of the level of free ACh, which depends on TAN firing, and bound ACh phenomenologically, through the differential equations

$$\begin{aligned}
\frac{d}{dt} ACh &= \rho_{max} / (1 + \exp(\frac{v_T - \theta_\rho}{\sigma_\rho})) - \eta ACh \\
&\quad - \tau^* \frac{ACh^2}{ACh^2 + \alpha^2} + A_{exc} - \mu^\uparrow ACh + \mu^\downarrow A_T \\
&\quad - \nu^\uparrow ACh + \nu^\downarrow A_S \\
\frac{d}{dt} A_T &= \mu^\uparrow ACh - \mu^\downarrow A_T \\
\frac{d}{dt} A_S &= \nu^\uparrow ACh - \nu^\downarrow A_S \\
\frac{d}{dt} A_{exc} &= \frac{ACh^2}{ACh^2 + \alpha^2} - A_{exc}.
\end{aligned} \tag{10}$$

In system (10), $\rho_{max}$ and the sigmoid function that it multiplies represent the voltage-dependent release of ACh by elevations in TAN voltage (spikes), $\eta$ represents the degradation of ACh by acetylcholinesterase, and $\alpha$ is the half-saturation level for the ACh bound to receptors that modulate inputs, $A_{exc}$, i.e. when $ACh = \alpha$, $A_{exc}$ equilibrates to 0.5. TANs

and SPNs are known to receive asymmetric input from thalamus and cortex ([20]; [70]; [96]; [141]). For simplicity's sake we combine coritcal and thalamic inputs into a single applied current for each cell type, and to account for the asymmetry in their inputs, we consider inputs to the TAN and SPN independently, leaving us with an applied current to TAN and a separate applied current to SPN. Finally, $\mu^{\uparrow,\downarrow}$ and $\nu^{\uparrow,\downarrow}$ represent M-receptor binding and unbinding rates of ACh in TANs and SPNs, respectively, and $\tau^*$ is a temporal scaling parameter set to $1$ ms$^{-1}$. Note that these phenomenological equations are dimensionless and the variables involved should not be viewed as concentrations.

We use TAN model to simulate TAN behavior in a variety of scenarios implemented in previous experiments. In those experiments in which TTX is applied to the bath, there is no firing, and hence no ACh release (Figs. 29, 30, 32). In those experiments in which only individual cells were being stimulated at any given time, only a small amount of ACh would be released from this firing, since the whole population is mostly unaltered. Thus, we reasoned that the firing of the stimulated cells should have little effect on net ACh levels, and accordingly we turned off ACh release from the model during our simulations of these effects (Figs. 33, 34). In the *in vitro* experiments involving apamin, apamin was applied to the bath; hence, we treat our model cell's activity as characteristic of the activity that would occur in many TAN neurons, and thus we include ACh effects in these simulations (Fig. 35). Similarly, in experimental recordings of baseline firing modes, the entire TAN population is free to fire, so we maintain dynamic cholinergic effects in the model (Fig. 29, 30).

### 3.2.3 Tic Expresion

To simulate the neural activity underlying motor tic production, we provided the TAN and SPN with an excitatory input current consisting of an ACh-sensitive input component with dynamics given by equations (9), (10) and an ACh-insensitive input component $\hat{I}_{appT}, \hat{I}_{appS}$, respectively. For each of these input components, on each simulation, we used either the railcar or the ramp temporal profile. In some simulations, we set the amplitude of the ACh-insensitive input to 0, effectively using an ACh-sensitive input alone. In simulations with nonzero inputs of both types we always ensured that the two inputs had different

70

Table 2: **Main TAN Model Parameters.** † denotes values used for experiments with apamin application, †† denotes values used for irregular firing, ∗ denotes values used for noisy irregular firing.

| Parameter | Value | Parameter | Value |
|---|---|---|---|
| $C_T$ ($\mu$F/cm$^2$) | 1 | $g_{Na}$ (mS/cm$^2$) | 25, 30$^{\dagger\dagger}$ |
| $g_K$ (mS/cm$^2$) | 15, 10$^\dagger$ | $g_{IR}$ (mS/cm$^2$) | 2.75 |
| $g_h$ (mS/cm$^2$) | 1.2, 0.8$^{\dagger\dagger}$ | $g_T$ (mS/cm$^2$) | 0.15 |
| $g_{Ca}$ (mS/cm$^2$) | 0.2 | $g_{NaP}$ (mS/cm$^2$) | 0.1, 0.02$^{\dagger\dagger}$ |
| $g_{sAHP}$ (mS/cm$^2$) | 0.05, .5$^\dagger$ | $g_{mAHP}$ (mS/cm$^2$) | 15, 60$^\dagger$, 2$^{\dagger\dagger}$ |
| $g_L$ (mS/cm$^2$) | 0.08 | $E_h$ (mV) | -60 |
| $E_{NaP}$ (mV) | 45 | $E_L$ (mV) | -53, $-60^{\dagger\dagger}$ |
| $\theta_{IR}$ (mV) | -90 | $\sigma_{IR}$ (mV) | 6 |
| $\theta_p$ (mV) | -90 | $\sigma_p$ (mV) | 6 |
| $\tau_p$ (ms) | 600, 1200$^\dagger$ | $\theta_a$ (mV) | -63 |
| $\sigma_a$ (mV) | 7.8 | $\theta_s$ (mV) | 140 |
| $\sigma_s$ (mV) | 4 | $\theta_r$ (mV) | -50 |
| $\sigma_r$ (mV) | 3.1 | $\tau_r$ (ms) | 1 |
| $a_\xi$ | 0.5 | $b_\xi$ | .05 |
| $k_m$ | 15, 3$^{\dagger\dagger}$ | $\varepsilon$ | 0.0001, 5$(10^{-5})^{\dagger\dagger}$ |
| $\zeta_T$ | 0, 8$^*$ | | |

Table 3: **M-Current Parameters**

| Parameter | Value |
|---|---|
| $\hat{g}_{M2/4}$ (mS/cm$^2$) | 0.04 |
| $\theta_{M2/4}$ (mV) | -50 |
| $\sigma_{M2/4}$ (mV) | 5 |
| $\tau_{M2/4}$ (ms) | 500 |
| $g_{M2/4max}$ (mS/cm$^2$) | 8 |
| $\theta_{\tilde{g}T}$ | 9 |
| $\sigma_{\tilde{g}T}$ | -0.1 |
| $\tau_{tildegT}$ (ms) | 500 |
| $\hat{g}_{M1}$ (mS/cm$^2$) | 1.3 |
| $g_{M1max}$ (mS/cm$^2$) | 3 |
| $\theta_{\tilde{g}S}$ | 2 |
| $\sigma_{\tilde{g}S}$ | 1.8 |
| $\tau_{\tilde{g}S}$ (ms) | 100 |

Table 4: **Cholinergic Subsystem Parameters**

| Parameter | Value |
| --- | --- |
| $\eta$ | 0.005 |
| $\rho_{max}$ | 10 |
| $\theta_\rho$ | 1 |
| $\sigma_\rho$ | -0.1 |
| $\alpha$ | 2 |
| $\mu^{\uparrow}$ | 0.01 |
| $\mu^{\downarrow}$ | 0.01 |
| $\nu^{\uparrow}$ | 0.01 |
| $\nu^{\downarrow}$ | 0.03 |

Table 5: **Ion Subsystem Parameters**

| Parameter | Value |
| --- | --- |
| $\gamma$ | 0.04 |
| $\delta$ | 1 |
| $p$ | 1.25 |
| $\varepsilon_{diff}$ | 1.333 |
| $k_{base}$ | 7 |
| $\tau_{K_o}$ | 1000 |
| $\tau_{Na_i}$ | 1000 |
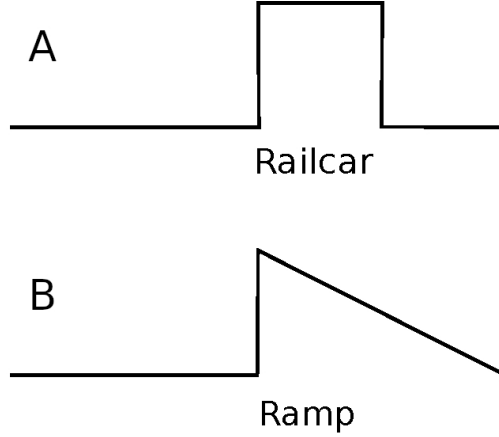
Figure 28: **Input Profiles**. Schematic illustration of the time courses of the maximal in-put levels associated with **(A)** railcar and **(B)** ramp profiles. The effective input to each postsynaptic neuron will be less than the maximum due to effects of ACh.

profiles (i.e., ACh-sensitive railcar with ACh-insensitive ramp or vice versa), for a total of four input profiles considered. In all simulations, the onset of SPN activity preceded the onset of TAN activity by 50ms, so we supply SPN with input 50ms before we supply TAN input. ([64]). See Fig. 28

### 3.3   Results

#### 3.3.1   Firing Modes

In spite of their name, TANs exhibit a variety of firing patterns, which we broadly characterize as tonic firing, burst-pause firing, and irregular firing. Each firing mode also yields an associated behavior in response to the application of TTX ([84]).

In the tonic firing regime, neurons engage in tonic 4-15 Hz spiking with shallow hyper-polarizations reaching -67 mV ([24], [84], [73]). In its tonic firing mode, our model produces a steady firing rate of about 8 Hz, with hyperpolarizations reaching -69 mV. To achieve

this firing regime, we set $K_{base}$ to 7 mM, corresponding to a potassium reversal potential $E_K \approx$ -86.5 mV. In the tonic firing regime, application of TTX yields a steady voltage above firing threshold ([84]), which our model reproduces (Figs. 29, 30A). In this regime, firing is slow enough that $p$, the gating variable of the sag current $I_h$, remains relatively active, and overcomes the hyperpolarizing effects of $I_M$ and $I_{mAHP}$, blocking the engagement of $I_{IR}$ and thus preventing deep hyperpolarizations.

The burst-pause firing mode is characterized by 0.5-1.5 second bursts of firing separated by deep hyperpolarizations to near the K$^+$ reversal potential ([84], [72]). The mechanism that allows TANs to undergo this deep, prolonged pause is thought to be important in regulating learning, as the cessation of TAN activity disinhibits dopamine terminals (Conceicao et al, 2017). To put our model into burst-pause firing mode, we only need to adjust the $K_{base}$ parameter to 6 mM, corresponding to a reversal potential $E_K$ of about -90 mV. In vivo, variability in the baseline potassium concentration could result from various effects including differences in activity of other local neurons, changes in vascular properties, or neuromodulation ([23]; [139], [52]). With this single parameter change, our simulation achieves an average firing rate of about 13Hz with each burst-pause cycle lasting about 650 ms and with its deepest hyperpolarization reaching about -85 mV. As the cell fires, the magnitude of its sag current, $I_h$, decays. Once $I_h$ has decayed sufficiently, the inward rectifier current, $I_{IR}$, amplified by the lower potassium reversal potential, is engaged, which induces deep hyperpolarizations. In this scenario, $I_M$ and $I_{mAHP}$ contribute to driving voltage low enough to engage $I_{IR}$, but are not required. At the resulting low voltages, $I_h$ can recover, but its slow time constant delays this effect (Fig. 29B, Fig 31). In this regime, TTX induces a slow, non-spiking oscillation with a period of up to about 2 s.

Irregular firing can be viewed as a mixture of the previous two regimes, featuring slow firing separated by both shallow and deep hyperpolarizations, as well as large subthreshold oscillations without firing. The deep hyperpolarizations in this regime in our model reach about -80 mV, consistent with experimental recordings ([84], [72]). While the firing in this regime in our deterministic model is periodic, we do obtain large subthreshold oscillations, and inclusion of a small amplitude noise term recovers the more irregular characteristic of this firing pattern observed experimentally (Fig. 29D). TTX causes slow oscillations in the
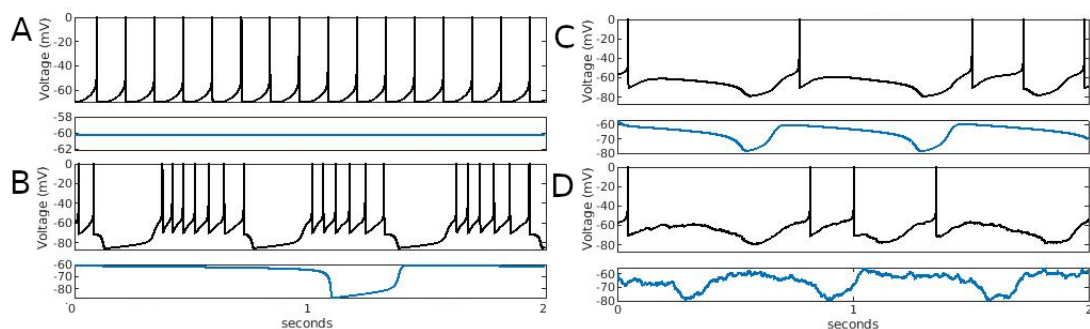
Figure 29: **Simulated TAN Firing Modes and Responses to TTX. A: Tonic Firing.**
Upper: The cell fires at a steady rate of about 8 Hz. The hyperpolarization is shallow. Lower:
TTX suppresses firing, and the cell remains at a steady voltage of -60 mV. **B: Burst-Pause
Firing.** Upper: The cell exhibits periods of rapid firing, punctuated by quiescence. Lower:
Under TTX the cell engages in slow, deep oscillations. **C: Irregular Firing.** Upper: The
cell exhibits both shallow and deep hyperpolarizations. Overall, the firing rate is much lower
than in the other modes, and there are epochs where action potentials fail to materialize.
Lower: Under TTX, slow, regular oscillations occur, although they are faster and shallower
than the burst-pause case. **D: Irregular Firing With Noise.** With noise added, the
irregularity of the spiking is more pronounced. Note that in all simulations the total duration
is 2 seconds, which matches the length of the time bar in the experimental traces in Figure
30.
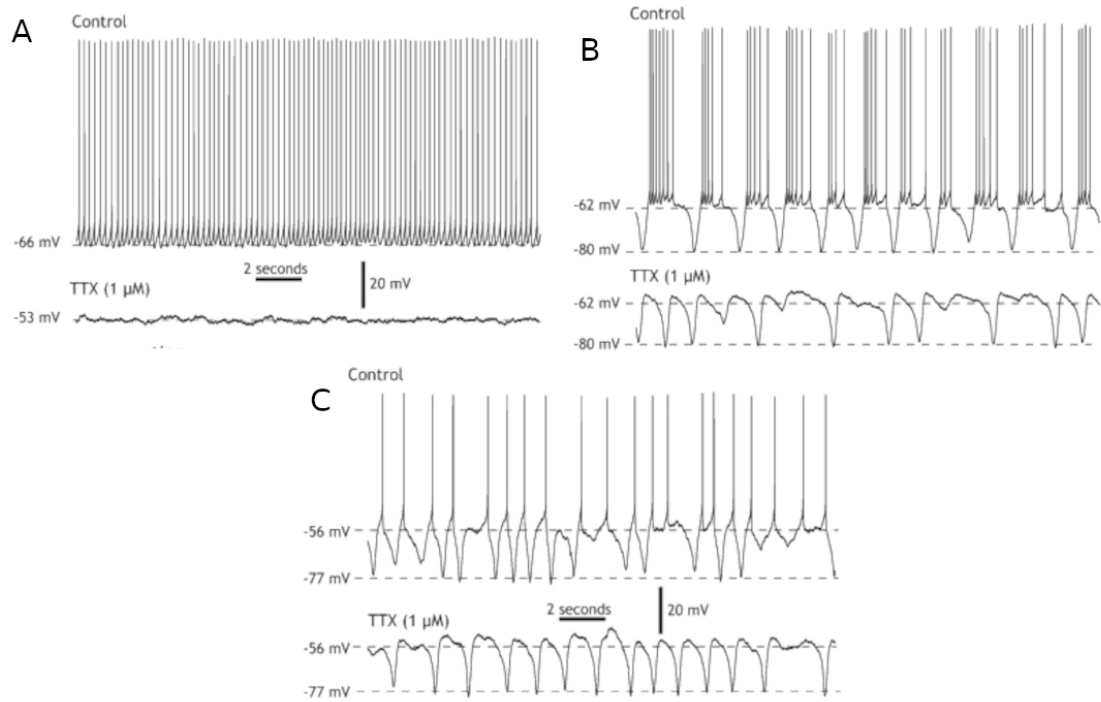
Figure 30: **Experimentally Observed TAN Firing Modes and Responses to TTX.**
**A: Tonic Firing.** Tonic firing with and without TTX. **B: Burst-Pause Firing.** Burst-Pause firing with and without TTX. **C: Irregular Firing.** Irregular firing with and without TTX. Reproduced from [84].
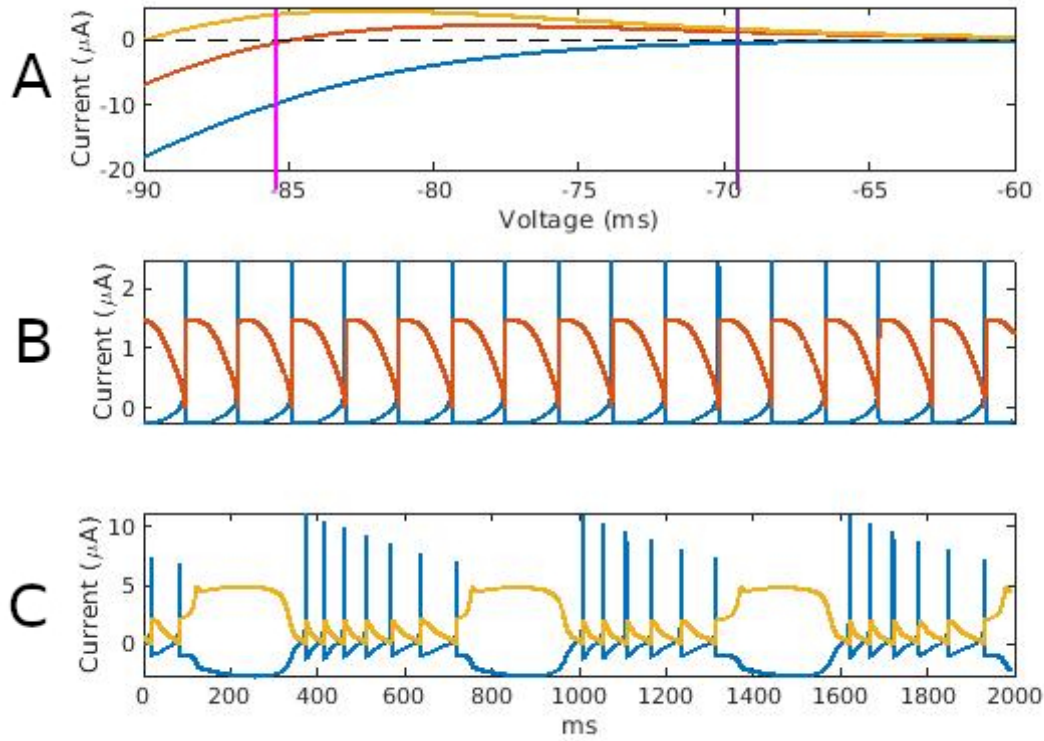
Figure 31: **IR and Sag Currents. A**: Steady-state values of the sag current $I_h$ (blue), inward rectifier current $I_{IR}$ in the tonic firing regime (orange), and $I_{IR}$ in the burst-pause regime (yellow) when voltage is clamped to various levels. Magenta (left) and purple (right) vertical lines indicate the voltages of the deepest hyperpolarizations occurring in burst-pause and tonic firing, respectively. **B**: Time courses of $I_h$ (blue) and $I_{IR}$ (orange) in tonic firing. **C**: Time courses of $I_h$ (blue) and $I_{IR}$ (yellow) currents during burst-pause firing. Negative sag currents help depolarize the membrane potential from a hyperpolarized state. In B and C, the spikes in $I_h$ correspond to voltage spikes, while the periods of elevated $I_{IR}$ correspond to epochs of lower voltage between spikes or bursts of spikes. Note the expanded range of the vertical axis in C relative to B.

irregular firing mode, which are shallower and slower than in the burst-pause case ([84], [72]) (Figs. 29, 30C,D).

### 3.3.2 Experimental Benchmarks

Since TANs are most known for their tonic behavior, we validated our TAN model by testing the ability of the model, with the parameter values associated with the tonic firing regime, to reproduce four benchmarks derived from experimental observations, beyond its basic firing pattern and behavior under TTX. This step provided much more rigorous constraints on the model parameter values than those resulting from simply matching the tonic firing pattern alone.

[136] found that the voltage time course of a TAN given a trapezoidal input current after TTX application exhibits a characteristic form. Of particular note is the "undershoot" effect following the removal of input, where the voltage of the cell falls below its baseline level, which helps to expose the time courses of subthreshold currents that are thought to be important in generating TAN pauses. Our model matches the following qualitative features when stimulated with a trapezoidal current under TTX (Fig. 32): A concave rise in voltage, a small voltage overshoot followed by a plateau when the applied current plateaus, and a deeper voltage undershoot falling below the baseline resting potential before the applied current ends, followed by a slow return to baseline. $I_h$ is inactive at these voltages, and it appears that $I_M$ and $I_{mAHP}$ are responsible for the undershoot, as they have not returned to their baseline level by the end of the input current (Fig. 32C).

Experimental results suggest that the sag current $I_h$ plays an important role in allowing the cell to maintain tonic firing by preventing the engagement of $I_{IR}$ ([136], [69]). If a TAN is supplied with a sufficiently hyperpolarizing applied current, then its firing ceases and its voltage remains hyperpolarized until the current is removed. However, after an initial deep hyperpolarization, there is a partial recovery of potential through the recruitment of $I_h$. Once the hyperpolarizing current is removed, the cell recovers to a higher firing rate than baseline, due to the deinactivation of $I_{Na}$ that occurs during hyperpolarization. Our model captures this effect, including its dependence on the strength of the applied current (Fig. 33).
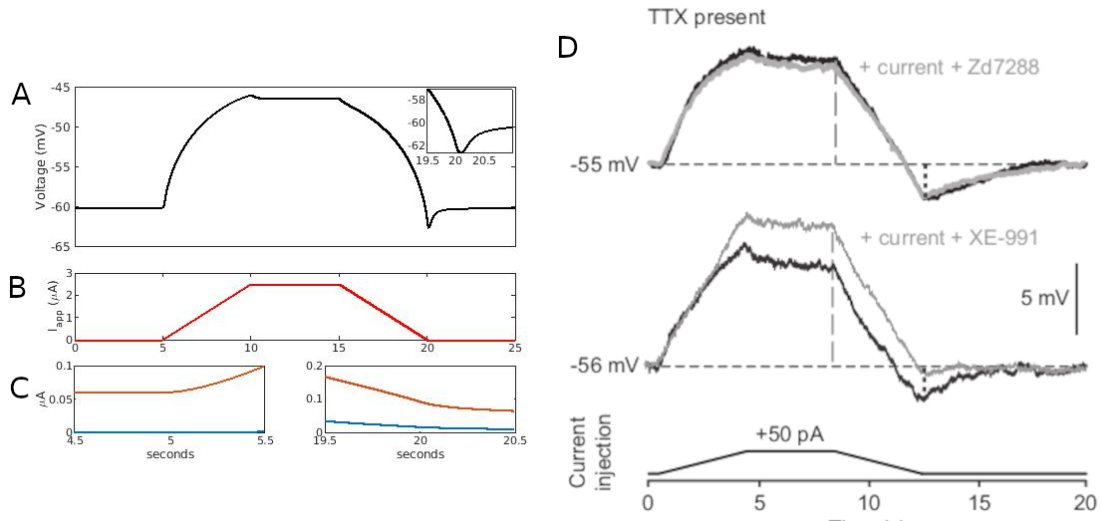
Figure 32: **Trapezoidal Input.** Upper: Behavior of the model TAN under TTX. **A:** Voltage time course to the application of input (**B**) shows a slight overshoot followed by a plateau. A significant undershoot occurs as input is removed, with the cell falling below baseline voltage prior to the complete removal of input. Inset in **A:** A closer view of the undershoot. **C:** $I_M$ (blue) and $I_{mAHP}$ (orange) currents. Their slow decay is responsible for the undershoot. **D:** Experimentally recorded TAN responses to trapezoidal current injection (bottom) under TTX. Grey traces are experiments with $I_h$ blocker Zd7288 (top) and $Kv7.2/7.3$ blocker XE-991 (middle). Panel D reproduced from [136].
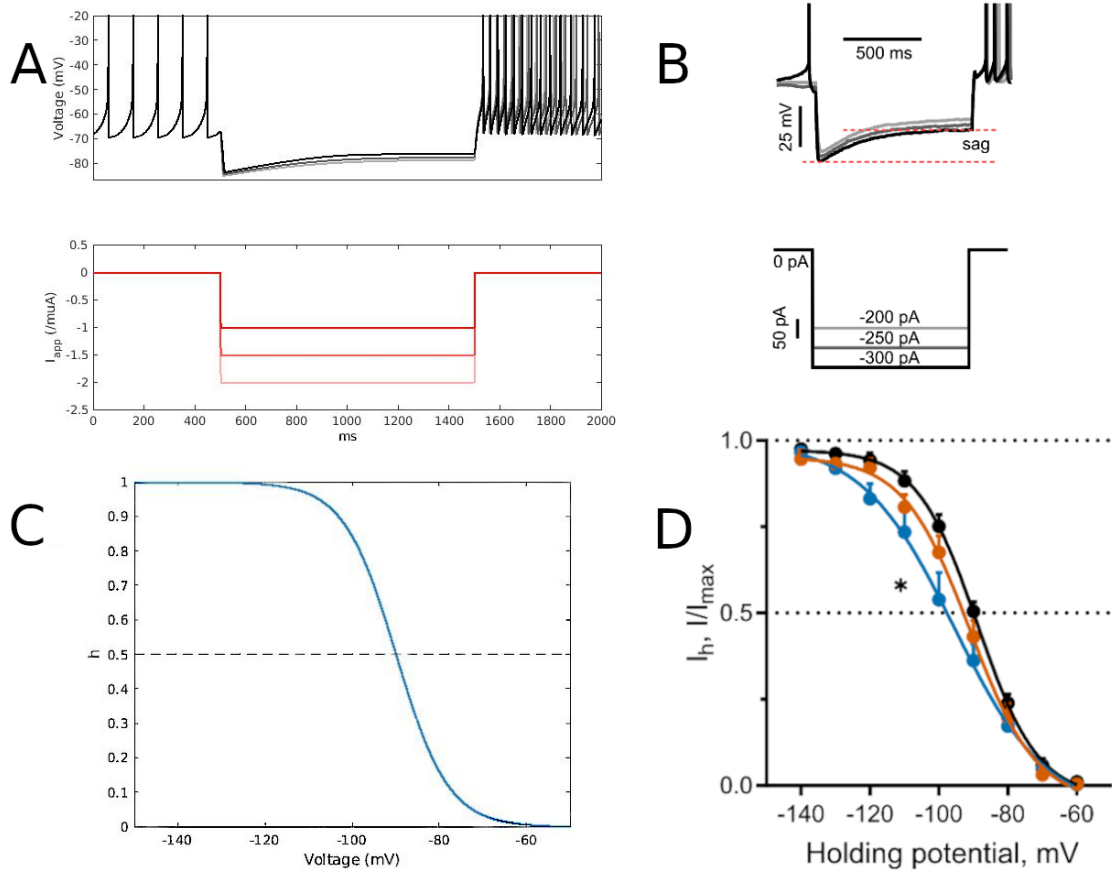
Figure 33: **Application of Hyperpolarizing Input Reveals the Sag Current, $I_h$. A:** Model cell Voltage traces (upper) in response to hyperpolarizing currents of various levels (lower). Note the slow recovery after the initial hyperpolarization and the accelerated spiking after removal of the input. **B:** Experimental hyperpolarization and sag. **C:** Steady-state $I_h$ inactivation curve, $p_\infty(v)$. Note half activation $\theta_p$=-90 mV and slope $\sigma_p$=6. **D:** Experimental measurement of sag inactivation under voltage clamp. Black curve from control mice, blue curve from mice after dopamine depletion via 6-OHDA administration, and orange curve from dopamine depleted mice receiving levodopa treatment. Panels B, D reproduced from Figure 3C, 3F, [69], published under the Creative Commons Attribution 4.0 International Public License CC BY 4.0

When a positive current is applied to a tonically spiking TAN, the neuron exhibits a predictable increase in firing rate. More importantly, when this drive is removed, the TAN undergoes a deep, prolonged pause before returning to normal firing ([25], [14]). Our model captures these effects as well as the brief elevation of potential above the original baseline, or rebound depolarization, as spiking returns (Fig. 34). In this case, while the cell is spiking, $I_h$ decays while $I_M$ and $I_{mAHP}$ build up, similarly to what occurs in the burst-pause firing mode, and, as in Fig. 32, these two currents remain elevated when input is removed. This change in current balance promotes hyperpolarization, which in turn yields engagement of $I_{IR}$; these currents counteract the recovery of $I_h$ and contribute to the amplitude of the hyperpolarization.

The pause that we obtain in simulations lasts for approximately 750 ms, which lies within the range of 390ms-1400ms reported in experiments ([25], [14]). This duration is controllable through $\tau_p$, the membrane time constant of $I_h$, and $\epsilon$, the time constant of $[Ca^{2+}]$. It is important to note that despite some similarities, this type of pause appears to be distinct from those arising in burst-pause firing. That is, pauses in both cases involve a decay in the sag current $I_h$ during a period of rapid firing, contributions of $I_M$ and $I_{mAHP}$, as in the "undershoot" phenomenon seen in Fig. 32 C, and the recruitment of $I_{IR}$. $I_h$ is, however, required for spiking to recover, and if the experiment is run with $I_h$ blocked, the cell will never recover from its post-input hyperpolarization, and voltage remains at -85mV.

When apamin is applied to a TAN in tonic firing mode, the neuron engages in short bursts with very rapid firing, followed by deep hyperpolarizations, due to $I_{sAHP}$ ([14]). To simulate apamin we block $I_{mAHP}$, and our model exhibits the experimentally observed firing pattern. The new pattern results because when apamin reduces $I_{mAHP}$, a speedup of firing and a corresponding buildup of calcium result. This accumulation in turn engages the apamin-insensitive current $I_{sAHP}$, which brings the voltage low enough to engage $I_{IR}$, resulting in a deep hyperpolarization as seen in burst-pause firing (Fig 35).
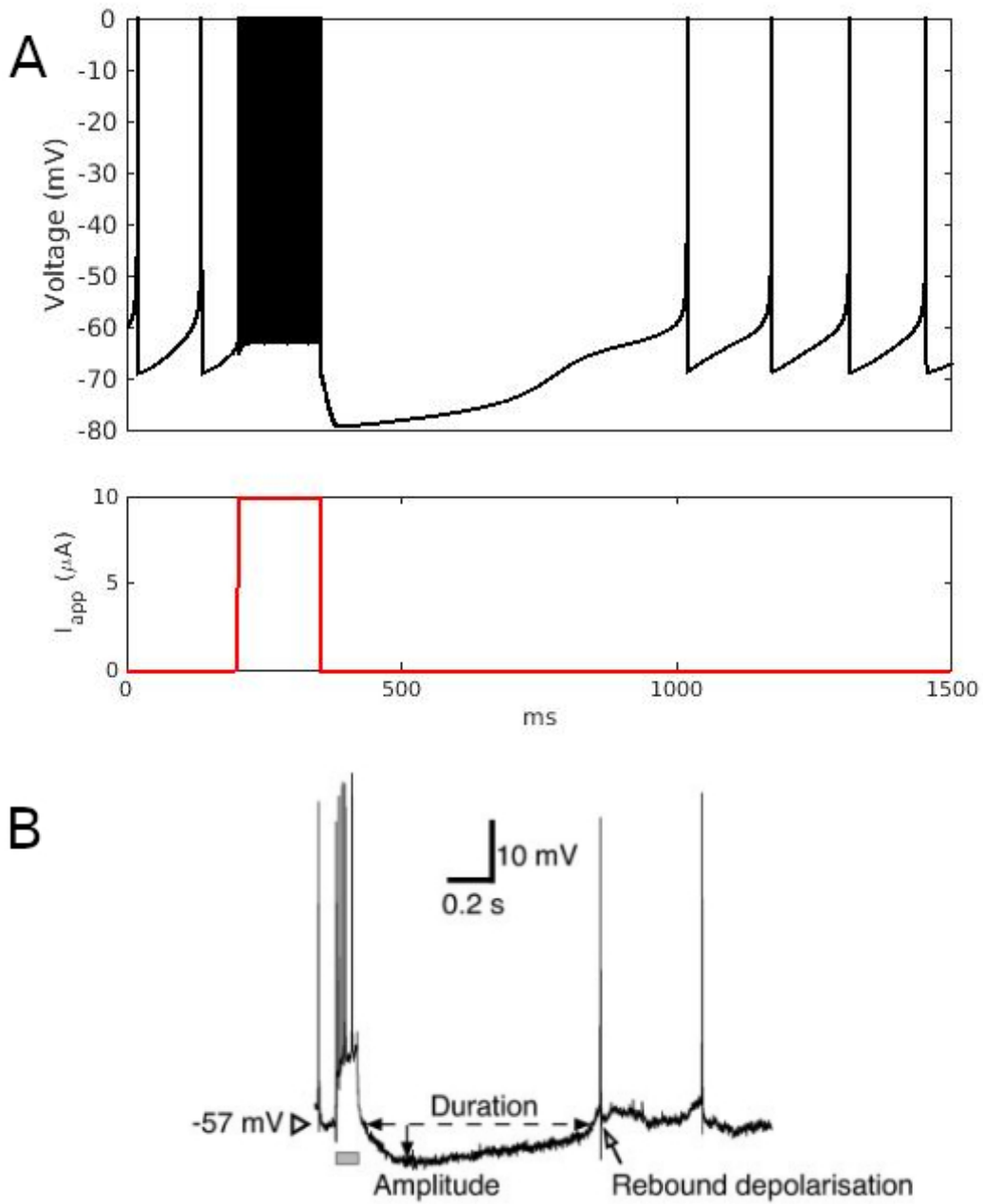
Figure 34: **Application and Removal of Depolarizing Input Current. A:** After removal of a strong, depolarizing input current, the TAN voltage undergoes a prolonged hyperpolarization and pause in spiking. **B:** Experimentally recorded voltage time course corresponding to the application and removal of strong depolarizing input. Panel B reproduced from Figure 2A, [25], Copyright 2004, Society for Neuroscience
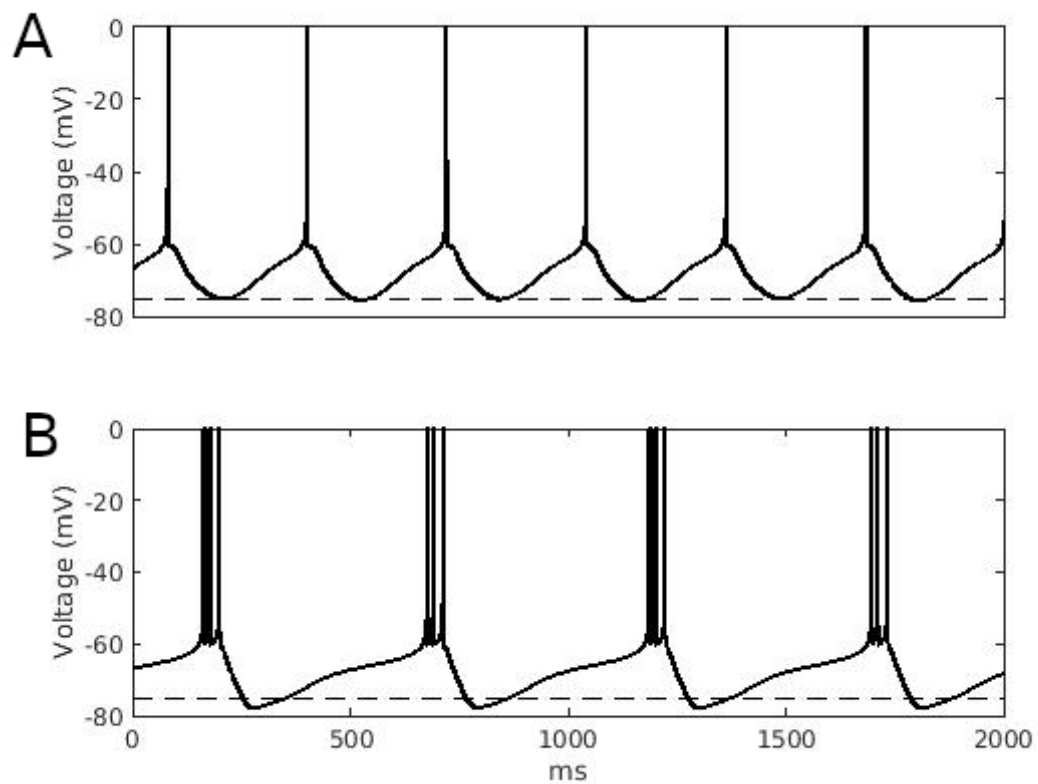
Figure 35:  **Effects of Apamin.**  **A:** Tonic firing with apamin-sensitive parameter regime **B:** With the application of apamin, we see rapid spiking followed by deeper hyperpolarizations.

### 3.3.3 Tic Expression:

During a motor tic induced by bicuculline application, TANs and SPNs exhibit a surge in firing followed by a prolonged pause ([64], [32]). The factor that is most likely to initiate this surge is a strong excitatory input – indeed, these striatal populations are targeted by excitatory synaptic projections from the cortex and thalamus – and hence we apply such an input to our model TAN and SPN to simulate their tic-related activity. In this section, we explore the capacity of inputs with various temporal profiles to induce the observed surge-pause spiking profiles and we investigate the mechanisms involved in this process; since bicuculline was applied in the experiments in which this activity was observed, we exclude synaptic inhibition from our model, which implies that activity pauses must result from other factors.

In our simulations, the initial surge in TAN activity induced by excitatory input leads to a rise in ACh, which causes (see equation (8)) the SPN M-current conductance $g_{M1}$ to decrease, promoting SPN firing. ACh has opposite effects on $M1$ versus $M2$ and $M4$ receptors. Thus, the rising ACh causes the TAN M-current conductance $g_{M2/4}$ to *increase*, initiating a TAN pause. With the pause now initiated, ACh decays below its baseline level, causing $g_{M1}$ to rise and $g_{M2/4}$ to fall. High $g_{M1}$ suppresses SPN firing, but, since the TAN is in a pause phase, the low $g_{M2/4}$ does not cause TAN activity to immediately resume. The elevation of $g_{M1}$ is strong enough to prevent SPN firing even with some sustained excitatory input to the SPN. Thus, the response of the SPN to excitatory input is strongly impacted by the response of the TAN and the ACh profile that results.

We now analyze this dynamics under certain input profiles (Fig. 28). Specifically, we assume that the excitatory inputs to TANs and SPNs are either sustained, which we call the railcar case, or adapting, which we call the ramp case, since these are common cortical firing patterns. Since the behavior of the SPN is largely modulated by ACh, we first investigate the response of the TAN. To consider a TAN response as a successful representation of experimental observations, we require an initial surge in TAN firing, followed by a single prolonged pause before a return to baseline spiking activity.

In the railcar input profile, "railcar" refers to the input time course: the maximum
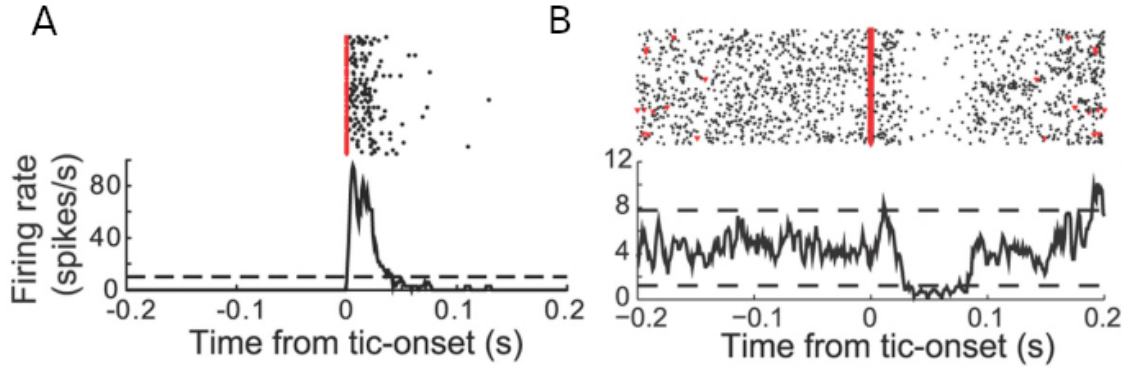
Figure 36: **Striatal activity During Tic Expression.** Raster plot and average firing rate of **A:** an SPN and **B:** a TAN, across multiple motor tics induced in the presence of bicuculline. Raster plots (upper) and firing rate traces (lower) are aligned with tic onset at time 0 (red vertical lines). Reproduced from Figure 2B, 2E, [64], Published under the Creative Commons Attribution-Noncommercial-Share Alike 3.0 Unported License (CC-BY-NC-SA 3.0) doi

applied input strength jumps from 0 $\mu$A to 0.5$\mu$A abruptly at onset and then jumps back to 0 abruptly at a specified offset time, while "long" refers to the offset time of $t_f = t_0 + 250$ ms, with $t_0$ chosen sufficiently large such that the input duration outlasts the TAN surge. We consider both an input that we call "ACh-sensitive", in reference to the fact that the effective input strength is modulated by ACh (see *Materials and Methods*, equations (9), (10)), which weakens the effective current felt by the postsynaptic neuron, and an "ACh-insensitive" input, which has a strength that is not modulated by ACh. In each case, the binding of ACh to $M_{2/4}$ receptors in the model TAN, represented by $A_T$, increases the M-current conductance, suppressing firing and allowing for the TAN pause despite continued excitation (Fig 37). As the TAN enters its pause phase, ACh decays and input recovers. For sufficiently long input, this recovery may induce oscillations, which could range from small subthreshold oscillations if the M-conductance dominates over the input (Fig 37 A) to a second surge in spiking, not seen in experiments, if the input duration is long enough (not

Figure 37: **Simulated TAN Responses to Railcar Type Input Surge**. **A: ACh sensitive Railcar Input** The initial surge (top) suppresses TAN firing before the end of the input (middle), followed by a slow return to baseline. Notice, however, that input is briefly weakened during the surge due to the rise in ACh. This rise in ACh causes a delayed rise in $g_{M2/4}$, allowing for the initiation of the pause. **B: ACh insensitive Railcar Input** The initial surge is now stronger, leading to very rapid TAN firing. When firing resumes, a single spike is enough to initiate a second pause, due to a high $g_{M2/4}$

shown). In the ACh-insensitive case, TAN firing is more intense than in the ACh-sensitive case, resulting in a higher level of ACh and thus higher M-current conductance $g_{M2/4}$. This higher conductance then decays slowly, so that even after a pause twice as long as the ACh-sensitive case, there is enough residual M-current to initiate a secondary pause after a single spik (Fig 37 B). We conclude that the ACh-sensitive railcar input profile that lasts beyond the surge itself is consistent with experimental observations of surge-pause dynamics in TANs as long as the input duration does not outlast the elevation in the intrinsic M-current, whereas the ACh-insensitive railcar profile would not yield the observed surge-pause pattern. Since neuronal firing often features spike frequency adaptation, as an alternative to the railcar input current, we investigate a ramp input for which the maximal value decays over 2000 ms from an inital strength of 0.5 $\mu A$. For concreteness, we assume that after an abrupt initial jump to a maximum, the applied input strength decays linearly. As with the railcar profile, we compare outcomes obtained when input is either ACh-sensitive or ACh-insensitive. As before, due to the ACh buildup associated with the surge, the $M_{2/4}$ receptors of the TAN can induce a pause. In the ACh-sensitive case, the recovery of the effective input current associated with ACh decay during the pause, together with the more gradual decay in the applied input strength itself, shortens the pause and allows spiking to return sooner than previously (Fig 37 A vs. Fig 38 A). On the other hand, in the ACh-insensitive case, a more intense initial surge in TAN spiking results in a greater ACh and $g_{M2/4}$ response, causing a rise in M-current that initiates a second pause when the input decays sufficiently, and even a third pause resulting from elevated firing due to rebound depolarization (Fig 38 B). Thus, as in the railcar case, our simulations suggest that the ACh-sensitive scenario is consistent with experimental surge-pause dynamics, albeit with a shorter pause than for a railcar input, while the ACh-insensitive scenario is not.

In the ramp case, we could change the rate at which the input decays. For inputs that decay too slowly, TAN activity exhibits a secondary increase, yielding overly rapid TAN spiking after the pause or even a second surge and pause cycle not seen in the data (not shown). If inputs are removed too quickly, however, then because $g_{M2/4}$ remains elevated, the correspondingly strong M-current induces a secondary pause. Thus, adapting input only gives a TAN response consistent with experimental observations if its decay rate is neither
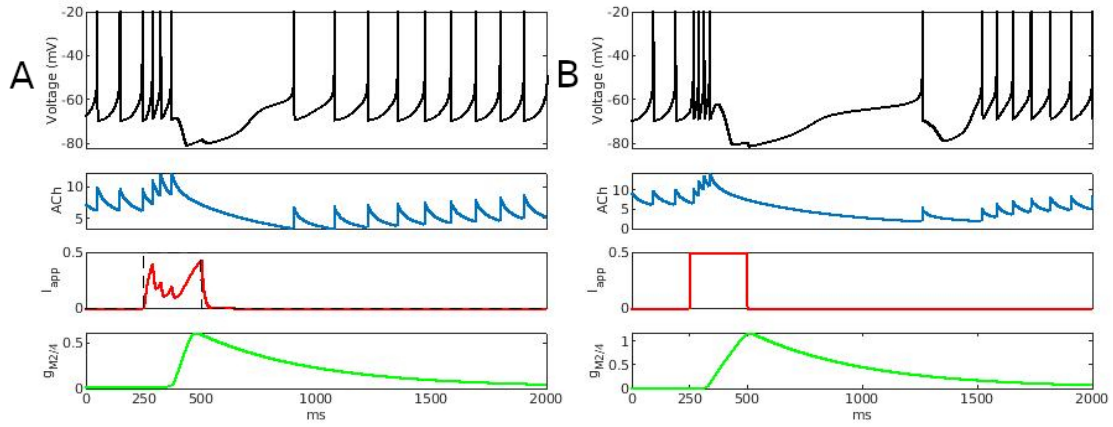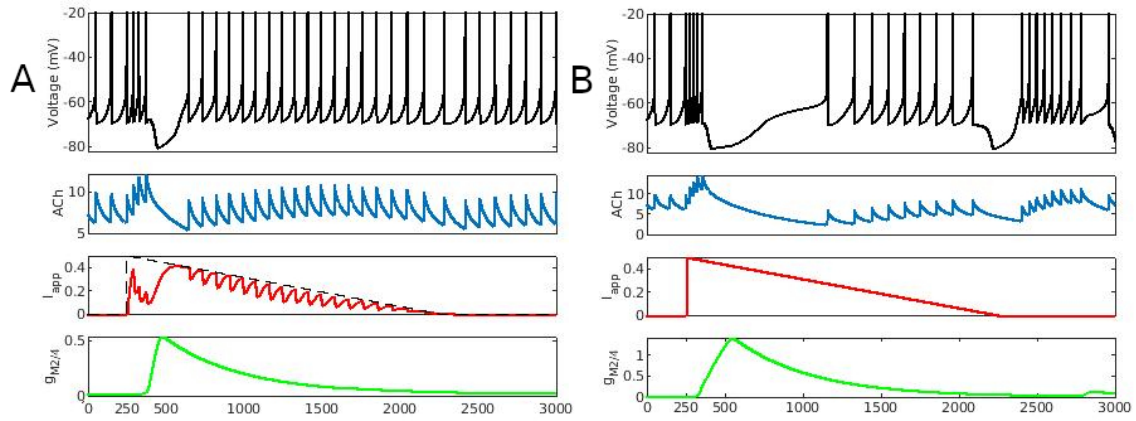
Figure 38: **Simulated TAN Responses to Ramp Type Input Surge**. **A: ACh sensitive Ramp Input** The initial surge (top) suppresses TAN firing, while both input and ACh make a slow return to baseline. As in the railcar case, input is briefly weakened during the surge due to the rise in ACh. This rise in ACh causes a delayed rise in $g_{M2/4}$, allowing for the initiation of the pause. **B: ACh insensitive Ramp Input** Although ACh remains below baseline when firing recovers, residual M-current allows for a secondary pause when input has fully decayed.

too slow nor too fast. (Fig. 39).

In the previous input profile cases, we examined inputs that outlast the duration of the actual TAN surge. Another possibility is that the inputs are shorter; indeed, in theory, the surge termination could be a direct consequence of the cessation of the input. Thus, as a final case, we consider railcar inputs that are shorter than the length of the TAN surge, so that $t_f = t_0 + 60$ ms. As before, TANs surge with the rising input, and the response to ACh-insensitve input exceeds that to ACh-sensitive input, but in both cases, due to the short nature of the input, the pause is induced by the loss of the input, as predicted, rather than due to the rise of $g_{M2/4}$. Again the ACh-sensitive input case behaves appropriately, with a rise in ACh and a single pause, but now, because the surge is terminated early, the ACh-insensitve case does not have as great an effect on ACh as it did with a longer input, so $g_{M2/4}$ does not grow to levels that initiate secondary pauses (compare Fig 37 B to Fig 40 B). Thus, we see that for short input surges, TAN behavior is consistent with experimental observations irrespective of the ACh-sensitivity of the excitatory input it receives.

We have now established that certain types of input yield the types of TAN surge-pause responses observed experimentally, while others do not. Next, we consider the firing profile of our model SPN subject to similar inputs as the TAN but shifted 50 ms earlier in time ([64]) and also impacted by the ACh profile generated by the TAN response. Experiments show that SPNs produce a qualitatively similar surge-pause pattern to TANs during tic expression (Fig. 36). After excluding TAN responses that are inconsistent with experimental data, we are left with four input profiles that we have considered that can produce an appropriate TAN surge-pause pattern. We investigated how the SPN response to each of these input profiles compares to the experimentally-observed SPN surge-pause. The model SPN is tuned so that with its baseline input and maximal M-conductance it fires at roughly 0.5Hz, with a rate that increases with the application of excitatory drive. The SPN neuron has no intrinsic mechanism to suppress a surge in firing in the presence of sustained excitation. Thus, its surge must end entirely due to changes in inputs or through effects of ACh release by the model TAN.

$M_1$-type receptors on the SPN facilitate firing in the presence of ACh, unlike the $M_{2/4}$ receptors found in TANs, so in our model, the maximal conductance of the SPN M-current
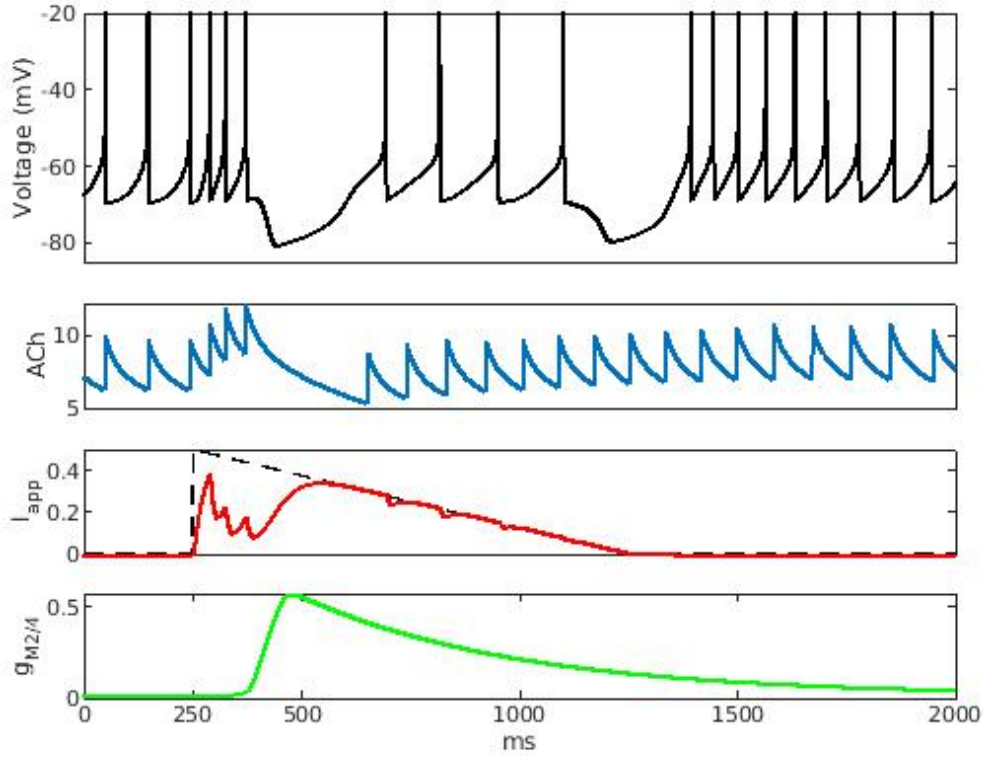
Figure 39: **A Failure Due to Premature Drive Removal.** If the duration of the ramp is halved to $t_f = t_0 + 1000$ ms, there is an initial TAN surge and pause before firing resumes. After input fades away, however, a second pause occurs.
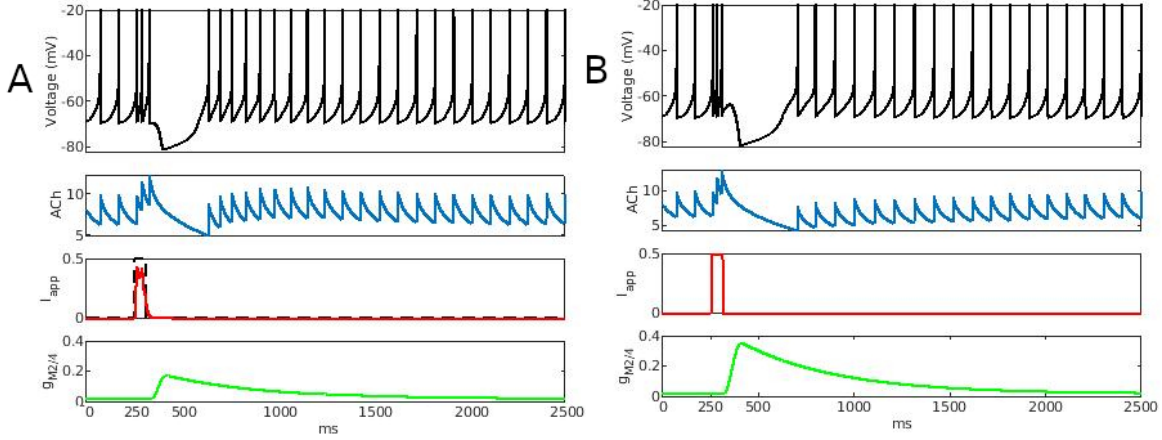
Figure 40: **Simulated TAN Response to Short Railcar Input Surge.** During the short railcar input, both ACh-sensitive **(A)** and ACh-insensitive **(B)** exhibit a single pause before returning to baseline. In the ACh-insensitive case, $g_{M2/4}$ (B, green) grows to levels more comparable with the ACh-sensitive responses in other input profiles

$g_{M1}$ decreases in the presence of ACh and rises in its absence (equation 8). In our simulations, as the TAN begins a surge in firing, ACh rises and suppresses $g_{M1}$. Thus, $I_{MS}$ is reduced, which enhances SPN firing above the level resulting from the input alone and contributes to the SPN surge. Once the TAN pauses, ACh decays below its baseline level, causing $A_S$, and therefore $g_{M1}$ and $I_{MS}$, to rise and to fight against SPN firing, potentially yielding the SPN pause. As TANs return to their baseline firing rate, ACh, and therefore $g_{M1}$, recovers to its baseline level as well. Figure 41 shows a typical ACh subsystem trace, generated by system (10) for a successful surge simulation.

We find that two of the four successful TAN response profiles generate successful SPN response traces (Fig 42A, B). For both the ACh-sensitive long railcar and the ACh-insensitive short railcar, the TAN pause allows significant ACh decay, resulting in a strong increase in $g_{M1}$, which can overcome any residual input to the SPN and induce a pause. On the other hand, the ACh-sensitive ramp input and ACh-sensitive short railcar input to the TAN both result in inappropriate SPN dynamics (Fig. 42C, D), regardless of the SPN input profile. For these cases, failure of the SPN surge-pause response occurs for two primary reasons: In

the ramp input profile, the decay of ACh during the TAN pause allows the effective input to the TAN ($I_{appT}$) to recover, shortening the duration of the pause. This shortened pause causes firing to resume, so ACh does not decay as deeply as in the successful cases, $g_{M1}$ does not grow much above its baseline level, and hence $I_M$ only weakly suppresses firing in SPN. Meanwhile, in both of these cases, TAN firing after the pause resumes at a slightly higher rate than in baseline conditions (Fig. 37B). As the TAN returns to tonic firing at this higher rate, ACh again rises above baseline, causing an increase in $g_{M1}$ and thereby *promoting* SPN firing again, leading to a prolonged surge of SPN spiking.

Thus, our simulations suggest that cortical and thalamic excitatory inputs to TANs and SPNs could lead to their experimentally observed surge-pause responses if those inputs are either an ACh-sensitive sustained (i.e,. adapting) input of long enough duration or a sufficiently brief ACh-insensitive (i.e., non-adapting) sustained input. Given that experiments have shown that input pathways from cortex and thalamus to TANs and SPNs do feature receptors known to be impacted by ACh, however, we predict that cortical and thalamic activity associated with motor tic production under bicuciline application is sustained and outlasts the observed TAN and SPN surges.

## 3.4    Discussion

We have constructed a conductance-based model of a striatal TAN that can produce various TAN spiking patterns observed experimentally and responds appropriately when tested under a wide range of conditions previously explored experimentally ([25], [84], [14], [64], [136], [69]). This model development represents an important step forward in efforts to simulate and model striatal activity, which may be of use in studying movement disorders. We find that ACh-sensitive M-current conductances that respond to varying ACh levels represent a viable mechanism for TAN autoregulation, which has long been believed to play a role in modulating striatal function ([145]; [50]). This cholinergic modulation has a strong effect when the TAN model is coupled with an SPN, contributing to the emergence of the surge-pause behavior associated with motor tics induced by bicuculline administration ([64]).
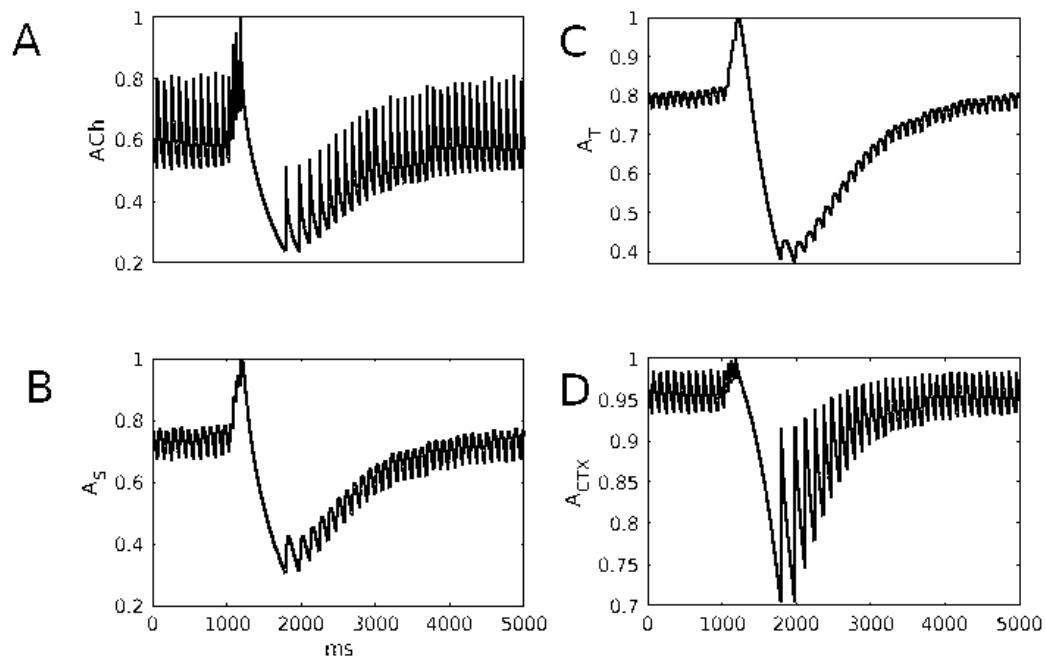
Figure 41: **ACh Engagment**. **A**: Normalized level of extracellular ACh in the case of ACh-sensitive railcar input of 250ms. Note the decay below baseline corresponding to the TAN pause. **B-D**: Normalized engagement of ACh in the various receptor types
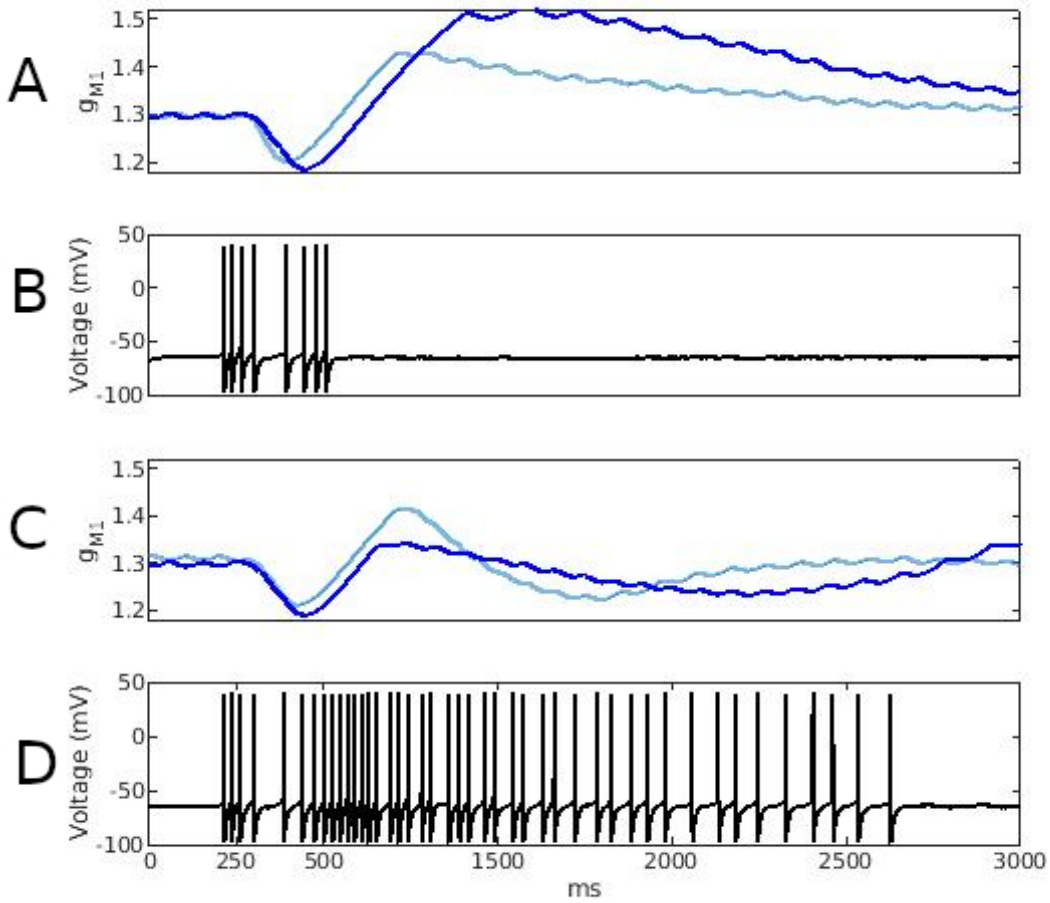
Figure 42: **SPN Dynamics. A:** In the ACh-sensitive railcar (blue) and combined input cases (orange, yellow), the initial buildup of ACh suppresses the conductance $g_{M1}$ of the SPN M-current during the TAN surge, inducing **B:** a corresponding surge in SPN spiking. As ACh decays, the SPN M-current conductance rises, suppressing further SPN firing. **C:** In the case of the ACh-sensitive ramp input, $g_{M1}$ does not grow as large and **D:** a sustained surge of SPN spiking results.

The contrast between the prolonged, accelerated firing of an individual TAN during depolarizing current injection and the pause in TAN activity following a firing surge associated with motor tic production, which leads to a corresponding rise in ACh, suggests that cholinergic feedback is vital for the latter. Because quantitative information about the effects of ACh on muscarinic receptors is sparse, we used a phenomenological approach to model the ACh subsystem; more precise modeling represents a natural future direction that can be pursued once further research into the specific actions of ACh has been conducted. However, the results that we have obtained provide constraints on the time course of cortical and thalamic inputs during motor tics. Specifically, our results suggest that inputs must be longer than the associated TAN and SPN surge duration and must be sensitive to ACh levels; for example, prolonged, sustained input should result in multi-phasic TAN responses, with multiple surge-pause epochs, while adapting input should result in other patterns that have not been observed experimentally ([64]). An important caveat to this work is that, lacking data on cortical and thalamic inputs to striatum during motor tic production, we explored several natural choices of input profiles; however, it is still possible that some more complicated pattern of inputs occurs and results in the surge-pause response, or that differences in cortical and thalamic input timing, which we have not considered, could contribute.

TANs exhibit a variety of firing modes ([84]), which we can reproduce with a single model. Capturing these different firing patterns does require some differences in model parameter settings. These differences likely reflect the biological reality; that is, the differences in activity observed experimentally when TTX is applied to TANs engaged in these behaviors indicates that the internal mechanisms of the cells truly are tuned differently across these regimes and hence the use of different parameter values to capture them is justified. Of particular note is the transition between the burst-pause regime and the tonic firing regime in the model, which we obtain with only a change to extracellular $K^+$ concentration. This concentration is believed to exhibit local variations in vivo ([23]; [139];, [52]). Interestingly, a diversity of firing modes is also found in certain neurons in other brain areas and may also be associated with differences in potassium conductances ([52]). The tonic firing mode appears to be the TAN activity pattern most commonly observed experimentally and gives the cell its name, so we make the natural choice of selecting it as a baseline condition for our

emulation of other experimental benchmarks. More work should be done in the future to consider how all of the different TAN firing modes impact TAN computation and what role they play in maintaining striatal function. Our model suggests a mechanism by which the TAN firing mode may be controlled experimentally, and may be of future use in examining TAN responses to different stimuli in non-tonic firing regimes.

While our approach shows that tuning of a small set of factors suffices to modulate firing patterns in an isolated TAN neuron, it is likely that TAN activity observed in experiments is influenced by the activity of a veritable zoo of other striatal cell types, many of which have ACh-sensitive nicotinic receptors ([31]; [141]). Although many of these are quite sparse within the striatum, these cells have recently been shown to play an important role in mediating TAN function (e.g., GABAergic NPY-NGF neurons studied in [47]; [96]). Dopamine is another important modulator of TAN behavior, which is widely believed to play an important role in the process of learning, particularly during TAN pauses ([16]; [59]; [68]; Tan and Bullock, 2008; Conceicao et al., 2017). Indeed, motor tics may be learned responses to corticothalamic surges (Conceicao et al., 2018), and the pause following TAN surges may contribute to this learning process. However, the DA-TAN interaction is complex and bi-directional and has not been implicated directly in the activity patterns that we have studied, and hence we have not modeled it in this work. More detailed models should also take into account the fact that SPNs are heterogenous, with direct pathway SPNs specifically expressing $M_4$ channels (Higley, Soler-Llavina and Sabatini, 2009; [20])

While other models of TANs exist ([84]; [71]; Tan and Bullock, 2018; [136]), we find that they are generally non-spiking models of subthreshold dynamics or otherwise unsuitable for exploring motor tic phenomena. To our knowledge, what we present here is the first spiking, conductance-based model of a TAN that reproduces at least qualitatively the variety of experimental benchmarks that we have considered. Although our model matches some experimental observations quantitatively, the timing of certain events in our simulations, especially during deep hyperpolarizations, is not fully consistent with experimental results. This is likely a result of using fixed membrane time constants. Allowing the membrane time constant of $I_h$ to vary with voltage could potentially alleviate these timing differences, as the deep hyperpolarizations in the model result from an interplay between $I_h$ and other

hyperpolarizing currents (e.g. $I_{IR}$). Furthermore, while the activity of our model depends on $I_M$, which is not completely inactive at hyperopolarized voltages, there may be additional subthreshold currents that we have not captured. Indeed, in the trapezoidal input experiment done by [136], as input is ramped down, the experimentally observed voltage is roughly linear, while the voltage trace of our model is concave (Fig. 32A,D). Finally, there is some subtlety missing in our representation of calcium-sensitive AHP currents. Both experimentally and in our model, an influx of calcium can cause the cell to transiently enter the burst-pause firing regime, but it is not clear from our simulations that calcium dynamics alone can sustain burst-pause firing. Moreover, our model requires some adjustment of parameter values to respond accurately to apamin, and even in the apamin-sensitive parameter regime produces hyperpolarizations slightly shallower than those seen experimentally. It may be possible to resolve these small discrepancies by using a different formulation of the sAHP current or tuning of the $[Ca^{2+}]$ subsystem.

Ultimately, we have developed a biologically constrained model of a TAN that fits a variety of experimental observations and have used it to explore how feedback effects associated with ACh contribute to TAN and SPN surge-pause responses to excitatory inputs, as may occur during motor tic production after bicuculline application. Incorporating this autoregulation into computational models including networks of striatal neurons may help to determine what, if any, functional roles different firing modes play in regulating striatal activity and whether GABAergic inhibition alone is enough to suppress the striatal activity associated with motor tics.

## 4.0   Chaos in Striatal Circuit with Sustained Drive

### 4.1   Introduction

Chaos, perhaps most famous from the butterfly effect, is often found in complex systems, especially those involving feedback loops. [41] Due to their unpredictable behavior, chaotic systems may appear at first glance to be random, they are in fact deterministic, and if an initial state can be known exactly, the full future of the trajectory can be computed, at least in principle [138]. While the brain is fundamentally noisy, chaotic and nearly chaotic systems are believed to govern the underlying activity of many neural circuits. [112] [132] [113] Whether or not this chaos is beneficial to the neural computation is of course dependent on context, but one useful effect of chaos is the ability to initiate state transitions when nearly chaotic circuits have multiple stable activity patterns. [49] When supplied adequate sustained input, the TAN model in the previous chapter exhibits some characteristics of chaotic behavior. The presence of interacting feedback loops is common in chaotic systems, so we wish to examine this behavior more carefully. In this chapter, then, we will discuss some routes to chaos and demonstrate them in a simplified TAN model.

### 4.2   Methods

#### 4.2.1   Reduced Model

In the interest of tractability, we consider a simplified TAN model which captures three key features of the full model during the transition to chaos: Periodic firing with no or low sustained input, chaotic firing without hyperpolarizations with moderate sustained input, and chaotic firing with hyperpolarizations with high sustained input. Since we no longer

consider firing modes or channel blocker responses, the model is greatly simplified to

$$\begin{aligned} C\tfrac{d}{dt}v &= -I_{Na} - I_K - I_{IR} - I_h - I_{leak} + I_{app} \\ \tau^* \tfrac{d}{dt}x^* &= x_\infty^* - x^* \end{aligned} \tag{11}$$

where all current equations are the same as the previous chapter. In addition to standard Na, K and leak currents, we retain only the sag, $I_h$ and inward rectifier $I_{IR}$, as well as cholinergic dynamics on the applied current, given by

$$\begin{aligned} \tfrac{d}{dt}A &= -\eta * A + \rho \exp(\tfrac{a-\theta_A}{\sigma_A})^{-1} - A^2/(A^2 + \alpha^2) + T \\ \tfrac{d}{dt}T &= A^2/(A^2 + \alpha^2) - T \\ \tau_{app}\tfrac{d}{dt}I_{app} &= M_{app}(1 + \exp((T - \theta_{app})/\sigma_{app}))^{-1} - I_{app} \end{aligned} \tag{12}$$

### 4.2.2 Key observations

With this simplified model, we may make some key observations. Between spikes, $T$ is much faster than $A$, and so remains near its nullcline. Since, between spikes, $T$ remains on its nullcline, it does not contribute to they dynamics of $A$, which now decays at a constant exponential rate, $A(t) = A(0) \exp(\eta t)$. Thus, between spikes, we can make the further simplification to the cholinergic subsystem:

$$\begin{aligned} C\tfrac{d}{dt}v &= -I_{Na} - I_K - I_{IR} - I_h - I_{leak} + I_{app} \\ \tau^* \tfrac{d}{dt}x^* &= x_\infty^* - x^* \\ \tfrac{d}{dt}A &= -\eta * A \\ \tau_{app}\tfrac{d}{dt}I_{app} &= M_{app}(1 + \exp((\tfrac{A^2}{A^2+\alpha^2} - \theta_{app})/\sigma_{app}))^{-1} - I_{app} \end{aligned} \tag{13}$$

During a spike, the release of ACh from TAN is steep, with a high half-activation, causing $A$ to behave approximately discretely during a spike - each spike increases $A$ by approximately 2.08. Finally, after each spike, $v$, $h$, and $n$ return to approximately the same values. See Figure 43.

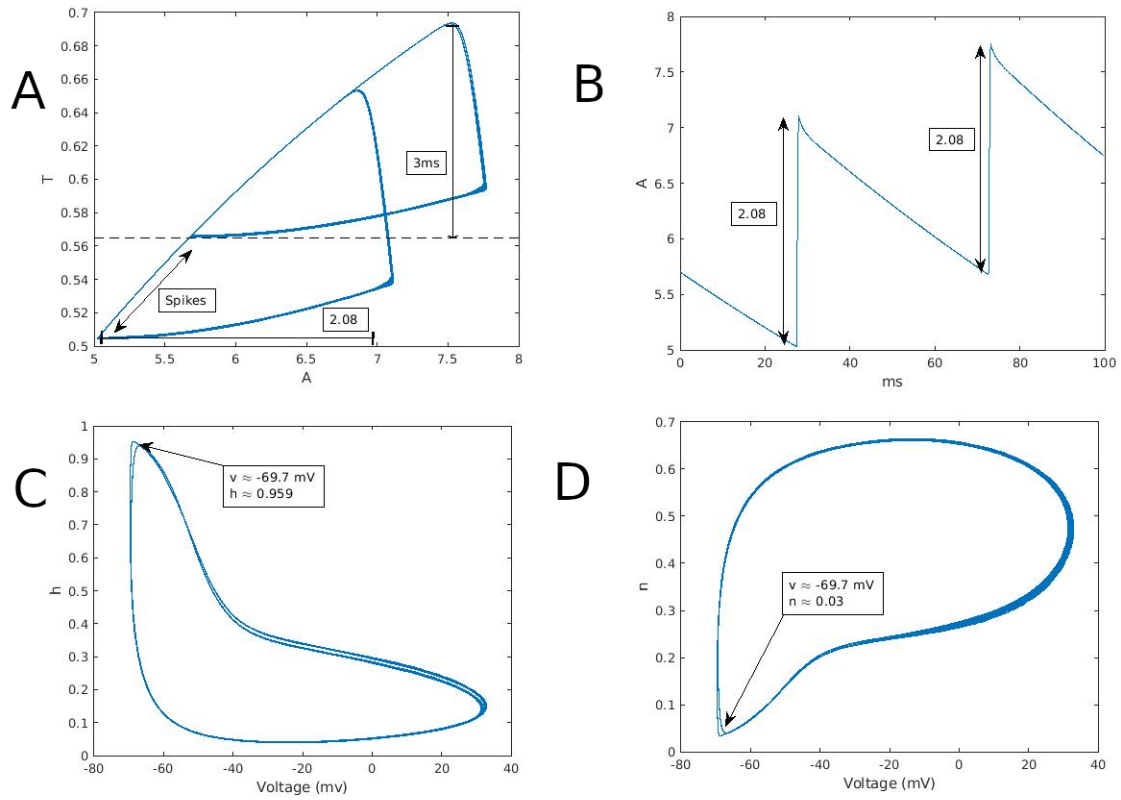Figure 43: **Key Observations in the Simplified TAN Model**. **A**: A-T projection during spiking. Notice that T quickly approaches its nullcline, and remains for the duration of the interspike period. **B**: A trace over 100 ms **C,D**: Projections of voltage with h (Na $^+$ inactivation) and n (K$^+$ activation), respectively. Notice that after each spike, all three return to the same approximate values.

### 4.2.3 Building the Poincare Map

With these considerations in mind, we can now define our approximate Poincare map $\mathbf{F}$

$$
\begin{aligned}
I_{n+1} &= I_{app}(t_f) \\
A_{n+1} &= A(t_f) \\
p_{n+1} &= p(t_f)
\end{aligned}
\tag{14}
$$

Where $I_{app}(t), A(t)$, and $p(t)$ are solutions to (13) with initial conditions $I_0 = I_n, A_0 = A_n + 2.08, p_0 = p_n$, and spike condition $t_f : v(t_f) = 20$. In the interest of computational efficiency, we approximate this map on a four dimensional grid (one for each of the dynamic variables, and one for the parameter $M_{app}$), and use fourth-order spline interpolation.

## 4.3 Results

### 4.3.1 Period Doubling Bifurcations

In the Poincare map $F$, a periodic limit cycle appears as a fixed point, $x^* = \mathbf{F}(x^*; \mu)$, where $\mu$ is some parameter [110] At these fixed points, the map intersects with the identity map $\mathbf{I}(x) = x$. An important bifurcation in these maps is the period doubling bifurcation, occurring at $\mu^*$. In this case, for $\mu < \mu^*$, we have some stable fixed point $x^* = \mathbf{F}(x^*; \mu)$, but if $\mu > \mu^*$, the fixed point loses stability and we have a new stable solution $\hat{x}$ such that $\hat{x} \neq \mathbf{F}(\hat{x})$ and $\hat{x} = \mathbf{F}^2(\hat{x})$. That is to say, applying the map $F$ to $\hat{x}$ takes us elsewhere, but applying it twice returns us to our starting value. It is easy to see that there must, in fact, be two points that satisfy this relationship, namely $\hat{x}$ and $\mathbf{F}(\hat{x})$.

Iterating (14) over a range of $M_{app}$ yields a bifurcation diagram exhibiting period doubling. (see Figure 49). We observe that the sequence period doubling bifurcations is increasingly frequent, suggesting an eventual chaotic regime. Returning to the flow, at these parameter values we additionally observe period doubling in the limit cycle of the model neuron (see Figs. 44,45)

Figure 44: **Single Period Limit Cycle. A:** Phase plane of $I_{app}$ vs. ACh. B: Phase plane of $I_{app}$ vs. sag gating variable p. C: Phase plane of receptor activation $A_{Ctx}$ vs. ACh. D: Voltage trace. Notice that each phase plane follows a single loop, and voltage is periodic.



Figure 45: **Period 2 Limit Cycle:** A: Phase plane of $I_{app}$ vs. ACh. B: Phase plane of $I_{app}$ vs. sag gating variable p. C: Phase plane of receptor activation $A_{Ctx}$ vs. ACh. D: Voltage trace. Notice that each phase plane follows a double loop, and voltage is doubly periodic.

103

Figure 46: **Period 4 Limit Cycle. A:** Phase plane of $I_{app}$ vs. ACh. B: Phase plane of $I_{app}$ vs. sag gating variable p. C: Phase plane of receptor activation $A_{Ctx}$ vs. ACh. D: Voltage trace. Though the difference is slight, each phase plane now follows four loops.

As we increase the parameter value, we continue to pass through a second period doubling (see Figures 46,47)

As we increase the parameter further, we pass through another period doubling, and here we should suspect that we indeed have a period doubling cascade. (see Figure 48)

To approach finding these fixed period doublings in a more principled manner, we perform stability analysis of the fixed points. For fixed points, they remain stable so long as all eigenvalues remain within the complex unit circle. While a loss of stability corresponding to eigenvalues which leave the unit circle through 1 or complex conjugates are similar to the case of flows, stability loss through an eigenvalue of $-1$ is not so straightforward, and indicates a period doubling bifurcation [55]. Thus, for a period 2 bifurcation, we find where an eigenvalue of $\mathbf{F}(x^*; \mu)$ reaches $-1$; for a period 4 bifurcation, we find where an eigenvalue of $\mathbf{F}^2(x^*; \mu)$ reaches $-1$; for a period 8 bifurcation, we track the eigenvalues of $\mathbf{F}^4(x^*; \mu)$ etc. We perform this analysis up to period 8, finding more precise estimates of the bifurcation, and compare to our bifurcation diagram. See Figures 49, 50 A-C.

Figure 47: **Another View of Period 4. A:** Phase plane of $I_{app}$ vs. ACh. B: Phase plane of $I_{app}$ vs. sag gating variable p. C: Phase plane of receptor activation $A_{Ctx}$ vs. ACh. D: Voltage trace. As $M_{app}$ is increased further, the 4-periodic nature is more clear.
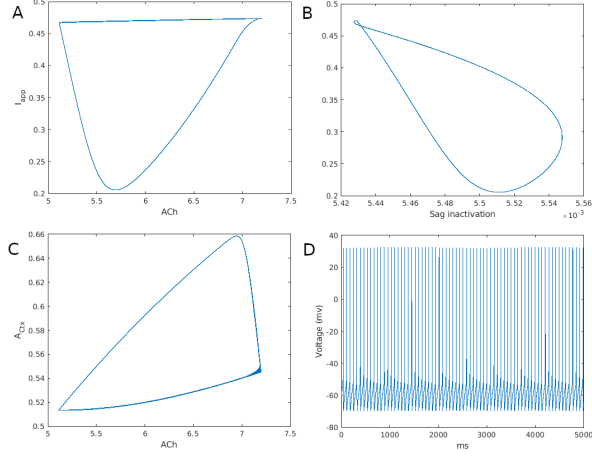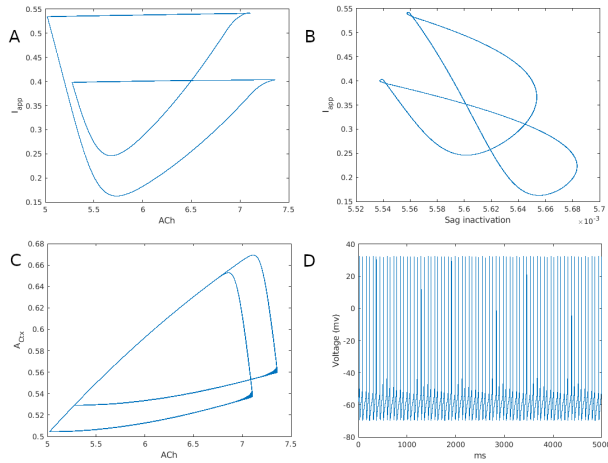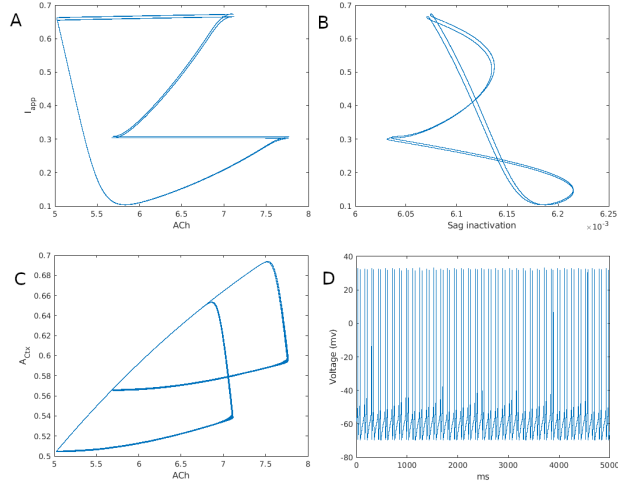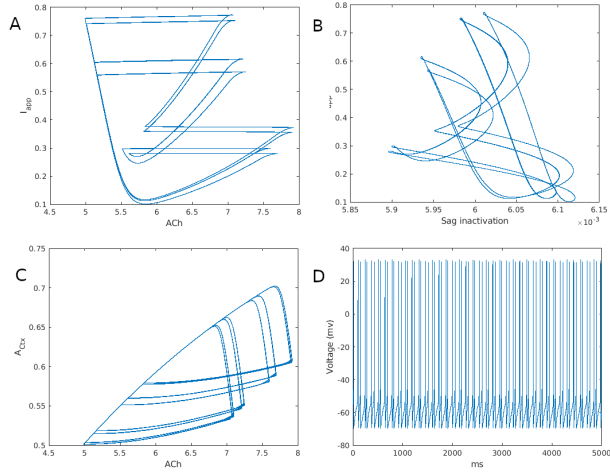


Figure 48: **Period 8 Limit Cycle: A:** Phase plane of $I_{app}$ vs. ACh. B: Phase plane of $I_{app}$ vs. sag gating variable p. C: Phase plane of receptor activation $A_{Ctx}$ vs. ACh. D: Voltage trace. After a period 8 doubling, chaos seems imminent. Notice, however, that $A_{Ctx}$ consistently remains near a 1-dimensional curve.
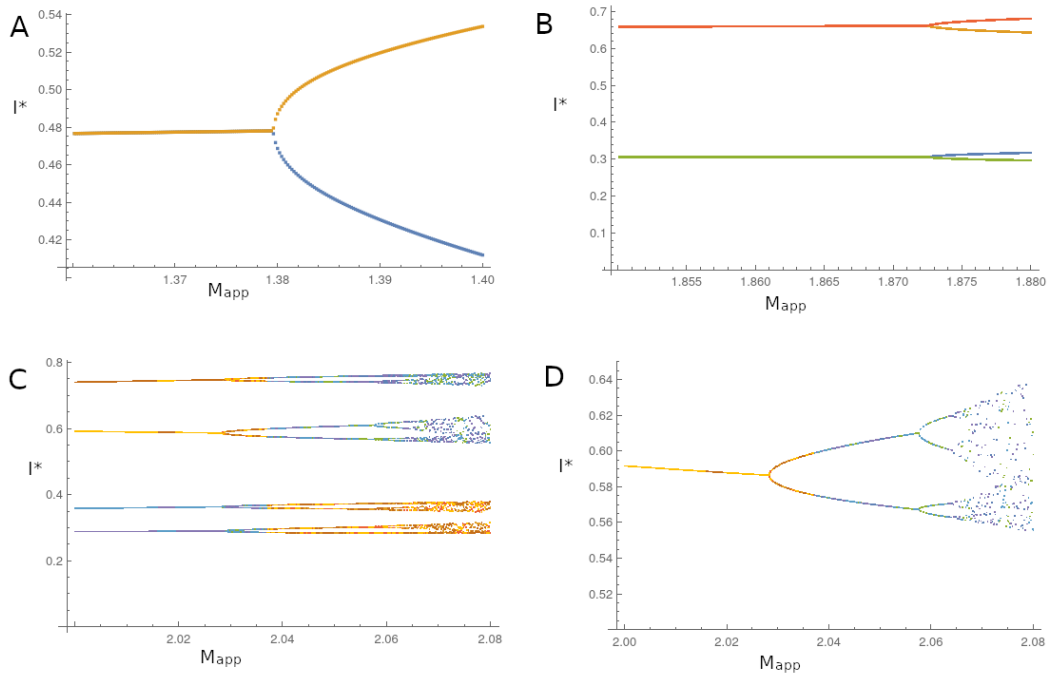
Figure 49: **Period Doubling Bifurcations**. **A:** close-up view of bifurcations from (A) period 1 to period 2, (B), period 2 to period 4, and (C) from period 4 to period 8. **D:** A closer view of period 8 doubling. Notice that a period 16 bifurcation is visible.

### 4.3.2 Lyapunov Exponents

While sequential period doubling bifurcations offer evidence of chaos, finding the exact sequence of parameters is impractical; showing this sequence has a finite limit even more so. Instead, we may turn to computing the maximal Lyapunov exponent of the map. This exponent describes the rate of divergence of two nearby initial points: that is, given two initial points $x_0$ and $x_0 + \epsilon$, after $N$ iterations of the map $\mathbf{F}$, we have $|\mathbf{F}^N(x_0) - \mathbf{F}^N(x_0 + \epsilon)| \approx \epsilon e^{N\sigma}$. Thus, if $\sigma < 0$, solutions converge exponentially, and if $\sigma > 0$, solutions diverge exponentially. For solutions which diverge, we are then in a chaotic system. To find the Lyapunov exponents of the map, we compute the eigenvalues of $\lim_{n \to \infty} (\prod_{i=0}^{n-1} D\mathbf{F}(x_i))^{\frac{1}{n}}$ with some sequence $x_i = \mathbf{F}^i(x_0)$ [55]. With these eigenvalues $\lambda_j$, our Lyapunov exponents are then $\sigma_j = \log(\lambda_j)$. We approximate these exponents with $n = 5000$, and find that our maximal Lyapunov exponent crosses 0 (and thus, the system becomes chaotic) when the parameter $M_{app} \approx 2.1$ (see Figure 50D.) We again return to the flow and find that the approximation agrees (see Figure 51).

### 4.3.3 Hyperpolarizations

When the cell fires rapidly, the sag current begins to inactivate. During normal firing, particularly when $I_{app}$ is low, the sag current is responsible for keeping the cell above the firing threshold. Thus, if $M_{app}$ is high enough, the cell begins to enter phases where the sag is sufficiently inactivated and $I_{app}$ is low, causing the voltage to make an excursion toward the K$^+$ reversal potential due to the influence of the inward rectifier. When $I_{app} + I_h \leq 0.4917$ the spiking oscillation is destroyed and the voltage approaches a stable fixed point. This excursion allows the sag current to recover and, due to the pause in firing, allows ACh to decay which in turn allows $I_{app}$ to rebound to much greater levels than before. When $I_{app} + I_h \geq 0.8543$, the fixed point is destroyed, and the cell resumes firing. This event can be seen in the full bifurcation diagram (Figure 53.) After the chaotic regime has begun, there is a sudden expansion in the range of $I^*$, indicating these large rebounds. Again, this agrees with the flow. (See Figure 52)
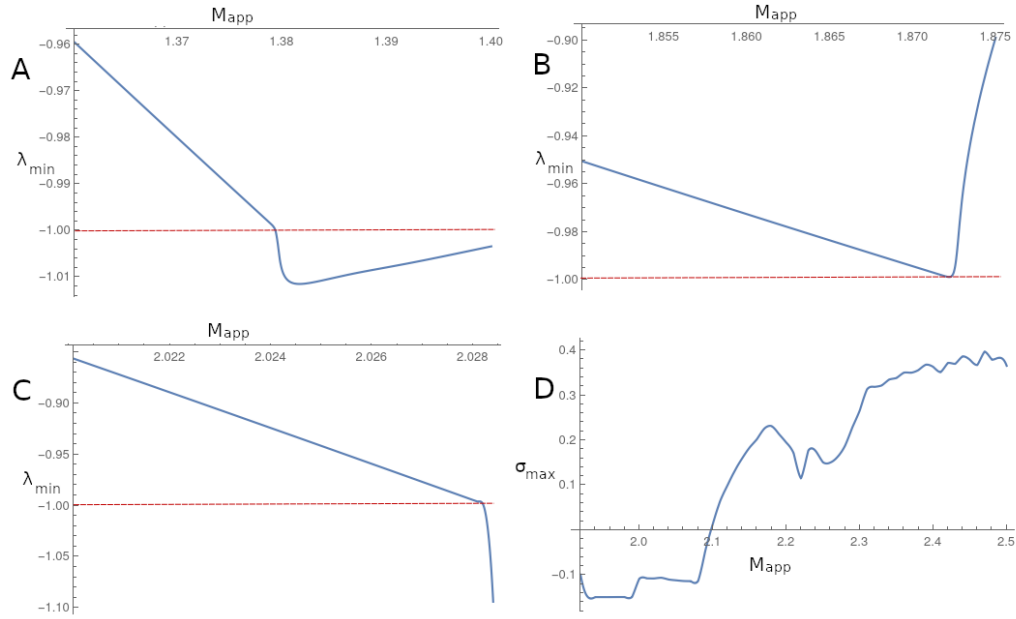
Figure 50: **Eigenvalues and Maxmial Lyapunov Exponent. A-C:** Eigenvalues of $\mathbf{F}$,$\mathbf{F}^2$, and $\mathbf{F}^4$, respectively. As they pass through -1, period doubling occurs. **D:** The maximal Lyapunov exponent as it crosses 0, indicating the onset of chaos.
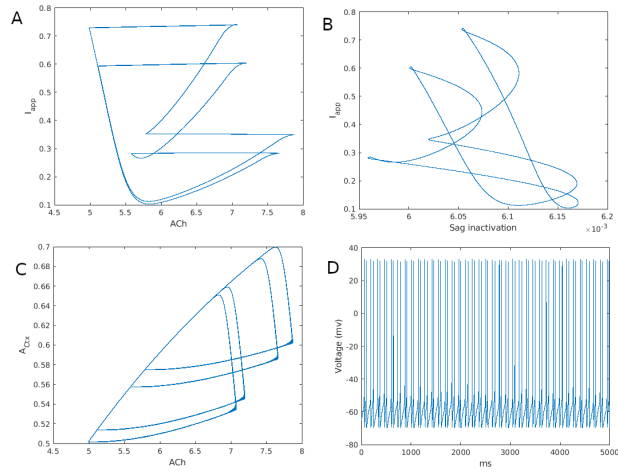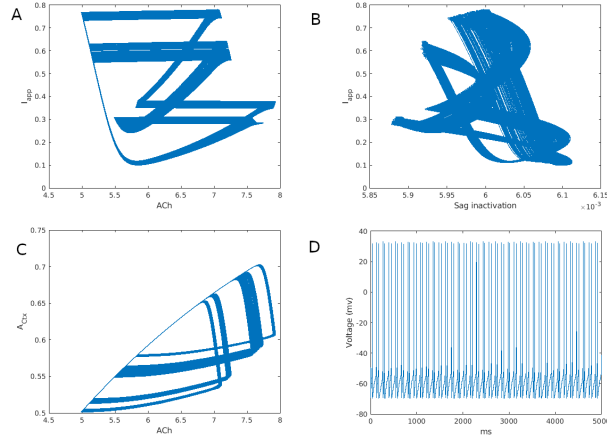
Figure 51: **Chaotic Regime. A:** Phase plane of $I_{app}$ vs. ACh. **B:** Phase plane of $I_{app}$ vs. sag gating variable p. **C:** Phase plane of receptor activation $A_{Ctx}$ vs. Ach. **D:** Voltage trace. After chaos begins, the trajectory creates a dense path, however, its behavior is still tightly bound. $A_{Ctx}$ remains near a 1-dimensional curve.
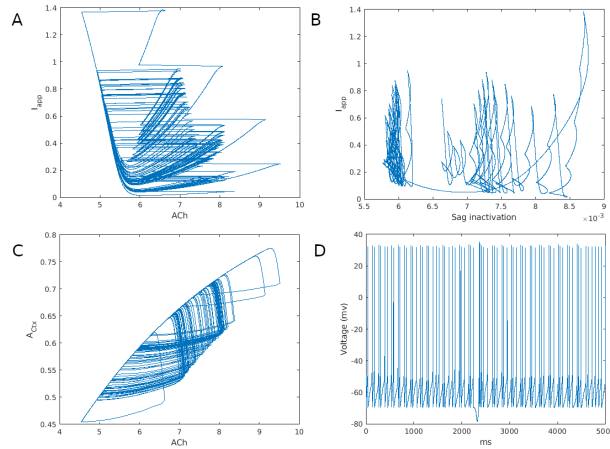


Figure 52: **Hyperpolarizations in the Chaotic Firing Regime. A:** Phase plane of $I_{app}$ vs. ACh. **B:** Phase plane of $I_{app}$ vs. sag gating variable p. **C:** Phase plane of receptor activation $A_{Ctx}$ vs. Ach. **D:** Voltage trace. When hyperpolarizations begin to occur, the range of activity of the neuron is greatly expanded. These hyperpolarizations allow $I_{app}$ and sag inactivation $p$ to much higher levels than before.
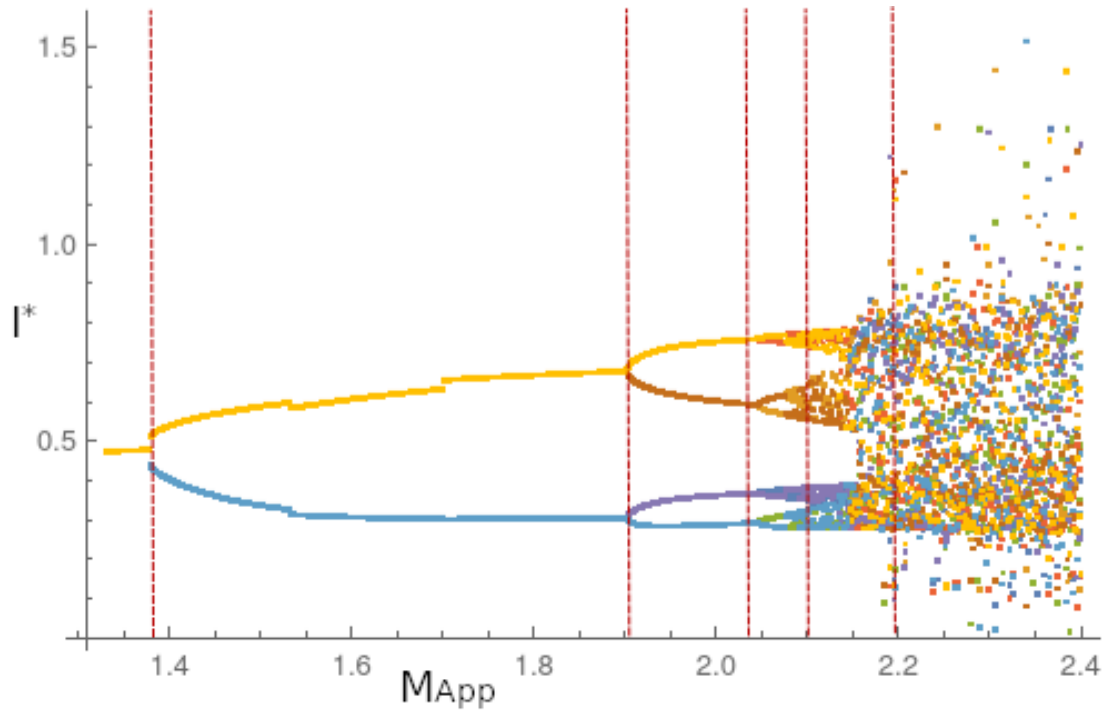
Figure 53: **The Full Bifurcation Diagram**. As the maximum current parameter $M_{app}$ increases, the system goes through a series of stable or periodic points, denoted $I^*$, before becoming chaotic. When $M_{app} \approx 2.2$, the range of $I$ expands, indicating the onset of hyperpolarization events. Some numerical error is present at this scale.

## 4.4 Discussion

It is unclear what role this chaotic firing may have in the striatum. One possibility is that, since TANs are weakly coupled via ACh, there is some risk of synchronization of firing, causing rhythmically varying levels of ACh throughout. This chaotic firing, then, can break synchronization, allowing the population to maintain a relatively steady level of ACh. On the other hand, by promoting sag inactivation, chaotic firing increases the propensity of TANs to hyperpolarize, which may lead to pauses. Since pauses contribute to learning, essentially randomly distributed pauses are likely to be detrimental to the normal function of the striatum. This apparent dichotomy may be partially resolved by different TAN firing modes. Periods of chaotic firing can be useful for transitioning between different stable patterns. When TANs are in bursting mode, the sag current is minimally inactivated, which may counteract the apparent promotion of pausing from the chaotic drive. It is important to reiterate here that pauses during burst firing are distinct from the TAN pause, which is longer, may occur during tonic firing, and is associated with learning events. Indeed, using chaotic firing to switch to burst firing may even allow TANs to coordinate pausing during these learning events. This aligns somewhat with other theories of chaos in neural systems, which suggest that the striatum should be on the edge of chaos: unstable enough to undergo lasting responses to brief signals, but not so unstable that these responses are too distinct [114]

At first glance, the construction of the Poincare map does not seem to offer much simplification: we are essentially integrating the same equations regardless. However, following this approach does in fact greatly simplify computations. We only need to integrate over one spike, and because the ACh is stereotyped during the spike, we can avoid computing the full action potential. More useful, however, is the fact that since the solutions of these integrals are continuous with respect to parameters and initial conditions, we can generate an interpolating surface of these solutions. Thus, we need only compute the integrals on an appropriately sized mesh, and from there iterating the map is merely computing polynomial values, which is computationally very efficient. Without more detailed numerical analysis, we do not know how the interpolation compares to the true surface, but comparisons to the

111

flow near the bifurcations suggest that our approximation is appropriate.

# 5.0 Conclusions

Throughout history, mathematics has been used to great effect to understand the natural world. Until recently, the sheer scale and complexity of neural circuits has prevented describing these structures and behaviors in a mathematically rigorous fashion. However, with the progress of technology, tools are becoming available to place these complex systems on a firm mathematical foundation, and this work represents some small inroads toward building a more complete theory of mathematical neuroscience.

We began by examining stick insect locomotion, during which each leg must be coordinated with the others to generate the walking pattern needed for movement as a whole, and within each leg, each joint must also coordinate with the others to generate correct individual steps. The stereotyped nature of these walking patterns allows us to focus on circuits of simple neurons specific to individual joints, and we focused on one of these joints. Since the neurons were simple, we could then further subdivide the problem into systems of planar ODEs. We found that except in the most ideal conditions, this circuit cannot track the duty cycle of a periodic forcing signal perfectly, but it can maintain the correct sequence of activity under a range of forcing conditions. This is achieved through modulation of a CPG which shares many important features of an HCO. Using high-performance computing, we were able to search parameter space across the entire circuit to find where the entrained solutions were stable and within a certain tolerance of the duty cycle of the forcing. Something not addressed by this work, and an open question for the future is the possible role of feedback from the CPG onto the forcing signal: the forcing is a result of ground contact, and the action of the joint impacts the timing of contact with the ground.

Next, we sought to examine a more detailed, realistic conductance-based model of striatal activity during motor tic production in animals treated with bicuculline. Although the animals are treated with bicuculline, the motor tics were consistent with human motor tics, so the behavior of this circuit may offer some insight into human pathologies, like Tourette's Syndrome. However, there were two major modelling challenges which first needed to be overcome: modelling of the TAN has not kept up with renewed experimental interest in TAN

behavior, and neuromodulators like ACh are commonly treated as static parameters, when we are specifically curious about the effects of transient dynamics. Although there are TAN models in the literature, they are often overly simplistic or overly restricted in their scope, modeling only one aspect of the myriad of behaviors TANs express. To remedy this, we began an extensive experimental literature review, identifying key features of normal TAN behavior, searching for evidence of relevant currents and how the cells respond to different experimental conditions. From this literature, we isolated a number of necessary currents required to express the full range of TAN behaviors, and could then tune our parameters so that the model matched TAN behavior under these different experimental conditions. Like the stick insect, this was made possible due to the fact that channel blockers could relatively isolate the response of individual currents, allowing us to tune the response of the model to these currents individually and combine these results into a single full model. The second modelling challenge to overcome was the action of ACh. Unlike the TAN itself, there is very little literature on the specific action of ACh, particularly the action of ACh on the receptors of interest. To work past this, we proposed a set of mechanistic interactions, similar to Lotka-Volterra and other population models. These give us, then, an at least reasonable model of the impact of these short, transient changes in the neuromodulator changes on the cells, and how they impact the cells' responses to drive. A particularly interesting feature of this model is the negative self-feedback loop of the TANs, where the release of ACh prevents TANs from firing, preventing the release of ACh, imposing some soft constraints on the firing rate of TANs.

Finally, we sought to examine how the TAN's feedback on its forcing signal impacted its behavior. Given a strong, continuous forcing signal that is subject to negative feedback due to ACh, the TAN response appears chaotic. With this observation, we then sought to quantify two things: is this system indeed truly chaotic, and, if so, by what mechanism does the cell transition from stable periodic firing to chaos. After simplifying the model to only its core elements, we found stereotyped behavior that allowed us to construct a Poincare map given through integral equations. This approach allowed us to drastically reduce the amount of computation necessary, as although the map equations were still too complex to be solved analytically, the entire behavior could be computed by integrating only a single spike

forward in time. Since these solutions are continuous in initial conditions and continuous in parameter space, we could then construct a mesh over which polynomial interpolation was used to further reduce computational complexity. We found a sequence of period doubling bifurcations, suggesting a period doubling cascade as a likely route to chaos. Rather than attempt to specify this sequence and find its accumulation point, we turned to the theory of Lyapunov exponents, and found that indeed the firing is truly chaotic.

This work has provided me with some insights into mathematical neuroscience, both generally as well as within the specific context of forcing. Speaking generally, although computers offer an extremely powerful tool for conducting research, they are not a substitute for mathematical insight and rigor. Even very simple circuits, of which there are trillions to study, can quickly grow into problems of immense complexity that computers are not capable of handling when approached naïvely. Mathematical solutions are completely necessary to cut through the scale of these problems and reduce complexity back to the realm of what is tractable and not merely possible in principle. Indeed, this type of approach is what allows us to study isolated forced circuits in the first place. As for forcing, it is important to realize that the response to the forcing need not match the timing of the forcing signal itself. Even in the case of the stick insect, where entrainment to the forcing signal is the goal, this is not always possible, much less necessary. Here, it is the sequence of the response matches rather than the specific timing, and so long as the sequence matches the insect can maintain its walking pattern. This seems plain in hindsight: the world is fundamentally rough and uneven, and maintaining fluid motion requires some level of redundancy and fault tolerance. We also see that even very short forcing signals can impart long-lasting effects to the circuit, as in the case of motor tics. While it would be incorrect to say that these long effects are necessarily pathological, very brief signals can dramatically alter the activity of a circuit. In multistable circuits, this may be an energetically efficient way to more permanently alter firing patterns. Whether or not this is a desirable outcome depends on the context. Regardless, this type of response will have considerable impact on neural computation.

# Bibliography

[1]     Borgmann A Hooper SL Büschges A. Sensory feedback induced by front-leg stepping entrains the activity of central pattern generators in caudal segments of the stick insect walking system. *Journal of Neuroscience*, 29: 2972–2983., 2009.

[2]     Borgmann A Scharstein H Büschges A. Intersegmental coordination: influence of a single walking leg on the neighboring segments in the stick insect walking system. *Journal of Neurophysiology*, 98: 1685–1696., 2007.

[3]     Borgmann A Toth TI Gruhn M Daun-Gruhn S Büschges A. Dominance of local load signals over inter-segmental effects in a motor system. i. experiments. *Biological Cybernetics*, 105(5-6): 399-411., 2011.

[4]     Büschges A. Role of local nonspiking interneurons in the generation of rhythmic motor activity in the stick insect. *J Neurobiol*, 27: 488–512., 1995.

[5]     Büschges A. Sensory control and organization of neural networks mediating coordination of multisegmental organs for locomotion. *J Neurophysiol*, 93: 1127–1135., 2005.

[6]     Büschges A. Connecting the micro with the macro level in motor control: unravelling general sensory influences on leg stepping. *J Physiol.*, (12):2971-2972., 2019.

[7]     Daun-Gruhn S Büschges A. From neuron to behavior: Dynamic equation-based prediction of biological processes in motor control. *Biological Cybernetics*, 105(1): 71-88., 2011.

[8]     Daun-Gruhn S Toth TI Borgmann A. Dominance of local load signals over inter-segmental effects in a motor system. ii. simulation studies. *Biological Cybernetics*, 105(5-6): 413-426., 2011.

[9]     Fuchs E Holmes P David I Ayali A. Proprioceptive feedback reinforces centrally generated stepping patterns in the cockroach. *J Exp Biol*, 215:1884–1891., 2012.

[10]    Hooper Sl Büschges A. *Neurobiology of Motor Control - Fundamental Concepts and New Directions.* Wiley Blackwell (SL Hooper & A Büschges eds.)., 2017.

[11] Hooper SL Guschlbauer Ch Blümel M Rosenbaum P Gruhn M Akay T Büschges A. Neural control of unloaded leg posture and leg swing in stick insect, cockroach and mouse differs from that in larger animals. *J Neurosci*, 29: 4109–4119., 2009.

[12] Prochazka A. *Proprioceptive feedback and movement regulation. In: Rowell l Sheperd JT (eds) Handbook of physiology*, volume 89–127. American Physiological Society New York:, 1996.

[13] Rosenbaum P Schmitz J Schmidt J Büschges A. Task-dependent modification of leg motor neuron synaptic input underlying changes in walking direction and walking speed. *Journal Neurophysiology*, 114: 1090-1101., 2015.

[14] Wilson C. J. Goldberg J. A. Origin of the slow afterhyperpolarization and slow rhythmic bursting in striatal cholinergic interneurons. *Journal of neurophysiology*, 95(1):196–204, 2006.

[15] Wosnitza A Bockemühl T Dübbert M Scholz H Büschges A. Inter-leg coordination in the control of walking speed in drosophila. *J Exp Biol*, 216: 480–491., 2013.

[16] Zhou F. M. Wilson C. J. Dani J. A. Cholinergic interneuron characteristics and nicotinic properties in the striatum. *Journal of neurobiology*, 53(4):590–605, 2002.

[17] Yeldesbay a Toth Ti Daun S. The role of phase shifts of sensory inputs in walking revealed by means of phase reduction. *Journal of Computational Neuroscience*, 44(1), 313-339., 2018.

[18] Biewener AA. Animal locomotion. *Oxford University Press Oxford.*, 2003.

[19] Eyad H Abed, HO Wang, and RC Chen. Stabilization of period doubling bifurcations and implications for control of chaos. *Physica D: Nonlinear Phenomena*, 70(1-2):154–164, 1994.

[20] Kreitzer A.C. Physiology and pharmacology of striatal neurons. *Annual Review of Neuroscience*, 32:127–147, 2009.

[21] Srivastava V Aminzare Z and Holmes. Gait transitions in a phase oscillator model of an insect central pattern generator. *SIAM Journal on Applied Dynamical Systems*, 17: 626-671., 2018.

[22]   Paul Apicella. The role of the intrinsic cholinergic system of the striatum: what have we learned from tan recordings in behaving animals? *Neuroscience*, 360:81–94, 2017.

[23]   Moghaddam B and Adams RN. Regional differences in resting extracellular potassium levels of rat brain. *Brain research*, 406(1-2):337–340, 1987.

[24]   B. D. Callaway J. C. Wilson C. J. Bennett. Intrinsic membrane properties underlying spontaneous tonic firing in neostriatal cholinergic interneurons. *Journal of Neuroscience*, 20(22):8493–8503, 2000.

[25]   Reynolds J.N.J. Hyland B.I. and Wickens J.R. Modulation of an afterhyperpolarization by the substantia nigra induces pauses in the tonic firing of striatal cholinergic interneurons. *Journal of Neuroscience*, 24(44):9870–9877, 2004.

[26]   Christian Bick, Marc Goodfellow, Carlo R Laing, and Erik A Martens. Understanding the dynamics of biological and neural oscillator networks through exact mean-field reductions: a review. *The Journal of Mathematical Neuroscience*, 10:1–43, 2020.

[27]   Büschges A. Bidaye SD Bockemühl T. Six-legged walking in insects: how cpgs peripheral feedback, and descending signals generate coordinated and adaptive motor rhythms. *J Neurophysiol*, 119: 459-475., 2018.

[28]   Bidaye SS Machacek C Wu Y Dickson BJ. Neuronal control of drosophila walking direction. *Science*, 344: 97–101., 2014.

[29]   Stefanos Boccaletti, Celso Grebogi, Y-C Lai, Hector Mancini, and Diego Maza. The control of chaos: theory and applications. *Physics reports*, 329(3):103–197, 2000.

[30]   Fellous J. M. Linster C. Computational models of neuromodulation. *Neural computation*, 10(4):771–805, 1998.

[31]   Orth M. Amann B. Robertson M. M. Rothwell J. C. Excitability of motor cortex inhibitory circuits in tourette syndrome before and after single dose nicotine. *Brain*, 128(6):1292–1300, 2005.

[32]   Pogorelov V. Xu M. Smith H. R. Buchanan G. F. Pittenger C. Corticostriatal interactions in the generation of tic-like behaviors after local striatal disinhibition. *Experimental neurology*, 265:122–128, 2015.

[33] Zhang c Lewis T. Phase response properties of half-center oscillators. *Journal of computational neuroscience*, 35:55-74., 2013.

[34] Graham D. An analysis of walking in the first instar and adult stick insect carausius morosus. *J. Comp. Physiol.*, 81:23–52., 1972.

[35] Graham D. Influence of coxa-thorax joint receptors on retractor motor output during walking in carausius morosus. *J Exp Biol*, 114: 131–139., 1985.

[36] Kreitzer A. C. Berke J. D. Investigating striatal function through cell-type-specific manipulations. *Neuroscience*, 198:19–26, 2011.

[37] Marder E Bucher D. Central pattern generators and the control of rhythmic movements. *Curr Biol*, 11: R986–R996., 2001.

[38] Rubin J Terman D. *Geometric singular perturbation analysis of neuronal dynamics. In: Handbook of dynamical systems B. Fiedler (ed.)*, volume 2: 93-146. Elsevier., 2002.

[39] Somers d Kopell N. Rapid synchronization through fast threshold modulation. *Biological cybernetics*, 68:393-407., 1993.

[40] Rybak I. Daun S Rubin J. Control of oscillation periods and phase durations in half-center central pattern generators: a comparative mechanistic analysis. *Journal of Computational Neuroscience*, 27(1): 3-36., 2009.

[41] JC Bastos de Figueiredo, L Diambra, Leon Glass, and CP Malta. Chaos in two-loop negative feedback systems. *Physical Review E*, 65(5):051905, 2002.

[42] P. J. ... Surmeier D. J. Ding J. Guzman J. N. Tkatch T. Chen S. Goldberg J. A. Ebert. Rgs4-dependent attenuation of m 4 autoreceptor function in striatal cholinergic interneurons following dopamine depletion. *Nature neuroscience*, 9(6):832–842, 2006.

[43] Giocomo L. M. Hasselmo M. E. Neuromodulation by glutamate and acetylcholine can change circuit dynamics by regulating the relative influence of afferent input and excitatory feedback. *Molecular neurobiology*, 36(2):184–200, 2007.

[44] Pakhotin P. Bracci E. Cholinergic interneurons control the excitatory input to the striatum. *Journal of Neuroscience*, 27(2):391–400, 2007.

[45]    Skinner F Kopell N Marder E. Mechanisms for oscillation and frequency control in reciprocally inhibitory model neural networks. *Journal of Computational Neuroscience*, 1:69–87., 1994.

[46]    Pearson KG. Ekeberg Ö. Computer simulation of stepping in the hind legs of the cat: an examination of the mechanisms regulating the stance-to-swing transition. *J Neurophysiol*, 94:4256–4268., 2005.

[47]    E. Tecuapetla F. Buzsáki G. Deisseroth K. ... Koos T. English D. F. Ibanez-Sandoval O. Stark. Gabaergic circuits mediate the reinforcement-related signals of striatal cholinergic interneurons. *Nature neuroscience*, 15(1):123, 2012.

[48]    G Bard Ermentrout and David H Terman. *Mathematical Foundations of Neuroscience.* Springer, 2010.

[49]    Walter J Freeman. Chaos in the brain: Possible roles in biological intelligence. *International Journal of Intelligent Systems*, 10(1):71–88, 1995.

[50]    Calabresi P. Centonze D. Gubellini P. Pisani A. Bernardi G. Acetylcholine-mediated modulation of striatal function. *Trends in neurosciences*, 23(3):120–126, 2000.

[51]    Wendler G. The co-ordination of walking movements in arthropods. *Symp Soc Exp Biol*, 20: 229–249., 1966.

[52]    Hemond P Epstein D Boley A Migliore M Ascoli GA and Jaffe DB. Distinct classes of pyramidal cells exhibit mutually exclusive firing patterns in hippocampal area ca3b. *Hippocampus*, 18(4):411–424, 2008.

[53]    Hughes GM. The co-ordination of insect movements. *J Exp Biol*, 29: 267–285., 1952.

[54]    Ann M Graybiel. Neurotransmitters and neuromodulators in the basal ganglia. *Trends in neurosciences*, 13(7):244–254, 1990.

[55]    John Guckenheimer and Philip Holmes. *Nonlinear Oscillations, Dynamical Systems, and Bifurcations of Vector Fields.* Springer, 1986.

[56]    John Guckenheimer and Ricardo A Oliva. Chaos in the hodgkin–huxley model. *SIAM Journal on Applied Dynamical Systems*, 1(1):105–114, 2002.

[57]    Boris Gutkin, David Pinto, and Bard Ermentrout. Mathematical neuroscience: from neurons to circuits to systems. *Journal of Physiology-Paris*, 97(2-3):209–219, 2003.

[58]    Cruse H. What mechanisms coordinate leg movement in walking arthropods. *TINS*, 13: 15–21., 1990.

[59]    Morris G. Arkadir D. Nevet A. Vaadia E. Bergman H. Coincident but distinct messages of midbrain dopamine and striatal tonically active neurons. *Neuron*, 43(1):133–143, 2004.

[60]    Schilling M Cruse H. Decentralized control of insect walking: A simple neural network explains a wide range of behavioral and neurophysiological results. *PLoS computational biology.*, 16(4):e1007804., 2020.

[61]    Mentel T Weiler V Büschges A Pflüger H-J. Activity of neuromodulatory neurones during stepping of a single insect leg. *J Insect Physiol*, 54(1): 51-61., 2008.

[62]    Stolz T Diesner M Neupert S Hess ME Delgado-Betancourt E Pflüger H-J and Schmidt J. Descending octopaminergic neurons modulate sensory evoked activity of thoracic motor neurons in stick insects. *J Neurophysiol*, 122: 2388-2413., 2019.

[63]    PJ Holmes and DA Rand. Bifurcations of the forced van der pol oscillator. *Quarterly of Applied Mathematics*, 35(4):495–509, 1978.

[64]    Bronfeld M. Belelovsky K. Bar-Gad I. Spatial and temporal properties of tic-related neuronal activity in the cortico-basal ganglia loop. *Journal of Neuroscience*, 31(24):8713–8721, 2011.

[65]    McCairn K. W. Bronfeld M. Belelovsky K. Bar-Gad I. The neurophysiological correlates of motor tics following focal striatal disinhibition. *Brain*, 132(8):2125–2138, 2009.

[66]    Danner SM Shevtsova NA Frigon A Rybak IA. Computational modeling of spinal circuits controlling limb coordination and gaits in quadrupeds. *eLife*, 6: e31050., 2017.

[67]    Eugene M Izhikevich and Richard FitzHugh. Fitzhugh-nagumo model. *Scholarpedia*, 1(9):1349, 2006.

[68]   Ashby F. G. Crossley M. J. A computational model of how cholinergic interneurons protect striatal-dependent learning. *Journal of Cognitive Neuroscience*, 23(6):1549–1566, 2011.

[69]   Choi S. J. Ma T. C. Ding Y. Cheung T. Joshi N. Sulzer D. ... Kang U. J. Alterations in the intrinsic properties of striatal cholinergic interneurons after dopamine lesion and chronic l-dopa. *Elife*, 9:e56920, 2020.

[70]   Ding J. B. Guzman J. N. Peterson J. D. Goldberg J. A. Surmeier D. J. Thalamic gating of corticostriatal signaling by cholinergic interneurons. *Neuron*, 67(2):294–307, 2010.

[71]   Franklin N. T. Frank M. J. A cholinergic feedback circuit to regulate striatal population uncertainty and optimize reinforcement learning. *Elife*, 4:e12029, 2015.

[72]   Goldberg J. A. Reynolds J. N. J. Spontaneous firing and evoked pauses in the tonically active cholinergic interneurons of the striatum. *Neuroscience*, 198:27–43, 2011.

[73]   Goldberg J. A. Teagarden M. A. Foehring R. C. Wilson C. J. Nonequilibrium calcium dynamics regulate the autonomous firing pattern of rat striatal cholinergic interneurons. *Journal of Neuroscience*, 29(26):8396–8407, 2009.

[74]   Goldberg J. A. Wilson C. J. Control of spontaneous firing patterns by the selective coupling of calcium currents to calcium-activated potassium currents in striatal cholinergic interneurons. *Journal of Neuroscience*, 25(44):10230–10238, 2005.

[75]   Holmes PJ Full RJ Koditschek D Guckenheimer J. The dynamics of legged locomtion: models analysis and challenges. *SIAM Rev*, 48(2):207–304., 2006.

[76]   Howe A. R. Surmeier D. J. Muscarinic receptors modulate n-, p-, and l-type ca2+ currents in rat striatal neurons through parallel pathways. *Journal of Neuroscience*, 15(1):458–469, 1995.

[77]   Maurice N. Mercer J. Chan C. S. Hernandez-Lopez S. Held J. Tkatch T. Surmeier D. J. D2 dopamine receptor-mediated modulation of voltage-dependent na+ channels reduces autonomous activity in striatal cholinergic interneurons. *Journal of Neuroscience*, 24(46):10289–10301, 2004.

[78]  Nisenbaum E. S. Wilson C. J. Foehring R. C. Surmeier D. J. Isolation and characterization of a persistent potassium current in neostriatal neurons. *Journal of neurophysiology*, 76(2):1180–1194, 1996.

[79]  Pisani A. Bernardi G. Ding J. Surmeier D. J. Re-emergence of striatal cholinergic interneurons in movement disorders. *Trends in neurosciences*, 30(10):545–553, 2007.

[80]  Shen W. Hamilton S. E. Nathanson N. M. Surmeier D. J. Cholinergic suppression of kcnq channel currents enhances excitability of striatal medium spiny neurons. *Journal of Neuroscience*, 25(32):7449–7458, 2005.

[81]  Song W. J. Tkatch T. Baranauskas G. Ichinohe N. Kitai S. T. Surmeier D. J. Somatodendritic depolarization-activated potassium currents in rat neostriatal cholinergic interneurons are predominantly of the a type and attributable to coexpression of kv4. 2 and kv4. 1 subunits. *Journal of Neuroscience*, 18(9):3124–3137, 1998.

[82]  Stiefel K. M. Gutkin B. S. Sejnowski T. J. Cholinergic neuromodulation changes phase response curve shape and type in cortical pyramidal neurons. *PLoS one*, 3(12):e3947, 2008.

[83]  Wang X Rinzel J. Alternating and synchronous rhythms in reciprocally inhibitory model neurons. *Neural Computation*, 4:84–97., 1992.

[84]  Wilson C. J. The mechanism of intrinsic amplification of hyperpolarizations and spontaneous bursting in striatal cholinergic interneurons. *Neuron*, 45(4):575–585, 2005.

[85]  Zhang W. Basile A. S. Gomeza J. Volpicelli L. A. Levey A. I. Wess J. Characterization of central inhibitory muscarinic autoreceptors by the use of muscarinic acetylcholine receptor knock-out mice. *Journal of Neuroscience*, 22(5):1709–1717, 2002.

[86]  Corbit V.L. Whalen T.C. Zitelli K.T. Crilly S.Y. Rubin J.E. and Gittis A.H. Pallidostriatal projections promote $\beta$ oscillations in a dopamine-depleted biophysical network model. *J. Neuroscience*, 36(20):5556–5571, 2016.

[87]  Smith JC Abdala APL Borgmann A Rybak IA Paton JFR. Brainstem respiratory networks: building blocks and microcircuits. *Trends Neurosci*, 36: 152–162., 2013.

[88]  Witten I. B. Lin S. C. Brodsky M. Prakash R. Diester I. Anikeeva P. ... Deisseroth K. Cholinergic interneurons control local circuit activity and cocaine conditioning. *science*, 330(6011):1677–1681, 2010.

[89] W. H. Todorov D. I. Latash E. M. ... Molkov Y. I. Kim T. Capps R. A. Hamade K. C. Barnett. The functional role of striatal cholinergic interneurons in reinforcement learning from computational perspective. *Frontiers in neural circuits*, 13(10), 2019.

[90] Stephen J Kish, Kathleen Shannak, and Oleh Hornykiewicz. Uneven pattern of dopamine loss in the striatum of patients with idiopathic parkinson's disease. *New England Journal of Medicine*, 318(14):876–880, 1988.

[91] K. Roberts E. A. Bucklin M. McCarthy M. M. Kopell N. Han X. Kondabolu. Striatal cholinergic interneurons generate beta and gamma oscillations in the corticostriatal circuit and produce motor deficits. *Proceedings of the National Academy of Sciences*, 113(22):E3159–E3168, 2016.

[92] Yoshiki Kuramoto. *Chemical oscillations, waves, and turbulence.* Courier Corporation, 2003.

[93] Marieke Langen, Dienke Bos, Siri DS Noordermeer, Hilde Nederveen, Herman van Engeland, and Sarah Durston. Changes in the development of striatum are involved in repetitive behavior in autism. *Biological psychiatry*, 76(5):405–411, 2014.

[94] Alun L Lloyd. The coupled logistic map: a simple model for the effects of spatial heterogeneity on population dynamics. *Journal of Theoretical Biology*, 173(3):217–230, 1995.

[95] Ruth Luthi-Carter, Andrew Strand, Nikki L Peters, Steven M Solano, Zane R Hollingsworth, Anil S Menon, Ariel S Frey, Boris S Spektor, Ellen B Penney, Gabriele Schilling, et al. Decreased expression of striatal signaling genes in a mouse model of huntington's disease. *Human molecular genetics*, 9(9):1259–1271, 2000.

[96] Assous M. Kaminer J. Shah F. Garg A. Koós T. Tepper J. M. Differential processing of thalamic information via distinct striatal interneuron circuits. *Nature communications*, 8(1):1–14, 2017.

[97] Büschges A Gruhn M. Mechanosensory feedback in walking: from joint control to locomotory patterns. *Advances in Insect Physiology*, 34: 194-234., 2008.

[98] Fink C. G. Booth V. Zochowski M. Cellularly-driven differences in network synchronization propensity are differentially modulated by firing frequency. *PLoS computational biology*, 7(5):e1002062, 2011.

[99]  Krishnan G. P. Chauvette S. Shamie I. Soltani S. Timofeev I. Cash S. S. ... Bazhenov M. Cellular and neurochemical basis of sleep stages in the thalamocortical network. *Elife*, 5:e18607, 2016.

[100]  Gruhn m Zehl l Büschges A. Straight walking and turning on the slippery surface. *J Exp Biol*, 212: 194-209., 2009.

[101]  Tiago V Maia and Michael J Frank. From reinforcement learning models to psychiatric and neurological disorders. *Nature neuroscience*, 14(2):154–162, 2011.

[102]  Büschges A Mantziaris C Bockemühl T. Central pattern generating networks in insect locomotion. *Dev Neurobiol.*, 80(1-2):16-30., 2020.

[103]  Jeffrey H Meyer, Stephanie Krüger, Alan A Wilson, Bruce K Christensen, Verdell S Goulding, Ayal Schaffer, Candace Minifie, Sylvain Houle, Doug Hussey, and Sidney H Kennedy. Lower dopamine transporter binding potential in striatum during depression. *Neuroreport*, 12(18):4121–4125, 2001.

[104]  Yaroslav I Molkov, Ana PL Abdala, Bartholomew J Bacak, Jeffrey C Smith, Julian FR Paton, and Ilya A Rybak. Late-expiratory activity: emergence and interactions with the respiratory cpg. *Journal of neurophysiology*, 104(5):2713–2729, 2010.

[105]  Moehle M.S. and Conn P.J. Roles of the m4 acetylcholine receptor in the basal ganglia and the treatment of movement disorders. *Movement Disorders*, 34(8):1089–1099, 2019.

[106]  Dolezal V. Wecker L. Y. N. N. Muscarinic receptor blockade increases basal acetylcholine release from striatal slices. *Journal of Pharmacology and Experimental Therapeutics*, 252(2):739–743, 1990.

[107]  McCarthy M. M. Brown E. N. Kopell N. Potential network mechanisms mediating electroencephalographic beta rhythm changes during propofol-induced paradoxical excitation. *Journal of Neuroscience*, 28(50):13488–13504, 2008.

[108]  McCarthy M. M. Moore-Kochlacs C. Gu X. Boyden E. S. Han X. Kopell N. Striatal origin of the pathologic beta oscillations in parkinson's disease. *Proceedings of the National Academy of Sciences*, 108(28):11620–11625, 2011.

[109] Ayali A Borgmann A Büschges A Couzin-Fuchs E Daun-Gruhn S Holmes P. The comparative investigation of the stick insect and cockroach models in the study of insect locomotion. *Current Opinion in Insect Science*, 12: 1-10., 2015.

[110] Lawrence Perko. *Differential Equations and Dynamical Systems*. Springer, 2000.

[111] Friedrich Pfeiffer, H-J Weidemann, and P Danowski. Dynamics of the walking stick insect. *IEEE Control Systems Magazine*, 11(2):9–13, 1991.

[112] Jan Pieter Pijn, Jan Van Neerven, Andre Noest, and Fernando H Lopes da Silva. Chaos or noise in eeg signals; dependence on state and brain site. *Electroencephalography and clinical Neurophysiology*, 79(5):371–381, 1991.

[113] Adam Ponzi and Jeff Wickens. Sequentially switching cell assemblies in random inhibitory networks of spiking neurons in the striatum. *Journal of Neuroscience*, 30(17):5894–5911, 2010.

[114] Adam Ponzi and Jeffery R Wickens. The inhibitory network of the striatum at the edge of chaos. *BMC Neuroscience*, 14(1):1–2, 2013.

[115] Ghigliazza r Holmes P. A minimal model of a central pattern generator and motoneurons for insect locomotion. *SIAM Journal on Applied Dynamical Systems*, 3:671-700., 2004.

[116] Bender JA Simpson EM Tietz BR Daltorio KA Quinn RD Ritzmann RE. Kinematic and behavioral evidence for a distinction between trotting and ambling gaits in the cockroach blaberus discoidalis. *J Exp Biol*, 214: 2057–2064., 2011.

[117] Marder E Calabrese RL. Principles of rhythmic motor pattern generation. *Physiol Rev*, 76: 687–717., 1996.

[118] Mendes CS Bartos I Akay T Márka S Mann RS. Quantification of gait parameters in freely walking wild type and sensory deprived drosophila melanogaster. *Elife*, 2:e00231., 2013.

[119] Daun-Gruhn S. A mathematical modeling study of inter-segmental coordination during stick insect walking. *Journal of Computational Neuroscience*, 30(2): 255-278., 2011.

[120] Gabel L. A. Nisenbaum E. S. Muscarinic receptors differentially modulate the persistent potassium current in striatal spiny projection neurons. *Journal of neurophysiology*, 81(3):1418–1423, 1999.

[121] Grabowska M Godlewska E Schmidt J Daun-Gruhn S. Quadrupedal gaits in hexapod animals—inter-leg coordination in free-walking adult stick insects. *J Exp Biol*, 215: 4255–4266., 2012.

[122] Knops S Toth TI Guschlbauer C Gruhn M Daun-Gruhn S. A neuromechanical model for curve walking in the stick insect. *J Neurophysiol*, 109(3): 679-691., 2013.

[123] McKinley J. W. Shi Z. Kawikova I. Hur M. Bamford I. J. Devi S. P. S. ... Bamford N. S. Dopamine deficiency reduces striatal cholinergic interneuron function in models of parkinson's disease. *Neuron*, 103(6):1056–1072, 2019.

[124] Orlovsky GN Deliagina TG Grillner S. Neuronal control of locomotion. *Oxford: Oxford University Press.*, 1999.

[125] Toth TI Daun S. A kinematic model of stick insect walking. *Physiological Reports*, 7(8): e14080., 2019.

[126] Toth TI Daun-Gruhn S. A putative neuronal network controlling the activity of the leg motoneurons of the stick insect. *NeuroReport*, 22(18): 943-946., 2011.

[127] Toth TI Grabowska M Schmidt J Büschges A Daun-Gruhn S. A neuro-mechanical model explaining the physiological role of fast and slow muscle fibres at stop and start of stepping of an insect leg. *PLOS ONE*, 8(11): e78246., 2013.

[128] Tóth TI Grabowska M Rosjat N Hellekes K Borgmann A Daun-Gruhn S. Investigating inter-segmental connections between thoracic ganglia in the stick insect by means of experimental and simulated phase response curves. *Biological Cybernetics*, 109(3): 349-362., 2015.

[129] Toth TI Knops s Daun-Gruhn S. A neuro-mechanical model explaining forward and backward stepping in the stick insect. *J Neurophysiol*, 107(12): 3267-80., 2012.

[130] Sponberg s Full RJ. Neuromechanical response of muscoskeletal structures in cockroaches during rapid running on rough terrain. *J Exp Biol*, 211:446., 2008.

[131] Partha Saha and Steven H Strogatz. The birth of period three. *Mathematics Magazine*, 68(1):42–47, 1995.

[132] Steven J Schiff, Kristin Jerger, Duc H Duong, Taeun Chang, Mark L Spano, and William L Ditto. Controlling chaos in the brain. *Nature*, 370(6491):615–620, 1994.

[133] Allen I Selverston. Invertebrate central pattern generator circuits. *Philosophical Transactions of the Royal Society B: Biological Sciences*, 365(1551):2329–2345, 2010.

[134] Andrew A Sharp, FRANCES K Skinner, and EVE Marder. Mechanisms of oscillation in dynamic clamp constructed two-cell half-center circuits. *Journal of neurophysiology*, 76(2):867–883, 1996.

[135] Harvey S Singer, In-Hei Hahn, and Timothy H Moran. Abnormal dopamine uptake sites in postmortem striatum from patients with tourette's syndrome. *Annals of Neurology: Official Journal of the American Neurological Association and the Child Neurology Society*, 30(4):558–562, 1991.

[136] Zhang YF Reynolds JN Cragg SJ. Pauses in cholinergic interneuron activity are driven by excitatory input and delayed rectification with dopamine modulation. *Neuron*, 98(5):918–925, 2018.

[137] Katz PS Hooper SL. *Invertebrate central pattern generators. In: Invertebrate Neurobiology edited by North g Greenspan RJ.* Cold Spring Harbor NY: Cold Spring Harbor Laboratory Press., 2007.

[138] Toni Stojanovski and Ljupco Kocarev. Chaos-based random number generators-part i: analysis [cryptography]. *IEEE Transactions on Circuits and Systems I: Fundamental Theory and Applications*, 48(3):281–288, 2001.

[139] Amédée T, Robert A, and Coles JA. Potassium homeostasis and glial energy metabolism. *Glia*, 21(1):46–55, 1997.

[140] Fink C. G. Murphy G. G. Zochowski M. Booth V. A dynamical role for acetylcholine in synaptic renormalization. *PLoS Comput Biol*, 9(3):e1002939, 2013.

[141] Abudukeyoumu N. Hernandez-Flores T. Garcia-Munoz M. Arbuthnott G. W. Cholinergic modulation of striatal microcircuits. *European Journal of Neuroscience*, 49(5):604–622, 2019.

[142] Brett Wingeier, Tom Tcheng, Mandy Miller Koop, Bruce C Hill, Gary Heit, and Helen M Bronte-Stewart. Intra-operative stn dbs attenuates the prominent beta rhythm in the stn in parkinson's disease. *Experimental neurology*, 197(1):244–251, 2006.

[143] Gritton H. J. Howe W. M. Romano M. F. DiFeliceantonio A. G. Kramer M. A. Saligrama V. ... Han X. Unique contributions of parvalbumin and cholinergic interneurons in organizing striatal networks during movement. *Nature neuroscience*, 22(4):586–597, 2019.

[144] Ishii M. Kurachi Y. Muscarinic acetylcholine receptors. *Current pharmaceutical design*, 12(28):3573–3581, 2006.

[145] Surmeier D. J. Song W. J. Yan Z. Coordinated expression of dopamine receptors in neostriatal medium spiny neurons. *Journal of neuroscience*, 16(20):6579–6591, 1996.